1-Dimensional Zinc Oxide Nanomaterial Growth and Solar Cell Applications

by

Hyung Woo Choi

A Dissertation Presented in Partial Fulfillment
of the Requirements for the Degree
Doctor of Philosophy

Approved November 2012 by the
Graduate Supervisory Committee:

Terry L. Alford, Chair
Stephen Krause
N. David Theodore

ARIZONA STATE UNIVERSITY

December 2012

ABSTRACT

Zinc oxide (ZnO) has attracted much interest during last decades as a functional material. Furthermore, ZnO is a potential material for transparent conducting oxide material competing with indium tin oxide (ITO), graphene, and carbon nanotube film. It has been known as a conductive material when doped with elements such as indium, gallium and aluminum. The solubility of those dopant elements in ZnO is still debatable; but, it is necessary to find alternative conducting materials when their form is film or nanostructure for display devices. This is a consequence of the ever increasing price of indium. In addition, a new generation solar cell (nanostructured or hybrid photovoltaics) requires compatible materials which are capable of free standing on substrates without seed or buffer layers and have the ability introduce electrons or holes pathway without blocking towards electrodes. The nanostructures for solar cells using inorganic materials such as silicon (Si), titanium oxide (TiO_2), and ZnO have been an interesting topic for research in solar cell community in order to overcome the limitation of efficiency for organic solar cells.

This dissertation is a study of the rational solution-based synthesis of 1-dimentional ZnO nanomaterial and its solar cell applications. These results have implications in cost effective and uniform nanomanufacturing for the next generation solar cells application by controlling growth condition and by doping transition metal element in solution.

ACKNOWLEDGMENTS

I would like to sincerely thank to my advisor Professor Terry L. Alford for his endless support and guidance to the right way. I would not have been able to do this dissertation without his help. I am indebted to him a lot and I cannot thank him enough.

I would also expand my gratitude to Professor Stephen Krause and Dr. N. David Theodore for their fruitful advice and support.

I am happy to give my thanks to my group members including Rajitha Vemuri, Aritra Dhar, Sayantan Das, and Samuel Tobler for their helps and friendship.

I wish to thank Kyu Sung Lee and JaeYoung Choi for their kind advices and sincere friendship for 4 years. I would not keep my track without their support. I will never forget the days working with them in the Flexible Display Center. I owe Sang Eun a lot of things. She has made me a better person with her constant encouragement.

I really thank my sisters, Hee Jung, Hee Jo for their support. Hee Jung, my big sister, gave me a lot of love and help. I could not thank her more.

Finally, I am deeply grateful to my father, Jeen Kap Choi, for his love, support, and encouragement.

TABLE OF CONTENTS

Page

CHAPTER Page

CHAPTER Page

LIST OF TABLES

LIST OF FIGURES

Figure Page

Figure Page

Figure Page

Figure Page

Chapter 1

INTRODUCTION

1-1. General properties of zinc oxide (ZnO)

Zinc oxide is a wide bandgap semiconductor (3.3 eV) exhibiting natively n-type due to oxygen vacancies and has attracted much interest during last decades as a functional material. ZnO has several favorable properties: good transparency, high electron mobility, wide bandgap, strong room-temperature luminescence, *etc*. Those properties have been already used in applications for transparent conducting electrodes in liquid crystal displays, electronic applications as thin-film transistors, light-emitting diodes and solar cell, *etc*.[1-9]

Its property of a wide bandgap makes ZnO as a promising material for photonic applications as well in the ultraviolet or blue spectrum range, while the high exciton-binding energy (60 meV) allows an efficient exciton emission even at room temperature.[9-10] In addition, ZnO doped with transition metals shows great promise for spintronic applications.[11-13] It has also been suggested that ZnO exhibits high sensitivity to various gas species such as ethanol, acetylene, and carbon monoxide; this makes it suitable for sensor applications.[10] ZnO is also transparent to visible light and can be made highly conductive by doping. Moreover, ZnO is chemically stable and environmentally friendly. Consequently, ZnO is a versatile functional material that has a diverse group of growth morphologies, in the form of powders, single crystals, thin films, and nanostructures [14]; these morphologies include nanoparticles, nanorods (NRs) and nanowires (NWs)

Reduction in physical size introduces novel electrical, mechanical, chemical, and optical properties that are believed to be the result of surface and quantum confinement effects. [15] Large surface to volume ratio, various deep level emissions of intrinsic or extrinsic defects in the visible range contribute to the optical transitions more significantly in addition to the ultraviolet excitonic emission.[1-3]

1-2. ZnO crystal structure

Zinc oxide, like other II-VI semiconductors, is a hexagonal crystal structure which is point group *3m*, space group $P6mc$, lattice parameters a_o = 0.325 nm and c = 0.52 nm their ratio c/a ~1.6 is close to the ideal value for hexagonal cell c/a =1.633 and non-centrosymmetric symmetry and polar surfaces.

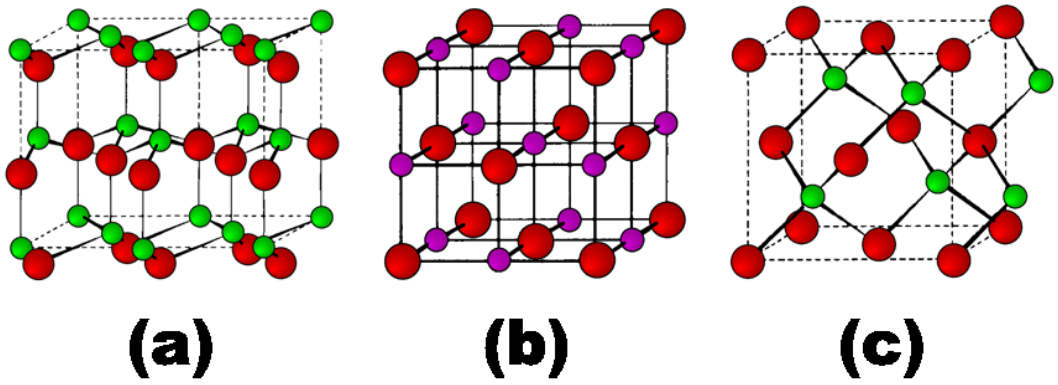

Figure 1-1. ZnO crystal structure (a) Wurtzite, (b) Rock salt, and (c) Zinc blend structures, respectively (green and purple: zinc, red: oxygen).[16]

Although ZnO has meta-stable cubic phases (zinc blend and rock salt), the thermodynamically stable crystal structure is the wurtzite structure at

ambient conditions. The crystal structure is described as alternating planes composed of tetrahedrally coordinated Zn^{2+} and O^{2-} ions stacked along the *c* axis.[16-17]

1-3. Wide bandgap properties of ZnO

Table I shows the various bandgap energies as a function of the lattice constant for the common III-V and II-VI compound semiconductors. ZnO is one of the II-Vi semiconductors including Zns, ZnSe, CdSe, ZnTe, and Cd Te. The bandgap of ZnO is similar to that of GaN. The large exciton binding energy of 60 meV allows ZnO as a potential material for efficient UV laser application and low power thresholds for pumping at room temperature.[9-10] The other advantage of wide bandgap materials in electronics is due to the high temperature and high power devices. High temperature operation requires a wide bandgap; such that, the intrinsic carrier concentration remains. The intrinsic carrier concentrations on the order of 10^{15} cm^{-3} occur at 500 ℃ for gallium arsenide (GaAs, Eg = 1.4 eV) and a 1000 ℃ for wide bandgap semiconductors such as gallium nitride (GaN, Eg = 3.4 eV) and ZnO.[18] High power operation is attractive for the wide bandgap semiconductors owing to the one order of magnitude higher breakdown fields compared to silicon and gallium arsenide. In optics, wide bandgap semiconductors have much interest for the development of blue and ultraviolet light emitting diodes and lasers.

Table I. The properties of common III-V and II-VI compound semiconductors

Group	Compound	Name	Crystal Structure	Bandgap (eV)		Mobility at 300 K (cm/V·s)		Band
				300 K	0 K	Electron	Hole	
III-V	GaAs	Gallium arsenide	Zinc blend	1.42	1.52	8500	400	Direct
	GaN	Gallium nitride	Wurtzite	3.45	3.4	440	380	Direct
	GaP	Gallium phosphide	Zinc blend	2.26	2.26	250	110	Indirect
	GaSb	Gallium antimonide	Zinc blend	0.72	0.82	3000	850	Direct
	InAs	Indium arsenide	Zinc blend	0.36	0.42	40000	460	Direct
	InP	Indium phosphide	Zinc blend	1.35	1.42	5400	150	Direct
	InSb	Indium antimonide	Zinc blend	0.17	0.23	80000	1250	Direct
II-VI	CdSe	Cadmium selenide	Zinc blend	1.7	1.85	800		Direct
	CdTe	Cadmium telluride	Zinc blend	1.44		1050	100	Direct
	ZnO	Zinc oxide	Wurtzite	3.3	3.42	200	180	Direct
	ZnS	Zinc sulfide	Zinc blend	3.54	3.84	165	5	Direct

1-4. ZnO nanomaterials growth

There are multiple of ways to produce the various forms of ZnO depending on process methods. It can be divided by the resulting ZnO form and by process types: bulk, thin film, nanowire, nanodot, nanobelt and vapor deposition or growth from solution and other parameters, respectively. Recently, nanodevices have been demonstrated with ZnO in the form of electric field effect switch,[19] single electron transistors,[20] biological and chemical sensor[21] and luminescence[22] for 1-dimensional semiconducting structures.

One of the reasons for understanding of nucleation and growth mechanism and synthesis method is that it is necessary for the realization of nanoscale device applications. The most popular method for fabrication ZnO nanowires involves *vapor-liquid-solid* (VLS) growth. This was proposed to explain the growth of single crystalline silicon wire by Wagner.[23] The growth of nanowire, nanotube, and nanorods for numerous materials has been understood by VLS model and is illustrated in Figure 1-2.

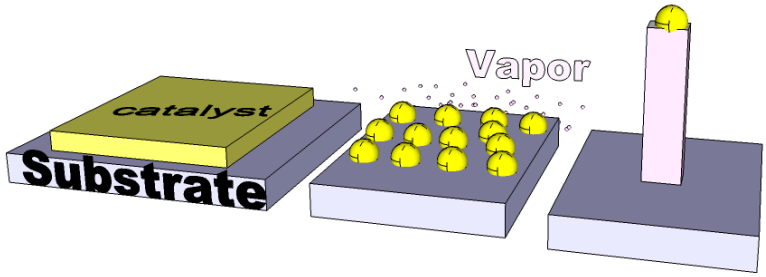

Figure 1-2. Illustration of vapor-liquid-solid model.

The catalyst layer called seed layer is directly deposited on a substrate as a thin film or particles. The vapor is supplied by numerous methods for nanomaterial formation. Increasing the material's temperature results in the formation of a vapor that induces catalyst transformed a liquid phase and results in nanomaterial growth.

In VLS model, the catalyst must be suspended on the top of the nanomaterial. The diameter of nanomaterial is determined by the size of catalyst (more controllable by seed size) resulting in high aspect ratio material growth. [24]

On the other hand, the growth mechanism called *root-growth* is commonly found in nanomaterials growth such as tungsten oxide ($W_{18}O_{49}$), one of the tungsten suboxides,[25] and carbon nanotubes.[26] Each metal catalyst gives energetically favorable sites where the vapor material comes to adhere on them. With catalyst, the nanoparticles are produced before the nanomaterial formation.

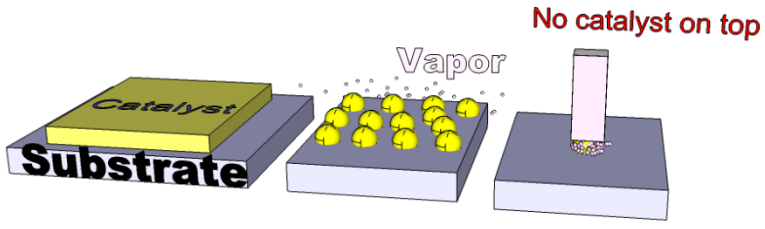

Figure 1-3. Illustration of root growth model.

In this study, however, ZnO nanowire growth was mainly done by electrochemical deposition using CH Instrument 610B potentiostat in a zinc

chloride aqueous solution without catalysts on ITO substrate. The dimension of grown ZnO nanowires were 10~200 nm diameter depending on zinc chloride and potassium chloride concentrations and 100 nm~2 um length depending on growth time and applied voltage controlled by potentiostat.

ZnO nanowires can be grown on any substrate that has a high conductivity including conducting phase, dots, particles, even several atoms. These substrates serve as the working electrode in a three-electrode system. Especially, in the solar cell industry, ITO is a common substrate for growth of nanostructure of ZnO with controllable parameters such as voltage and large number of nucleation sites.

1-5. Electrochemical deposition of ZnO

Electrochemistry is a part of chemistry study that contains chemical reactions which take place in a solution at the surface of electrodes (a metal or a semiconductor). The ionic conductor, the electrolyte, transfers electrons between the electrodes and the electrolyte or species in solution. In contrast, chemical reactions where electrons are transferred between molecules are called oxidation/reduction (redox) reactions.[27] In general, electrochemistry deals with situations where oxidation and reduction reactions are separated in space or time, connected by an external electric circuit. If a chemical reaction is facilitated by external voltage, it is defined as electrolysis. During electrochemical deposition, chemical energy is transformed into electrical energy and is expressed mathematically as the product of the cell's electrochemical cell voltage (also referred to as electromotive force or '*EMF*') and the electric charge transferred through the external circuit.[27]

There are various important electrochemical processes in both nature and industry, like the coating of objects with metals or metal oxides through electrochemical deposition and the detection of alcohol in drunken drivers through the redox reaction of ethanol.[28-31]

The major advantages of the solution-based technique (in aqueous or non-hydrolytic media) for synthesizing nanomaterials are high yield, low cost and easy process. The solution-based technique has been demonstrated as a promising alternative approach for the mass production of metal, semiconductor and oxide nanomaterials with excellent controls of the shape

and composition with high reproducibility. However, the ZnO nanowires synthesized in aqueous solution may often suffer from poor crystallinity.[32]

For the formation of 1-dimensional ZnO nanostructures from solution, several growth mechanisms have been developed, such as self-nucleation,[33] anisotropic growth[34] of crystals by thermodynamic or kinetic control and structural directed growth by templates.[35] The anisotropic growth of ZnO crystals induced by different surface energies can lead to the formation of elongated nanocrystals. However, the differences in the surface energies of most materials are not large enough in order to cause highly anisotropic growth of long nanowires. By adding the surfactant molecules that selectively adsorb and attached onto certain surfaces of the nanocrystals reduces the growth of certain surfaces. This selective reaction induces nanocrystals elongation along a favorable direction to form nanowires as shown in Table II. As a matter of fact, the formation mechanism of ZnO nanowires in solution is complicated and the selection or function of the structural parameter requires further and systematic investigation.

Table II. Summary of different results and methods for aqueous solution growth of ZnO nanorods, naotubes, nanobelt and nanowires [36]

Growth solution	Morphology	Focus of investigation
Zinc nitrate, HMT	Microtubes	On Si and conducting , glass substrates [37]
Zinc nitrate, HMT	Nanotubes	Influence of substrate and seed layer [38]
Zinc nitrate, HMT	Aligned nanowire arrays	Influence of seed layer [39]
Zinc-nitrate, HMT, citriate	Oriented nanocolumns,	Control of aspect ratio: nanoplates , addition of citrate anions decreases aspect ratio [40]
Zinc nitrate, zinc acetate, HMT	Highly aligned nanorods	Influence of substrate and seed layer [41]
Zinc nitrate, triethanolamine, HCl (pH 5)	Ordered nanorods	Influence of substrate and counter ions in growth solution [42]
Zinc nitrate, thiourea	Nanowires, flower-like, tube-like	Influence of reactants, substrate pretreatment [43]
Zinc acetate, sodium hydroxide, citric acid	Disk-like, flowerlike, nanorods	Influence of pH on growth solution [44]
Comparison of different growth solutions	Star-like, nanorods	Influence of reaction conditions: ligand, counter-ions, pH, ionic strength, and deposition time [45]

Chapter 2

HYBRID/NANOSTRUCTURED SOLAR CELLS

2-1. Organic solar cells

Before introducing the research highlights in this chapter, it should be noted here that understanding the concept of photovoltaic is imperative. The photovoltaic effect means that electrons are transferred between different bands (*i.e.,* from the valence to conduction bands) within the materials resulting in the buildup of voltage between two electrodes.[46] Photovoltaic effect is the basic physical process through a photovoltaic cell (also called solar cell) converts sunlight into electricity that was firstly found by Alexandre-Edmond Becquerel (1820-1891) who studied the solar spectrum and optics. Sunlight composed of photons, packets of solar energy, that contain different amounts of energy that correspond to the different wavelengths of the solar spectrum. In the case of photons impinge upon a photovoltaic cell, they can be reflected, absorbed, and transmitted.

Only the absorbed photons generated electricity. The energy of photons is transferred to an electron in an atom of the device. By obtaining the energy from sunlight, the electrons inside of a photovoltaic cell are capable of escaping from their ground state associated with a single atom in the energy band to generate the current in an electric circuit. [46]

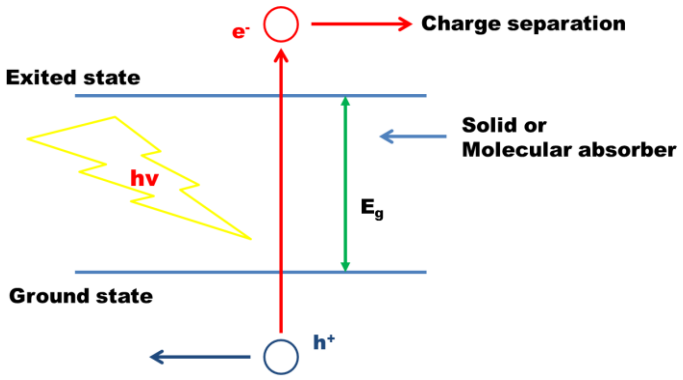

Figure 2-1. Illustration of exciton generation process.

In addition, it has to be mentioned that the photons interact with absorber (also called active layer) and induce excitons. . It is these excitons that are the source of current flow, moving through the bands in absorber. As soon as sunlight strikes the active layer, the energy enough to electron excited is transferred towards charge so that the current flow occurs within bands.

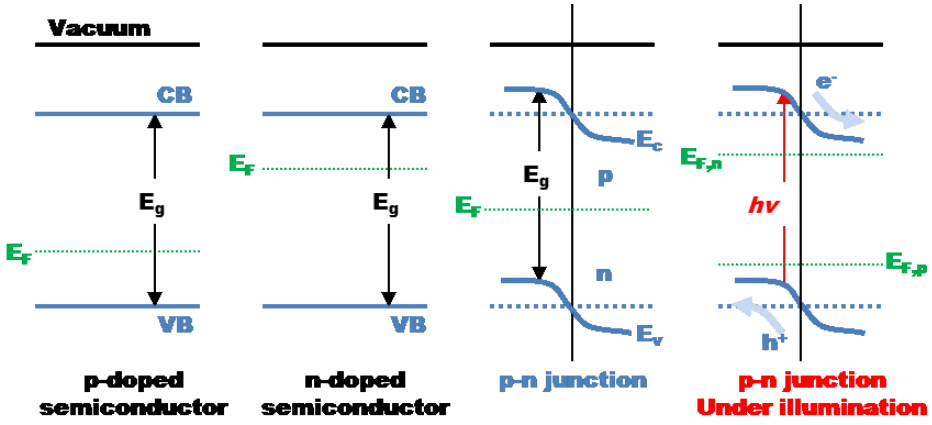

Figure 2-2. Illustration of the band structure of p-n junction solar cell.

Beside inorganic solar cells, which may be considered as organic/inorganic hybrid cells that are other types of organic solar cells become of great interest.[47-55] These cells can be divided into molecular and polymer, bulk heterojunction (BHJ) cells. Organic materials such as conjugated polymer, dyes, molecular organic materials can show p- or n-type semiconducting properties including high optical absorption coefficient that offers the possibility for the production of very thin solar cells. Therefore, only small amounts are necessary for fabrication of devices. Additionally, the interest stems from technological aspects as the expected ease of large scale manufacturing at low temperature and cost. There are still huge challenges with organic solar cells reported in literatures. Organic solar cells offer the hope of being very cheap due to the variety of materials, composition, and concepts, which reflects the possibilities in terms of devices manufacturing, materials consumption, and material design.[56-65]

However, in organic solar cells, the key challenge is that the charge generation layer thickness is much smaller than that of inorganic cells which means the lifetime of charge is much shorter. In order to circumvent the problem, several attempts have been reported in terms of hybrid or nanostructured solar cells. The chemical structures of some molecular materials used for organic solar cells are shown in Figures 2-3 and 2-4. All of these materials are soluble in several solvents depending on polymer types due to their side chain solubilization and their photo and electroluminescence. For fabricating donor-acceptor structure, the donor polymers can be either combined with an acceptor polymer (bulk

heterojunction) or with fullerenes either in planar or diffuse bilayer structure. Recently, there are several different types of polymer species for organic solar cells focusing on chemical structures of acceptor and donor materials such as new fullerene derivatives (C_{60}, C_{61}, C_{71}, *etc*).[49]

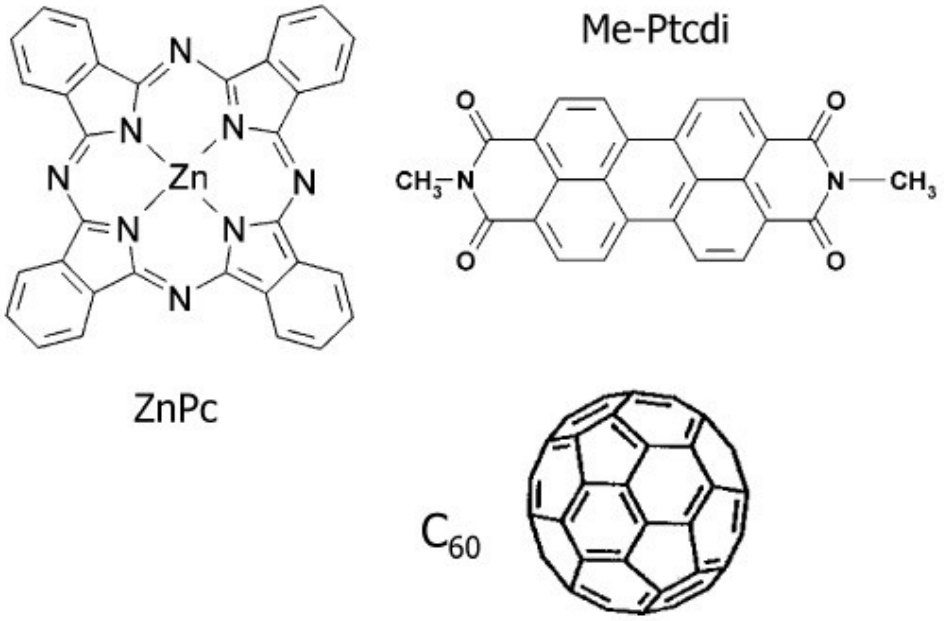

Figure 2-3. Chemical structure of evaporated organic molecules applied in organic solar cells. ZnPc (zinc-phthalocyanine), Me-Ptcdi (N,N-dimethyl perylene-dicarboximide), and fullerene (C_{60}).[49]

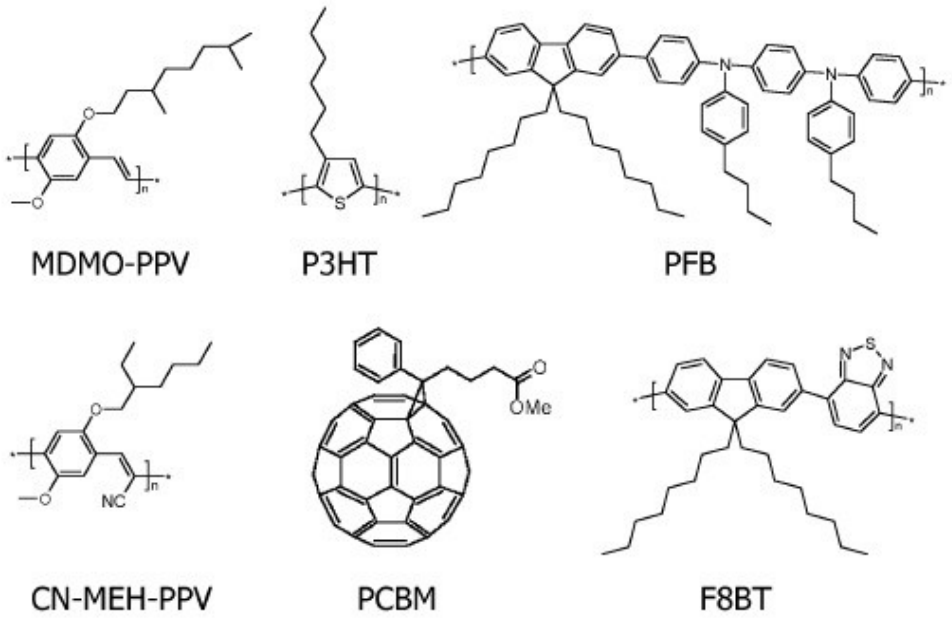

Figure 2-4. Chemical structure of solution processible conjugated polymers and fullerene derivative for organic solar cells. Upper row: the p-type hole conducting donor polymers, MDMO-PPV (poly[2-methoxy-5-(3,7-dimethyloctyloxy)]-1,4-phenylenevinylene), P3HT (poly(3-hexylthiophene), PFB (poly(9,9'-dioctylfluorene-co-bis-N,N'-(4-butylphenyl)-bis-N,N'-phenyl-1,4-phenylenediamine)), Lower row: the electron conducting acceptor polymers, CN-MEH-PPV (Poly[2-methoxy-5-(2-ethylhexyloxy)-1,4-phenylenevinylene]), (6,6)-phenyl C_{61} butyric acid methyl ester (PCBM), and F8BT (poly(9,9-dioctylfluoreneco-benzothiadiazole)).[49]

The design and choice of efficient donor and acceptor molecules is of interest. It is critical for candidate molecules to gain optical bandgaps that are small enough to be excited efficiently by solar radiation. The majority of this radiation is produced in the visible and infrared (IR) regions within

wavelengths over 350 nm corresponding to the energy less than 3.5 eV. Donor molecules must be able to transfer electrons and acceptor molecules must allow holes transport. The combination of donor and acceptor as shown in Figure 2-5 must be chosen to allow for the proper offset between their highest occupied molecular orbital (HOMO) and lowest unoccupied molecular orbital (LUMO) levels that are similar to valence and conduction bands in inorganic solar cells.

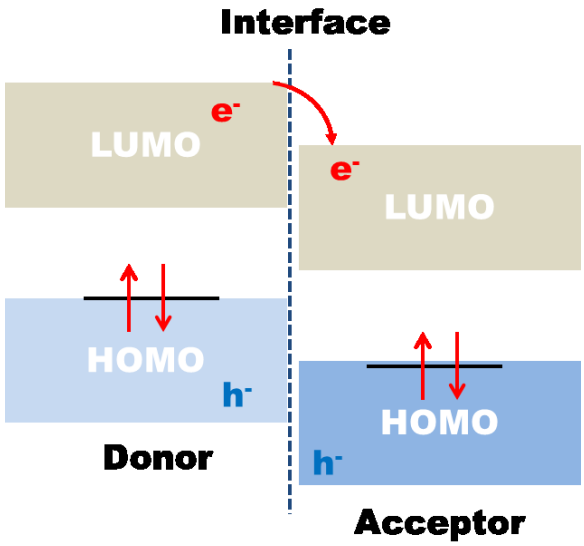

Figure 2-5. Illustration of HOMO-LUMO in organic solar cell.

Organic solar cells generally consist of a donor and acceptor, which are similar in concept to the two types of dope silicon in silicon solar cells. Unlike silicon solar cells, the donor and acceptor in organic solar cells are completely different materials. Each material has a characteristic HOMO and LUMO energy with the HOMO and LUMO of the donor being higher in energy than their respective counterparts in the acceptor. The gap between the HOMO

and LUMO is called as the optical bandgap. Optical bandgap determines the minimum wavelength of incoming light required for excitation in each materials. Photons hitting either donor or acceptor molecules excite an electron from the HOMO to the LUMO. In order to generate the free electron-hole pair, the exciton must travel to the interface between the donor and acceptor molecules or to electrode. At this interface, electrons which have been excited to the LUMO of the molecule can be transferred into the LUMO of the acceptor and holes in the HOMO can jump into the HOMO of the donor. This dissociation is possible only if the difference in energy between the HOMO and LUMO is greater than the binding energy of the exciton. This process is called *charge separation*. The great challenge of organic solar cell earlier in this chapter is a short life time of charges. If exciton is not able to reach electrodes, recombination occurs so that the additional energy to generate another exciton is required for current flow.[49]

The best research organic solar cell efficiencies have been reached 10% in 2012 as shown in Figure 2-6 summarized by national renewable energy laboratory (NREL). Efficiencies increased rapidly with molecular layers system based on conjugated polymer with fullerene derivatives. The efficiency and stability against environmental influences have to be increased further to make organic solar cells become commercialized.[50]

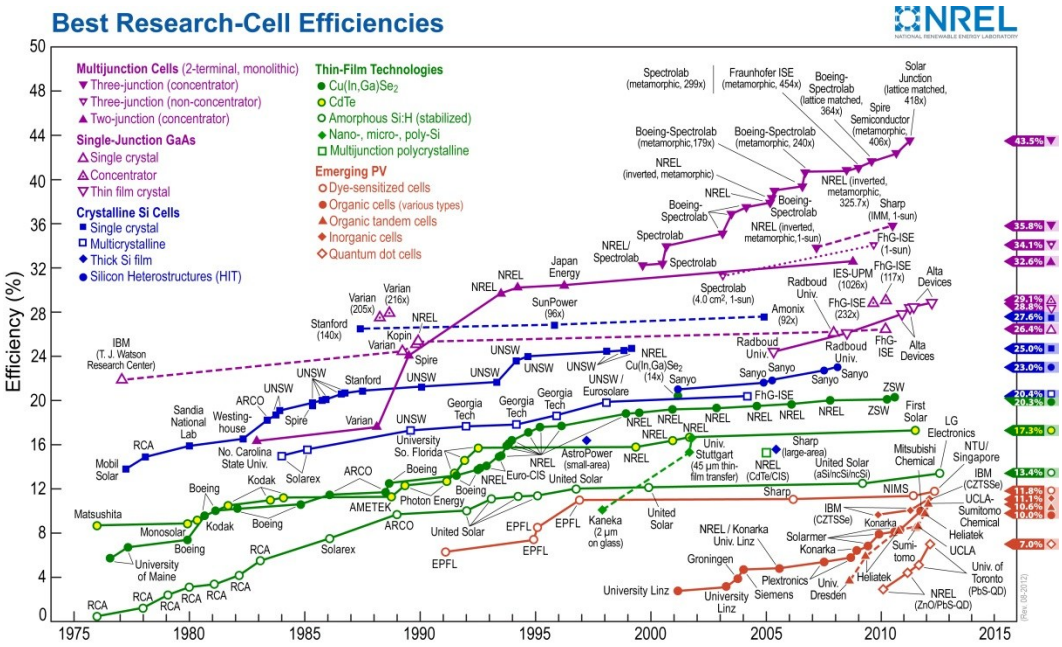

Figure 2-6. The best research-cell efficiencies. (courtesy of National Renewable Energy Laboratory)

Technology development of first generation photovoltaics based on crystalline Si is manufactured as devices with efficiencies 20~25%. To minimize the high material costs associated with high purity Si, second generation thin film solar cells based on CdTe, and $CuInSe_2$ are beginning to reach the market place and show moderate efficiencies in the range of 16-20%. Third generation devices based on multi-junction concentrators have reached efficiencies above 40%. Organic photovoltaics still remains at 10% of highest efficiency, but processing costs limit their applications to real life.[50]

The goal of second and third generation photovoltaic devices seek to maximize conversion efficiencies while minimizing processing costs to achieve the $1/watt goal which represents the economic benchmark when

photovoltaic is cost competitive to fossil fuel energy sources. To achieve this, the Shockley-Queisser limit for single p-n junction solar cell must be overcome and nanomaterials such as nanowires and nanoparticles will play a critical role. The fourth generation solar cell, called hybrid or nanostructured, is firstly adapted this idea instead of making solar cell multi-junction.[66]

2-2. Characterization of organic solar cells

The current-voltage characteristics of a solar cell in the dark and under illumination are shown in Figure 2-7. In the dark, there is almost no current flowing, until the contacts start to inject at forward bias for voltages larger than the open circuit voltage.

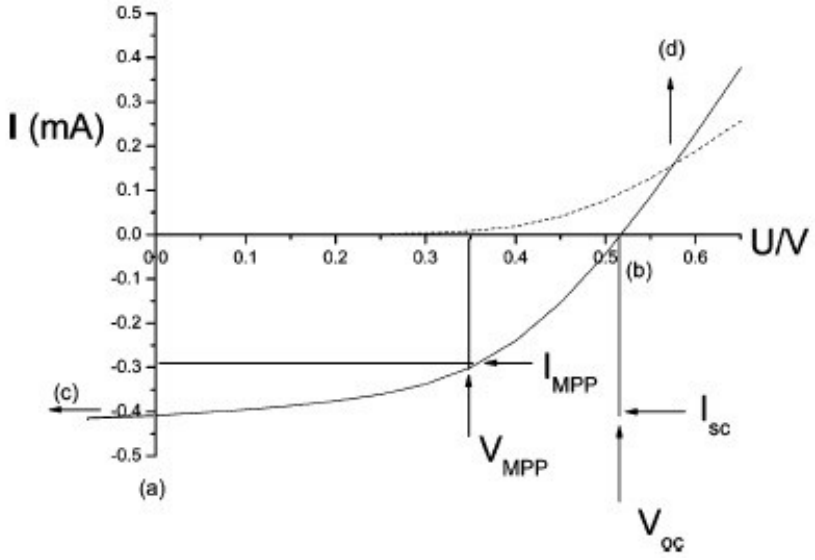

Figure 2-7. Current-Voltage (I-V) curves of an organic solar cell (dark ----; illuminated –). [67]

In the fourth quadrant (between (a) and (b)), the device generates power under light. At maximum power point (MPP), the product of current

and voltage is the largest. The photovoltaic power conversion efficiency of a solar cell is determined by the following formula.

$$\eta_{e=\frac{V_{oc}\,I_{sc}\,FF}{P_{in}}}$$

$$FF = \frac{I_{mpp}\,V_{mpp}}{I_{SC}\,V_{OC}}$$

where V_{oc} is the open circuit voltage, I_{sc} is the short circuit current, FF is the fill factor, and P_{in} is the incident light power. Generally, the V_{oc} (open circuit voltage) of a metal-insulator-metal device is determined by the difference in work functions of the two metal contacts.[68] However, in a p-n junction, the maximum available voltage is determined by the difference of the quasi-Fermi levels of the two charge carriers, that is, n-doped semiconductor energy level and p-doped semiconductor energy level, respectively. In organic solar cells, the open circuit voltage is found to be linearly dependent on the highest occupied molecular orbital (HOMO) level of the donor (n-type semiconductor quasi Fermi level) and lowest unoccupied molecular orbital (LUMO) level of the acceptor (p-type semiconductor quasi Fermi level).[69-70] Interfacial effects at the metal/organic semiconductor interface such as oxide formation change the work function of the electrodes and influence the open circuit voltage.[71-72] In conclusion, the open circuit potential is a sensitive function of energy levels of the used materials as well as their interfaces.[49]

In the ideal, loss free contacts, the short circuit current, I_{sc}, is determined by the product of the photoinduced charge carrier density and the charge carrier mobility within the organic semiconductors:

$$I_{SC} = ne\mu E$$

where n is the density of charge carriers, e is the elementary charge, μ is the mobility, and E is the electric field. Assuming the 100% efficiency for the photoinduced charge generation in a bulk heterojunction mixture, n is the number of absorbed photons per unit volume. Mobility is dependent on the device materials and fabrication parameters. It is sensitive to the nanoscale morphology of the organic semiconductor thin film.[73]

The external quantum efficiency (EQE) or incident photon to current efficiency (IPCE) is simply the number of electrons collected under short circuit conditions, divided by the number of incident photons. EQE is calculated using the following formula:

$$EQE(IPCE) = \frac{Number\ of\ Collected\ Electrons}{Number\ of\ Incident\ Photons} = \left(\frac{hc}{e}\right)\left(\frac{I_{SC}}{\lambda \cdot P_{in}}\right) = \frac{1240 \cdot I_{SC}}{\lambda \cdot P_{in}}$$

where λ [nm] is the incident photon wavelength, I_{sc} [μA/cm^2] is the photocurrent of the device, and P_{in} [W/m^2] is the incident power. The photon generation process consists of the exciton generation and dissociation, charge transfer and charge collection from incident light. EQE can be rewrite as the sum of each process which can be express as

$$EQE = \eta_O \times \eta_A \times \eta_{ED} \times \eta_{CT} \times \eta_{CC} = \eta_O \times IQE$$

where,

$$IQE(\lambda) = \frac{EQE\ (\lambda)}{1 - R(\lambda)}$$

R(λ) is reflectivity.

The fill factor is determined by charge carriers reaching the electrodes, when the built-in field is lowered toward the open circuit voltage.

In fact, there is a competition between charge carrier recombination and transport. Hence, the product of the lifetime τ times the mobility μ determines the distance d that charge carriers can drift under a certain electric field E.

$$d = \mu\tau E$$

This product $\mu\tau$ has to be maximized.[74] Furthermore, the series resistances influence the filling factor (FF) considerably and should be minimized. Finite conductivity of the ITO substrate clearly limits the filling factor on large area solar cells. Finally, the device should be free of current pathways between electrodes to maximize the parallel shunt resistance.[67]

2-3. ZnO nanostructured solar cells

Nanostructured photovoltaic devices made of a conjugated polymer and a metal oxide semiconductor have attracted attention. Olson *et al.* reports hybrid photovoltaic devices using poly (3-hexylthiophene) (P3HT)/ (6,6)-phenyl C_{60} butyric acid methyl ester (PCBM) into solution-synthesized

ZnO nanofibers.[75] Since ZnO has a wide bandgap, it cannot absorb in the visible region of the solar spectrum. Therefore, hybrid ZnO solar cell devices employing organic dye molecules, inorganic quantum dots and nanoparticles which effectively absorb in the visible and IR regions are of interest for efficient energy harvesting. The charge injection efficiency of hybrid P3HT/PCBM/ZnO solar cells processed with and without N719 dye are compared and it is found that both the short circuit current density and the efficiency are higher with the dye.[76] In the CdSe quantum dot sensitized ZnO nanowire solar cell reported by Leschkies *et al.,* the photocurrent generated from the visible light was due to the electron-hole pairs created in the CdSe quantum dots, followed by electron injection into the ZnO nanowires.[77] Chen *et al.* reported an Au nanoparticle-sensitized ZnO nanorod solar cell where the Au nanoparticles enhance the absorption of visible light through surface plasmon resonance and the Schottky barrier at the ZnO/Au interface reduce electron-hole recombination, which ultimately improves efficiency.[78] Others have fabricated core-shell heterostructures to optimize surface chemistry. For example, Plank *et al.* fabricated ZnO-MgO core-shell based solid-state dye sensitized solar cells (DSSCs) and observed a five-fold efficiency improvement compared to pristine ZnO nanowire based photovoltaic devices [79]. Greene *et al.* found that the efficiency of P3HT/ZnO nanorod solar cells could be improved five-fold by a thin TiO_2 shell on the ZnO nanorod arrays. [80] Enhancing light coupling into the active region of the photovoltaic devices is another way to improve efficiency by adding anti-reflective coatings to minimize reflectance losses. ZnO is regarded as a good

dielectric anti-reflective coating material due to its high transparency. Solution-synthesized ZnO nanorod arrays have been employed as efficient solar cell antireflective coatings to enhance solar cell performance.[81]

Flexible solar cells based on nanostructured metal oxides have attracted increasing interest due to the potentially light weight, thin, and bendable advantages. A dye sensitized solar cell based on hydrothermally grown ZnO nanowire films on flexible substrates was reported.[82] ZnO nanoparticles were attached to ZnO nanowire surfaces to further increase the surface area and the results showed promising device stability.

In order to use these ZnO nanostructures for solar cell application, patterning or defining of structure area is critical for efficient light absorption into solar cells. The nanostructures for solar cell using lots of inorganic materials such as TiO_2, Si, and ZnO have been interesting topic for research in solar cell industry that overcome limitation of efficiency for organic solar cells.

2-4. Theoretical efficiency limits of solar cells

In the famous work by Shockley and Queisser, they theorized that the semiconductor bandgap dictates the p-n junction solar cell efficiency.[66] They predicted that the maximum power conversion efficiency of 30% at 1 sun corresponding to a 1.1 eV bandgap. In terms of energy loss, incoming photons whose energy is above the bandgap are lost to heating and those whose energy are below the bandgap pass through and are not absorbed. In the work, they assumed the following: the sun is a blackbody at 6000 K, the

solar cell is a blackbody at 300 K and uniform in temperature, the active region is thick enough to absorb all light above the bandgap, one photon gives rise to one electron-hole pair, all recombination is via radiative processes, all photo-excited carrier pairs which do not recombine radiatively are extracted, and all excited carriers relax to the band edge prior to extraction, relaxation is by creating phonons. The Shockley-Queisser approach is useful for theorizing first generation (bulk crystalline) and second generation (thin film) photovoltaics. One of the goals of third generation photovoltaics is to overcome the Shockley-Queisser limits imposed on single bandgap absorbers.[66]

2-5. Testing standards of solar cells

To simulate solar radiation and characterize the performance of photovoltaic devices in a controlled laboratory environment, there are a number of important considerations.

The first consideration is the emissive light power distribution. The sun is a blackbody radiating at a temperature of 6000 K and the emissive power radiation as a function of wavelength is characterized by Plank's radiation formula. This is the light power distribution experience by objects in outside the earth's atmosphere referred to as air mass (AM) 0 distribution. However, to account for the light scattering and absorption losses associated with earth's atmosphere, the AM 1.5 is established to account for the path length that light travels in earth's atmosphere and is defined as:

$$AM = \frac{1}{cos\theta}$$

θ is the angle between a light ray at noon and the zenith angle of the sun at a given time. Under AM 1.5 standard conditions, θ is 48.2°. The air mass concept accounts for the selective absorption at particular wavelengths of light due to various atmospheric species (O_2, O_3, H_2O, CO_2).[42]

In the world, four laboratories have been certified in accordance with the international electrotechnical commission (IEC) which has standards for all electrical, electronic, and related technologies. Commonly, national renewable energy laboratory (NREL) has been chosen for measuring device performance under standard condition obtained from American society for testing and materials (ASTM) of AM 1.5 global solar irradiation. This condition as shown in Figure 2-8 indicates that direct normal and hemispherical on 37 degree slope of the sun-facing tilted surface was chosen to represent the average latitude of the 48 contiguous United States.

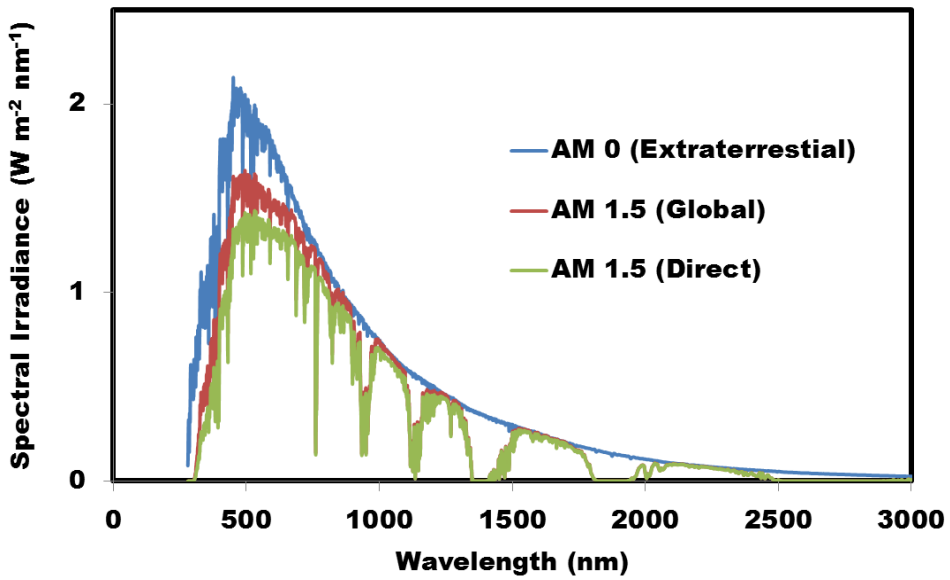

Figure 2-8. Standard reference for solar spectral irradiances generated by American society for testing and materials (ASTM) used in NREL standard condition. [courtesy of American society for testing and materials]

As shown in Figure 2-9, the materials for solar cell research have independent solar spectrum where the photon generation can be maximized. The intensity of light coming from sun has maximum value in the range of visible wavelength. The exciton generation for organic solar cells is focused only on this wavelength range from 350 nm to 800 nm.

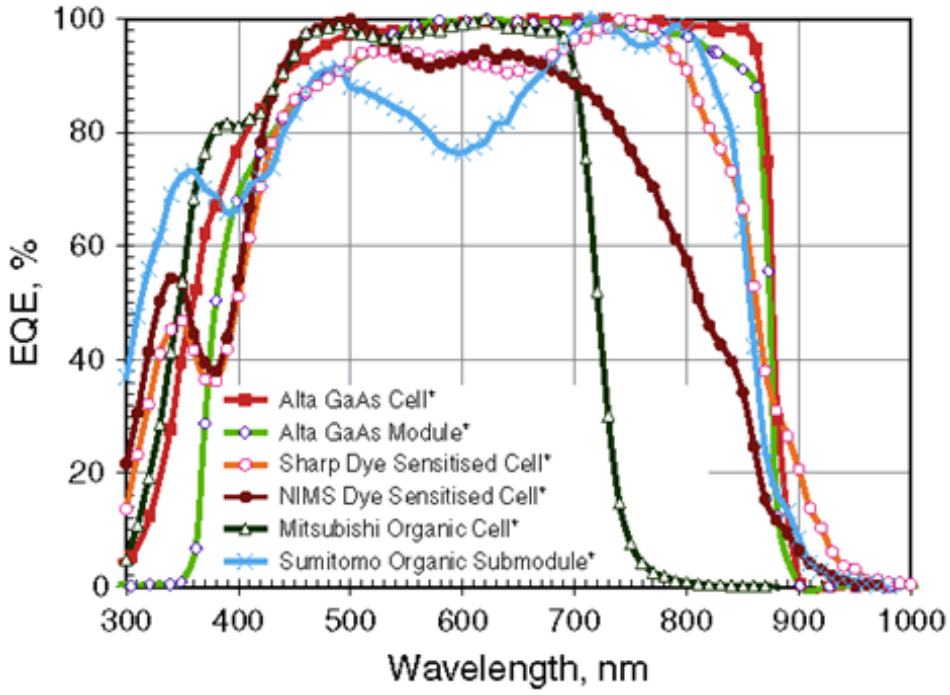

Figure 2-9. External quantum efficiencies (EQEs) for various materials for solar cell researches. [50]

2-6. The concept of ZnO nanostructured organic solar cells

Enhancing light coupling into the active region of the photovoltaic devices is another way to improve efficiency by adding anti-reflective coatings to minimize reflectance losses. ZnO has been considered as a good anti-reflective coating material due to its high transparency and appropriate refractive index (n=2, smooth film) and solution-synthesized ZnO nanorod arrays have been employed as efficient solar cell anti-reflective coatings to enhance solar cell performance.[49] Flexible solar cells based on nanostructured metal oxides have attracted increasing interest due to the potentially light weight, thin, and bendable advantages. A dye-sensitized

solar cell based on hydrothermally grown ZnO nanowire films on flexible substrates was reported.[82] ZnO nanoparticles were added to ZnO nanowire surfaces to further increase the surface area and the results showed promising device stability.

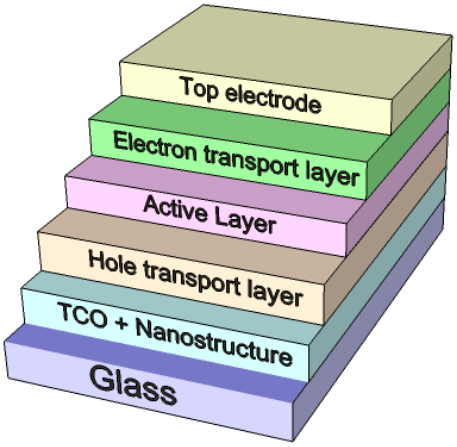

Figure 2-10. Illustration of ZnO nanostructured Organic Photovoltaic device.

Figure 2-10 displays schematic diagram of nanostructured organic photovoltaics. In this study, different from other studies, ZnO nanowires play a critical role of antireflective layer when light comes through the ITO coated glass that causes life time of light inside of active layer longer so that more exciton pairs generate which results in external quantum efficiency increases. There are two possibilities for ZnO nanostructured organic photovoltaics in the consideration of bandgap matching among layers. Figure 2-11 shows illustration of bandgap diagram of the organic photovoltaics with ZnO nanostructure between ITO and poly (3,4-ethylenedioxythiophene) poly (styrene sulfonate) (PEDOT:PSS) layers.

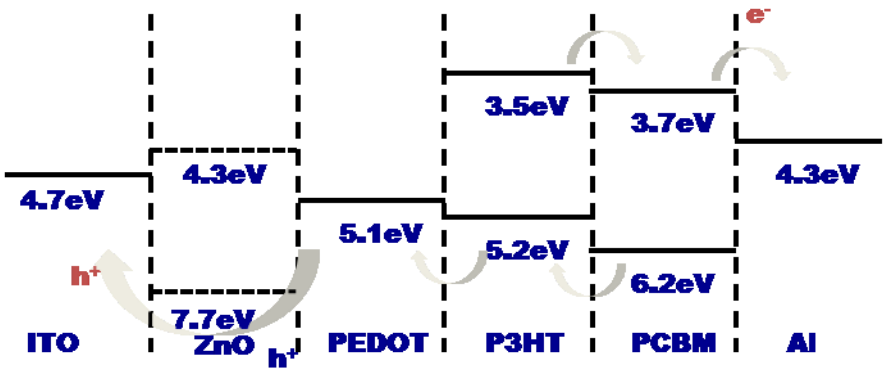

(a) Band diagram of nanostructured organic photovoltaics

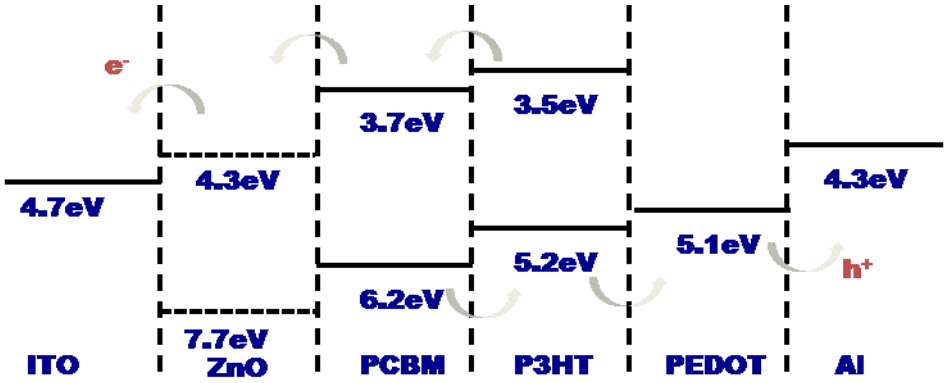

(b) Band diagram of inverted-nanostructured organic photovoltaics

Figure 2-11. Comparison of band diagrams between nanostructured organic photovoltaics and inverted-nanostructured organic photovoltaics.

However, inverted OPV, when ZnO layer forms film on ITO layer, has different charge transport mechanism; ITO receives electrons and Al electrode works as holes transport layer. Due to the difficulty of achieving PEDOT:PSS layer on active layer (P3HT/PCBM), an inverted OPV will be discussed later.

ZnO nanostructure acts as an antireflective structure that enhances light trapping inside of the active layer. Life time of reflected light from top electrode, Al or Ag, will last longer in the active layer that regenerates additional exciton pairs resulting in higher external quantum efficiency that increase power conversion efficiency. However, ZnO on ITO layer also has direct reflection of incident light at the boundary of ITO and nanostructure. The density of ZnO nanowires should be optimized for maximizing exciton generation with respect to diameter, length and density.

Chapter 3

THE NUCLEATION AND GROWTH OF ZINC OXIDE NANOMATERIALS

3-1. Heterogeneous nucleation and growth process

Nucleation and growth are transformations between crystallographic and non-crystallographic states of oxide materials. This transformation is a principle approach for single-crystal growth. To understand the mechanism of solidification is a key factor that controls the mechanical, electronic, magnetic properties of final forms of solids.[83] The nucleation in liquids is always a heterogeneous process. The growth of ZnO from aqueous solution in this study is also a heterogeneous process.

Commonly, the concept of heterogeneous nucleation can be seen in thermodynamics. The consideration of a solid embryo forming in contact with a flat surface, such as an ITO substrate in this study, can be found that for a given volume of solid, the total interfacial energy of the system is minimized if the embryo has the shape of a spherical shape with a certain wetting angle θ.[84]

$$\gamma_{ML}=\gamma_{SM} + \gamma_{SL} \cos\theta$$

or

$$\cos \theta = (\gamma_{ML} - \gamma_{SM}) / \gamma_{SL}$$

The equations above only can be used for the optimum embryo shape on the condition that the surface is flat. The formation of such an embryo will be associated with an excess free energy given by

$$\Delta G_{het} = -V_s\Delta G_v + A_{SL}\gamma_{SL} + A_{SM}\gamma_{SM} - A_{SM}\gamma_{ML}$$

V_s : the volume of the spherical embryo

A_{SL}: The area of the solid/liquid interface

A_{SM}: The area of the solid/surface interface

γ_{SL}: the free energy of the solid/liquid interface

γ_{SM}: the free energy of the solid/surface interface

γ_{ML}: the free energy of the surface/liquid interface

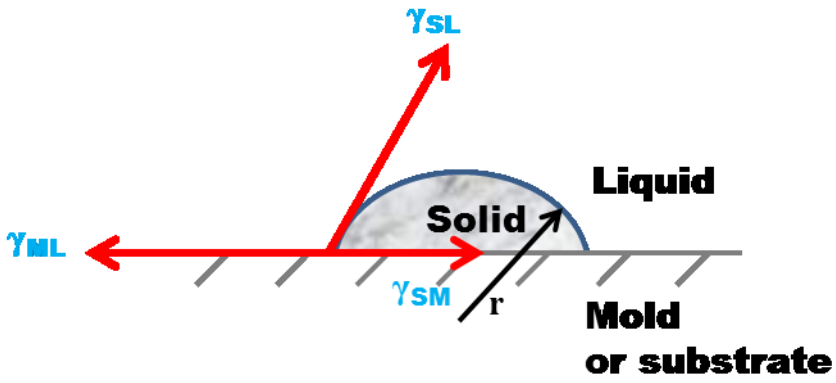

Figure 3-1. Heterogeneous nucleation of spherical cap on a flat substrate.

There are three interfacial energy contributions. The reason why negative sign in front of $V_s\Delta G_v$ is that the formation of embryo allows the reduction of total free energy depending on the volume of embryos. On the surface of a flat substrate, heterogeneous nucleation can be rewritten in terms of the wetting angle (θ) and embryo radius (r) as

$$\Delta G_{het} = \left\{-\frac{4}{3}\pi r^3 \Delta G_v + 4\pi r^2 \gamma_{SL}\right\} S(\theta)$$

where

$$S(\theta) = (2 + cos\theta)(1 - cos\theta)^2/4$$

S(θ) has a numerical value less than 1 dependent only on θ, the shape of the nucleus. Usually, S(θ) is called as a shape factor.

The surface nucleation shown above is a single atom solidifying on a flat surface that is unstable and tend to rejoin to the solution. However, if a sufficient amount of atoms generates a nucleus, it is possible to become self-stabilized and continue to grow.

However, the thermodynamic model of heterogeneous nucleation and growth is commonly used for the case that involves temperature change (ΔT). For the electrochemical deposition, the temperature is constant so that the heterogeneous model is responsible only for nucleation process at the beginning of embryo formation.

3-2. Electrochemical deposition of 1-dimensional ZnO nanomaterials

It is important to note that the driving force of nucleation is for electrochemical deposition is applied potential by potentiostat which enables to give constant voltage between electrodes.

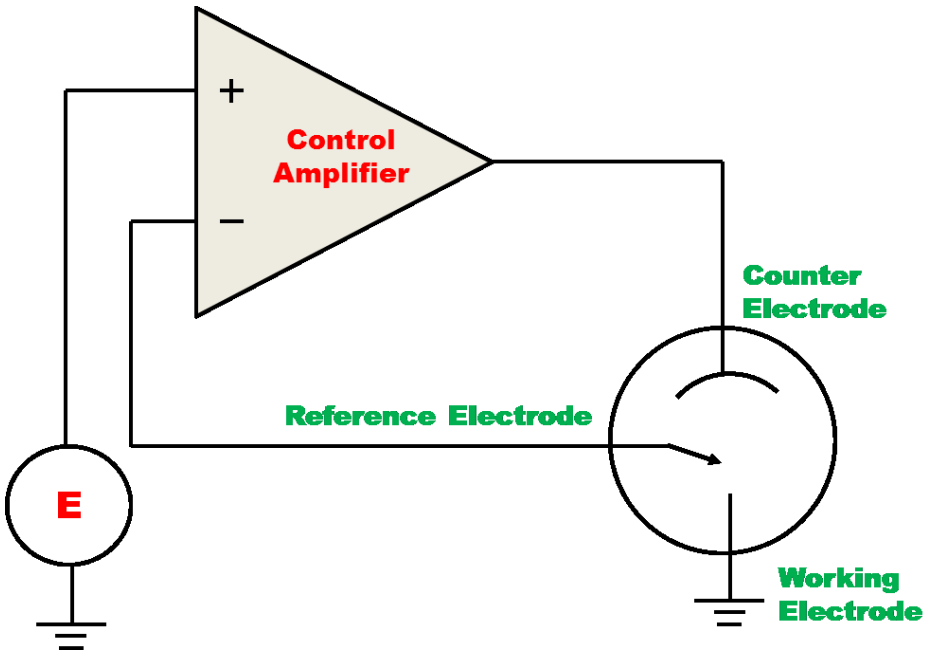

Figure 3-2. Schematic diagram of potentiostat.

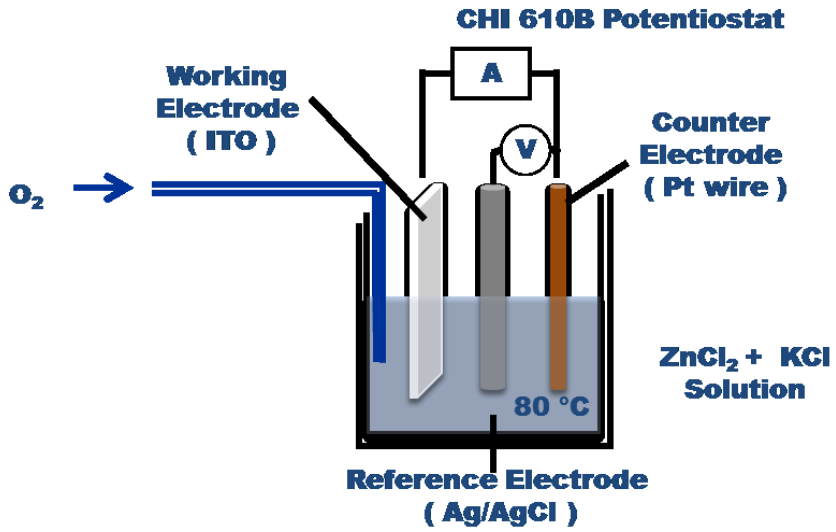

Figure 3-3. Schematic diagram of three electrode electrochemical cell.

The electrochemical deposition can be explained by understanding the mechanism of potentiostat or galvanostat (able to generate a constant current between electrodes) or coulostat (able to maintain a constant charge). In this

study, only potentiostat will be discussed. In addtion, electrochemical deposition can be described as the flow of current among electrodes and conducting material including ionically conducting phase called an electrolyte solution. Unlike electrochemical deposition without external current flow, a current flow by potentiostat or galvanostat results in significant changes of grown crystals.

There are three electrodes connected to the potentiostat for fabricating ZnO nanomaterials. They are working, counter, and reference electrodes. The materials for reference, working, and counter electrodes used in this study are silver/silver chloride (Ag/AgCl), ITO coated glass (or conducting substrates such an ITO coated plastic substrates), and platinum (Pt), respectively. These electrodes are critical for formation of nanomaterials in aqueous solution at a constant electric field, especially depending of the reference electrode due to its own potential in the ironically conducting phase.[27]

By applying electric field between electrodes, charged particles (ions) are accelerated towards one of the two electrodes and establish a field with the direction depending on the sign of the charged particle. Only resistance for the charged particles can be caused by the viscosity of the medium where the particles are moving. The established velocity (v) of the particles called the drift velocity with radius (r) is

$$v = \frac{(z \cdot e_0 \cdot E)}{(6 \cdot \pi \cdot \eta \cdot r)}$$

where

z: atomic number of charge

e_0: elementary charge

E: external potential

η: viscosity

r: ionic radius

The velocity of an ion 'j' can be written as

$$v = \mu_j \cdot E$$

where

μ_j: ionic mobility

There are several parameters that change mobility of an ion in the viscous medium such as a filter, a type of conducting medium, and shape of container. However, in this study, the conducting medium (phase) is a water-based solution which viscosity is 1 with zinc (Zn^+) and potassium (K^+) and chlorine (Cl^-) ions.

An electrical voltage is applied to these electrodes and the ions start movement. Even though some of the colored ions can be recognized at the one of electrodes, the resulting crystal at a working electrode is white colored ZnO nanomaterials with various lengths (50 nm ~ 2μm) depending on growth time.

The reaction occurred at the each electrodes can be described as

Reference (Ag/AgCl) electrode: $Ag + Cl^- \leftrightarrow AgCl + e^-$

Counter (Pt) electrode: $\frac{1}{2}O_2 + H_2O + 2e^- \rightarrow 2\,OH^-$

Working (ITO coated glass) electrode: $Zn^{2+} + 2\,(OH^{-}) \rightarrow ZnO + H_2O$

At the counter electrode, additional oxygen is achieved by bubbling O_2 gas directly into the aqueous solution prior to reaction continues to end of the reaction. On the application of an electric field, reduction of oxygen occurs, leading to the production of OH^- ions on the surface of the working electrode as well as in the solution.

After nucleation, there are three different growth modes shown in Figure 3-4.

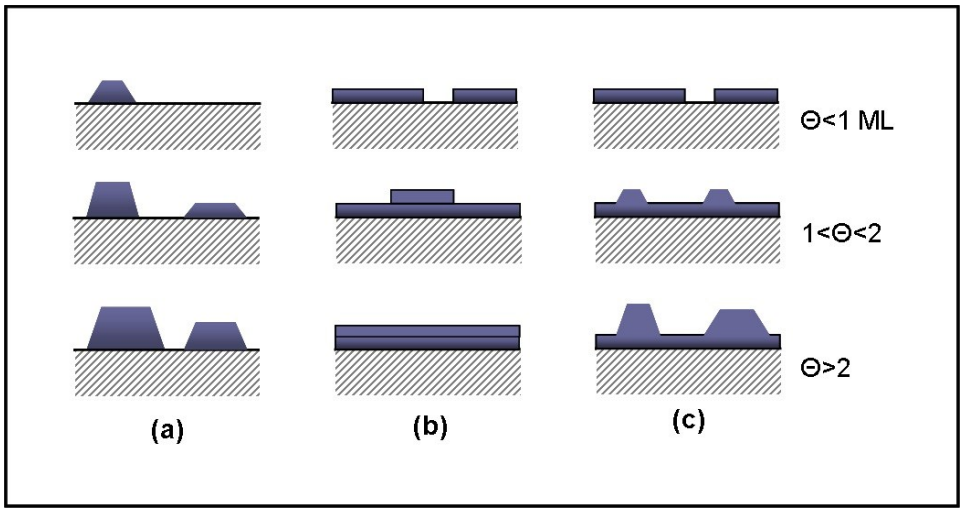

Figure 3-4. Schematic representation of the three growth modes, as a function of the coverage θ in monolayer: (a) island, or Volmer-Weber growth, (b) layer-plus-island, or Stranski-Krastanov growth, and (c) layer-by-layer, or Frank-van der Merwe growth. [85]

The island or Volmer-Weber growth mechanism can be adapted for ZnO nanomaterials growth. The deposited atoms are more strongly bound to

each other than they are to the substrate, the island mode results. On the other hands, there are other terms for ZnO nanomaterials growth which is root-growth firstly used by J. Pfeifer.[25] As shown in Figure 3-5, the nucleus of ZnO is not a sphere but a multi-faced nucleus owing to the native characteristic of ZnO nanocrystal.

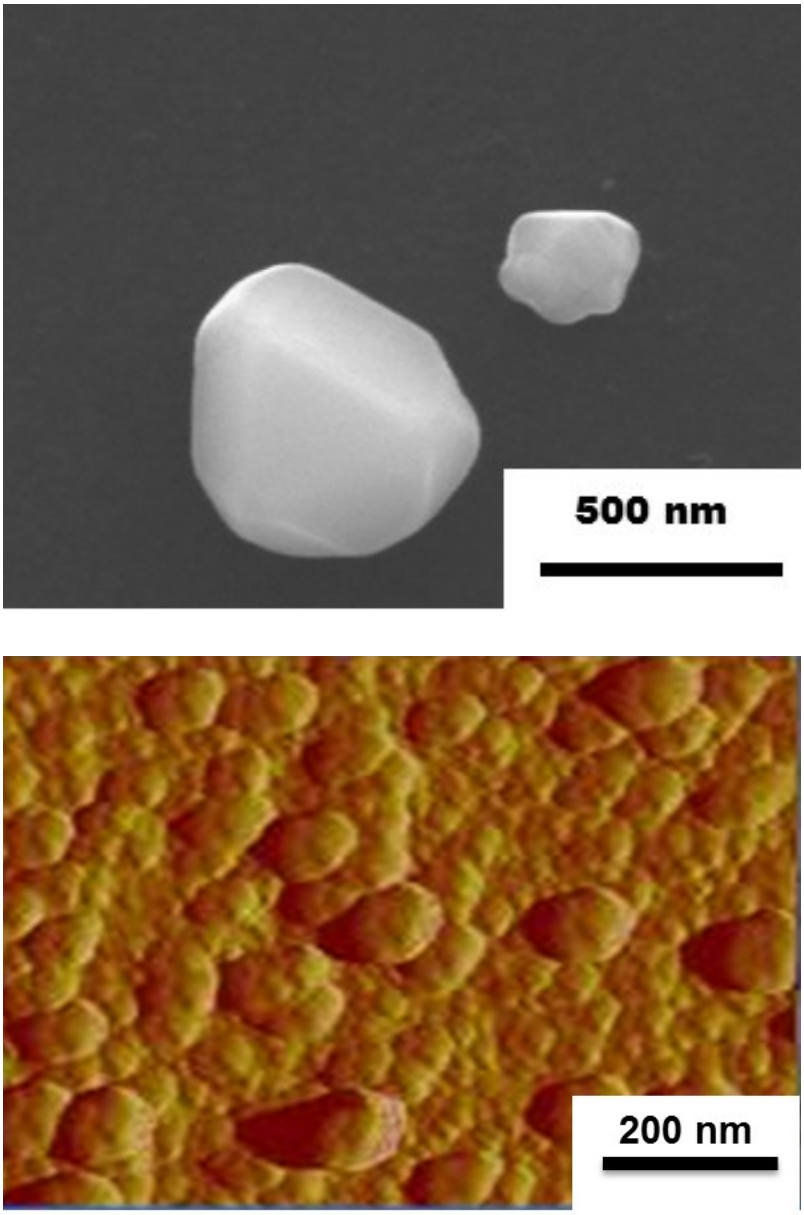

Figure 3-5. FESEM and AFM images of nucleation of ZnO on ITO substrate.

Depending on the substrate, the formation of ZnO nanomaterials shows various size, shape, and facet direction but it is obvious that all nuclei have hexagonal shape.

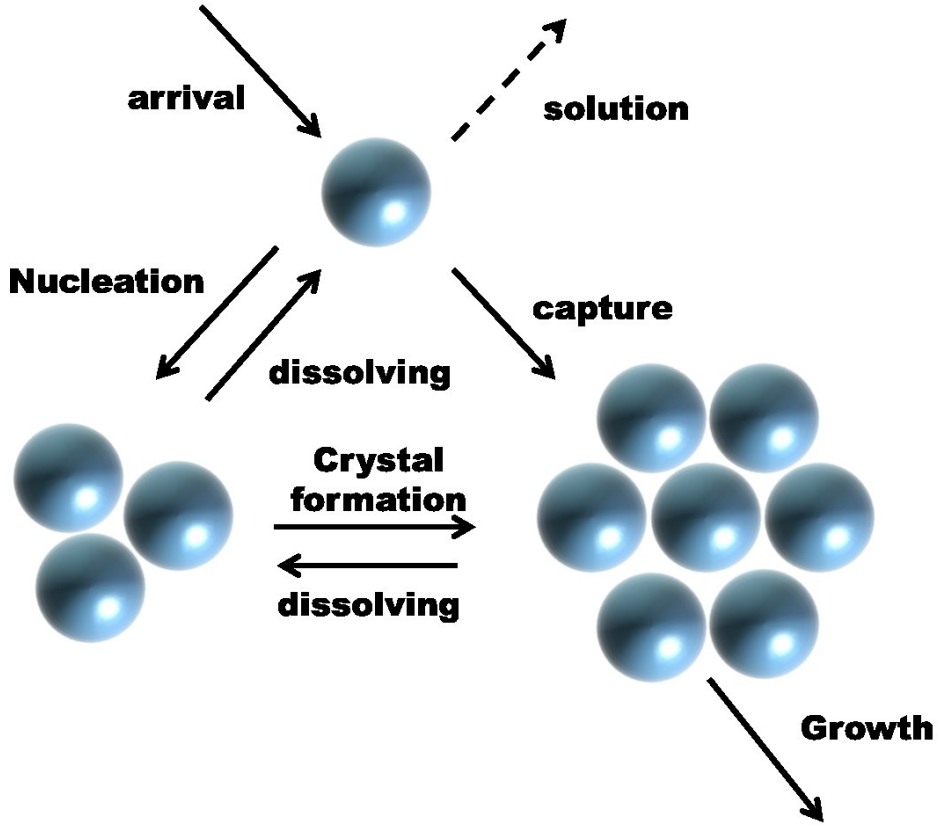

Figure 3-6. Schematic illustration of the interaction between nucleation and growth stages.

Continuous addition of ions from the solution determines the critical radius of nuclei. Once the size of hexagonal shape ZnO is confirmed, ions react with hydroxide forming ZnO nanorods until the reaction ends. The growth of ZnO nanomaterials is an interface-controlled process because the solution has full of ions which can be added to formed crystals. In the solution the ions move freely within a container but the applied voltage give an opportunity for ions attracted towards each electrodes. For example, the Zn^{2+} ions are attracted to the working electrode which has negative bias and

chloride ions are attracted to counter electrode remaining the form of ions without further reaction. The growth rate is determined by interfacial diffusion rate between the solution and crystal.

3-3. Growth conditions for ZnO nanorod array

In order to find proper conditions such as concentration of $ZnCl_2$ and KCl, temperature, pH of solution, applying voltage between working, reference, and counter electrodes, current-voltage measurements have been conducted with a CHI610B potentiostat in the range from -1.5 V to 0 V at 70 ℃ and 80℃. It can be found that there are 2 distinctive smooth peaks for 1 cycle of C-V measurement shown in Figure 3-7.

Current flow between a working electrode and a counter electrode generates hydroxide (OH^-) around -0.7 V. Zn^+ ions react with hydroxide to form ZnO as a resulting crystal. To get consistent condition for ZnO nanorods growth, ZnO growth has been performed less than -0.8 V. There is not enough time for Zn^+ ions to form a wire-shape hexagonal crystal below -1.5 V, large ZnO dots are found after 1 hour growth which is not favorable for high aspect ratio materials. The growth of ZnO nanorod arrays in this study has been performed in the range of -0.8 V ~ -1 V to make that highly oriented ZnO nanorods.

Table III. Potential applied for ZnO nanorod growth

Potential	ZnO growth
Above -0.8 V	None
From -0.8 V to -1.5 V	ZnO nanorods growth
Below -1.5 V	ZnO nanodot growth

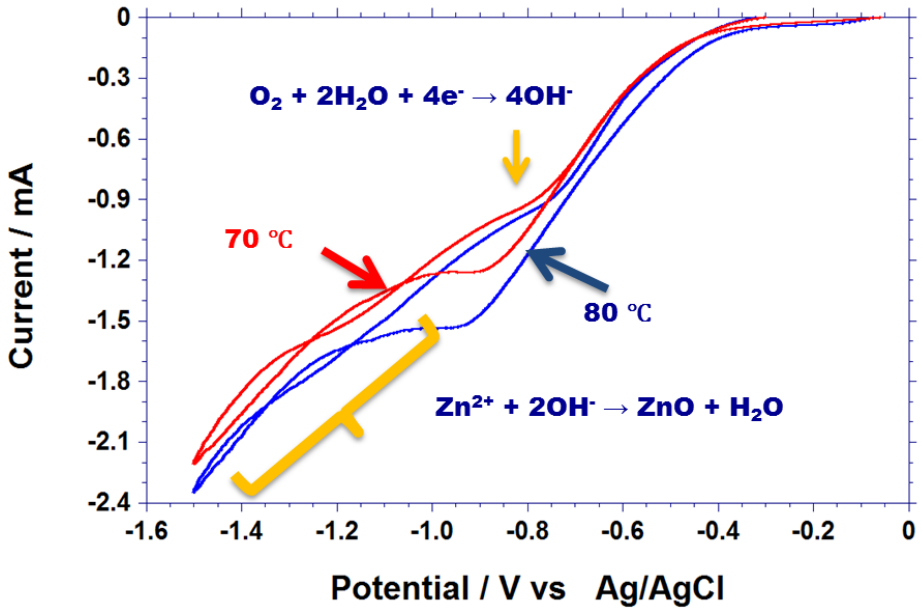

Figure 3-7. Current-Potential (I-V) measurement by potentiostat to find the condition for electrochemical deposition of ZnO nanomaterials; red: 70 ℃, blue: 80 ℃.

There is no ZnO nanowires growth from 0V to -0.5 V because of low current flow at the surface of working electrode, ITO substrate, in the solution which indicates nucleation does not occur on the ITO substrate that

is confirmed by FESEM. As matter of fact, ZnO nanowire growth is conducted at -1V vs Ag/AgCl reference electrode for all solutions to ensure that sufficient nucleation and growth are done within an hour. The important parameter for ZnO nanowires growth in aqueous solution is charge transferred from electrolyte towards electrodes. Potentiostat automatically calculated the charge which explains amount of ionic movement during electrochemical reaction.

$$Q = Current \times Time = I(A) \times t(s)$$

and measured charge transferred were

$$Q = 10^{-5} C \sim 3\ C$$

depending on the growth time and current density.

Since $One\ charge = 1.6 \times 10^{-19}\ C$, $6 \times 10^{13} \sim 1.8 \times 10^{19}$ charges have been moved between two electrodes during various growth conditions.

The possible zinc species in the electrolyte are Zn^{2+} ions, zinc hydroxide complexes including $Zn(OH)^{+}$, $Zn(OH)_2$, $Zn(OH)_3^{-}$, and $Zn(OH)_4^{2-}$, and zinc chloride complexes including $ZnCl^{+}$, $ZnCl_2$, and $ZnCl_3^{-}$. The predominant species depend on the pH and the temperature of the solution as shown in Figure 3-8. In the growth temperature range from 55 to 90℃ and pH from 5 to 6, the major zinc species are Zn^{2+}, $ZnCl^{+}$, $Zn(OH)^{+}$, and $ZnCl_2$. $ZnCl_2$ is a minor constituent in the temperature range from 55 to 90℃. However, all of the other major zinc species concentrations vary significantly as the temperature increases.

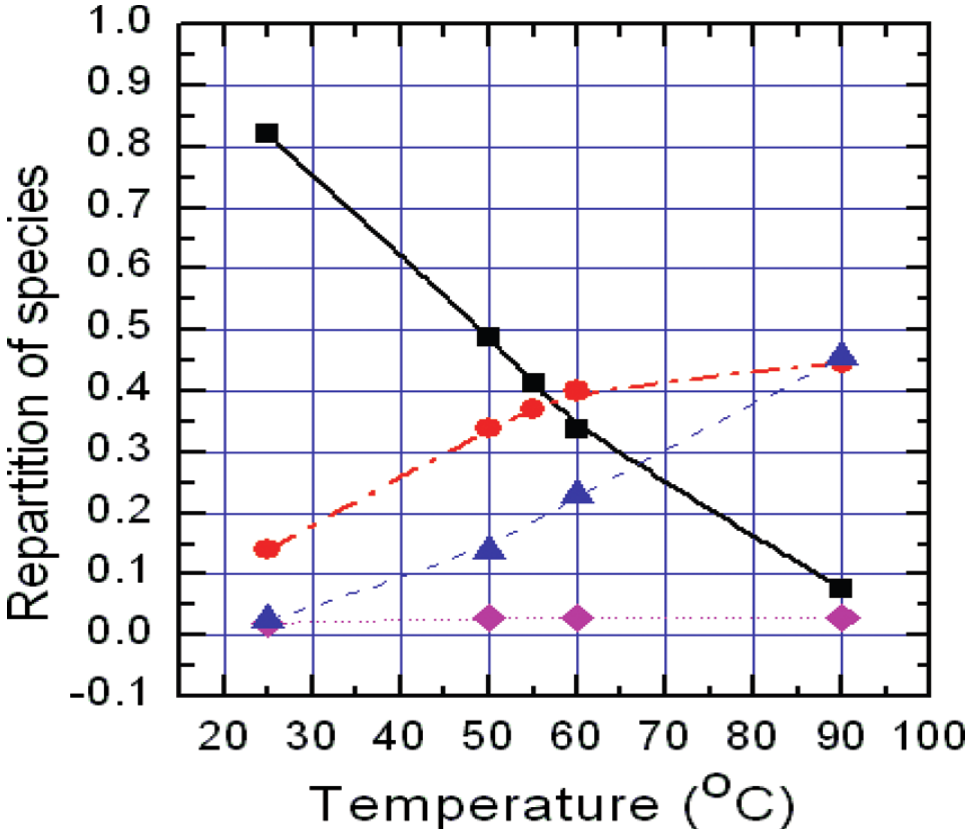

Figure 3-8. Zinc soluble complexes as a function of solution temperature at pH 6.5. Symbols represent different zinc species: (black) Zn^{2+}; (red) $ZnCl^{+}$; (blue) $Zn(OH)^{+}$; (purple) $ZnCl_2$.[86]

While electrochemical deposition occurred, the production of ZnO on the ITO substrate is described by

$$\frac{1}{2}O_2 + H_2O + 2e^- \rightarrow 2\,OH^-$$

$$Zn^{2+} + 2\,(OH^-) \rightarrow ZnO + H_2O$$

During an external potential application, reduction of oxygen occurs, leading the production of OH^- ions on the surface of the working electrode.

Holes enter the circuit via the counter electrode and oxidize $ZnCl_2$ to form Zn^{2+} ions and other Zn-related species. It is observed that the electrochemical deposition process may be divided into two distinct stages: a nucleation stage around 5 min, and a growth stage.

The nucleation stage on the cathode, ITO, is a very important step that mostly determines the nanowire's diameter and density. The nucleation rate depends on the OH^- and Zn^{2+} ion concentrations which depend on the current density and electromigration in the electrolyte solution. In addition, it is significantly affected by the applied external potential. If the potential is not sufficient, nucleation on the working electrode will not occur that is around 500 μA of current flow in our system. After the growth of ZnO nanowires in the solution for 1hr, the average dimension of nanowires was 100 nm in diameter and 500 nm in length.

3-4. Structural and optical properties of ZnO nanomaterials

In Figure 3-9, densely aligned ZnO nanowires clearly show hexagonal shape on top of them with smooth side facets. ZnO nanowires electrochemically deposited in 0.5 mM $ZnCl_2$ aqueous solution at -1V vs Ag/AgCl reference electrode which have the typical ZnO nanowires having perfect hexagonally faceted morphology. The number of nucleation site was 90/25 μm^2. However, it should be noticed that there are the nuclei which could not be transformed to a nanowire shape.

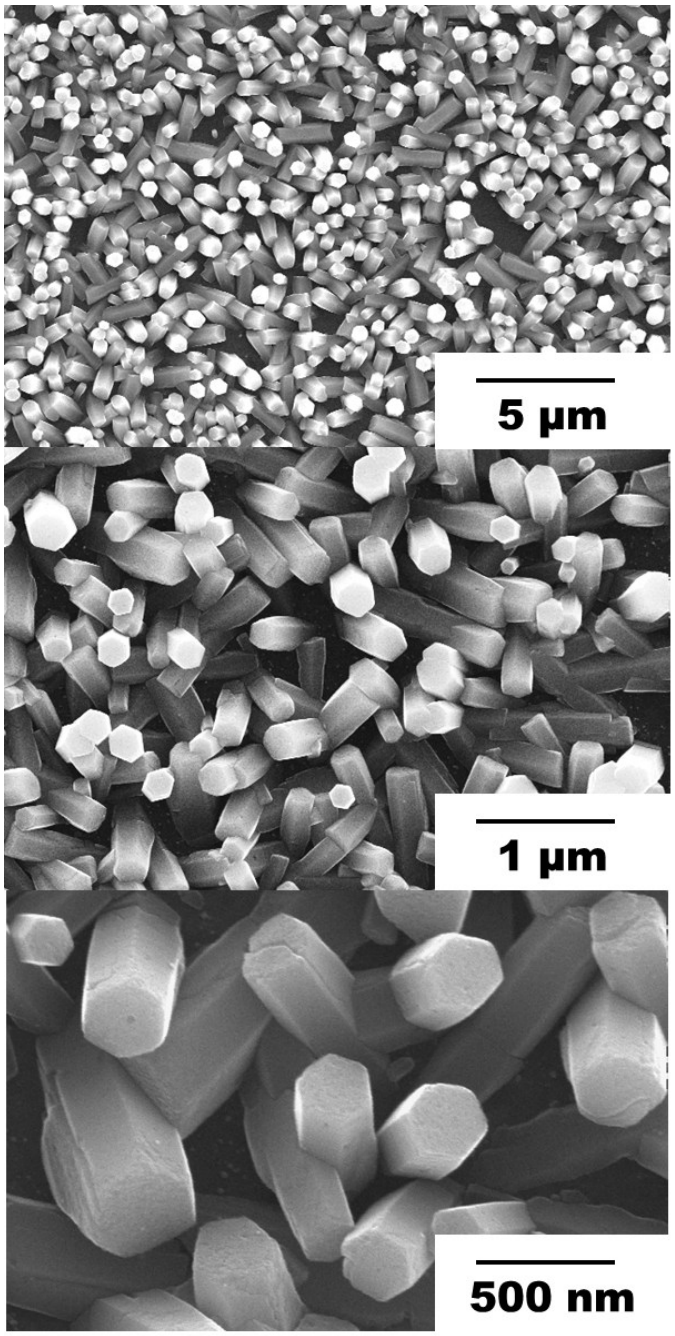

Figure 3-9. FESEM images of ZnO nanowires on seedless ITO substrate in 5 X 10^{-4} M $ZnCl_2$ with 0.1 M KCl solution with various magnification.

Photoluminescence spectra of ZnO nanowires array measured using a He-Cd laser (325 nm excitation) as the excitation source at a room temperature is shown in Figure 3-10.

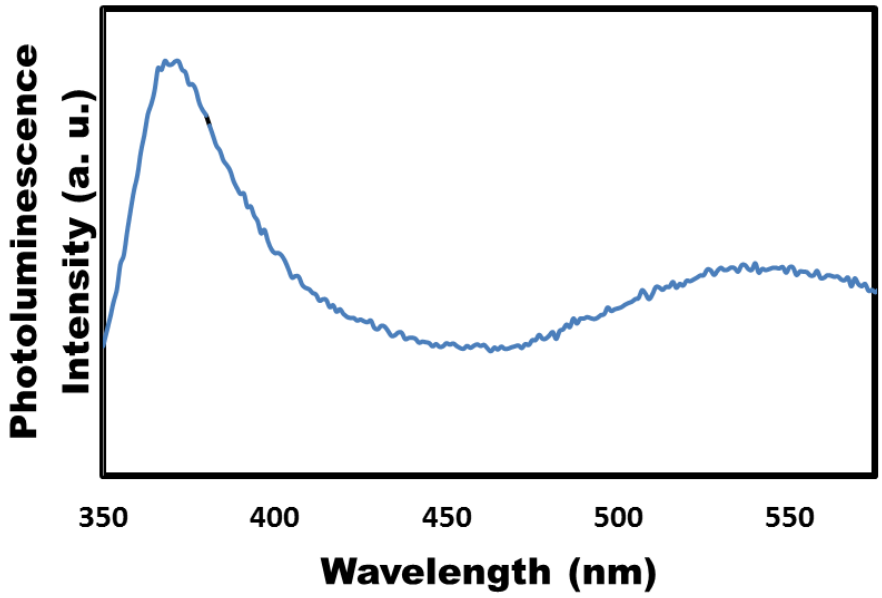

Figure 3-10. Photoluminescence spectrum of as deposited ZnO nanowires on seedless ITO measured at room temperature.

The narrow UV band at 3.26 eV (381 nm in wavelength) and a broad green band at 2.3 eV (about 540 nm in wavelength) are observed in the PL spectrum. The UV emission band must be explained by a near band edge transition of wide bandgap ZnO nanowires, namely the recombination of free excitons through an exciton–exciton collision process.[87] The appearance of UV band emission with low excitation intensity at a room temperature can be attributed to the radial quantum confinement effect of ZnO nanowire. The green band emission results from the radial recombination of a photo-

generated hole with an electron that belongs to a singly ionized oxygen vacancy.[88]

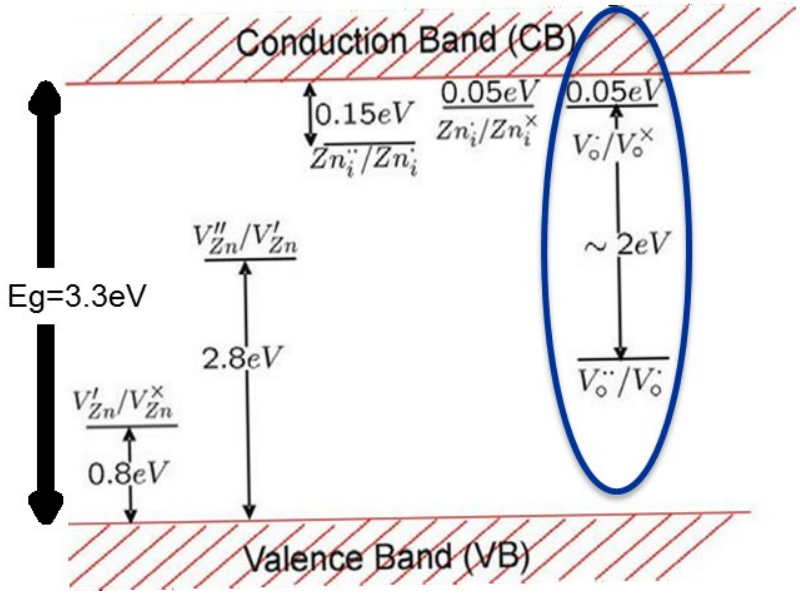

Figure 3-11. Schematic diagram of native defects in ZnO.[89]

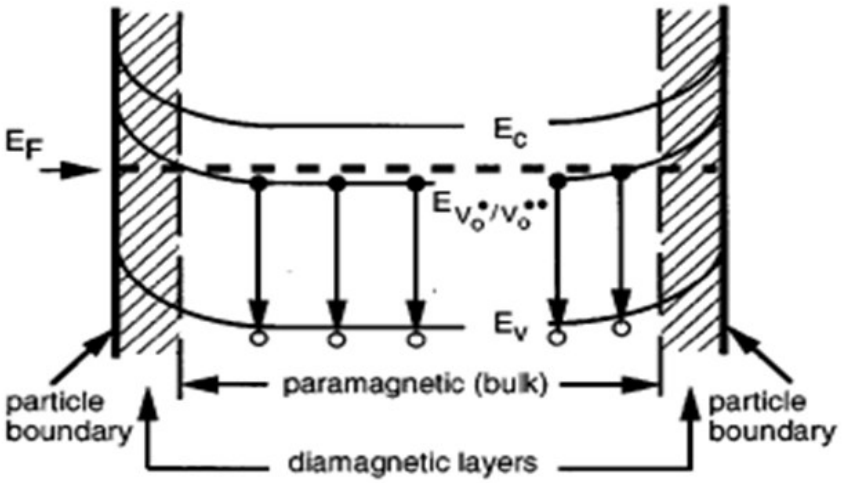

Figure 3-12. Schematic diagram of energy band diagram of ZnO.[88]

After annealing, all singly ionized oxygen vacancies are compensated with oxygen during annealing so that PL responsible for band edge excitation remains. Many researcher have been reporting the PL variation along different temperature and atmosphere during annealing. In this study, the temperature for annealing is 400 ℃ for 1 hr resulting in band edge emission only in PL spectrum from 350 nm to 580 nm shown in Figure 3-13.

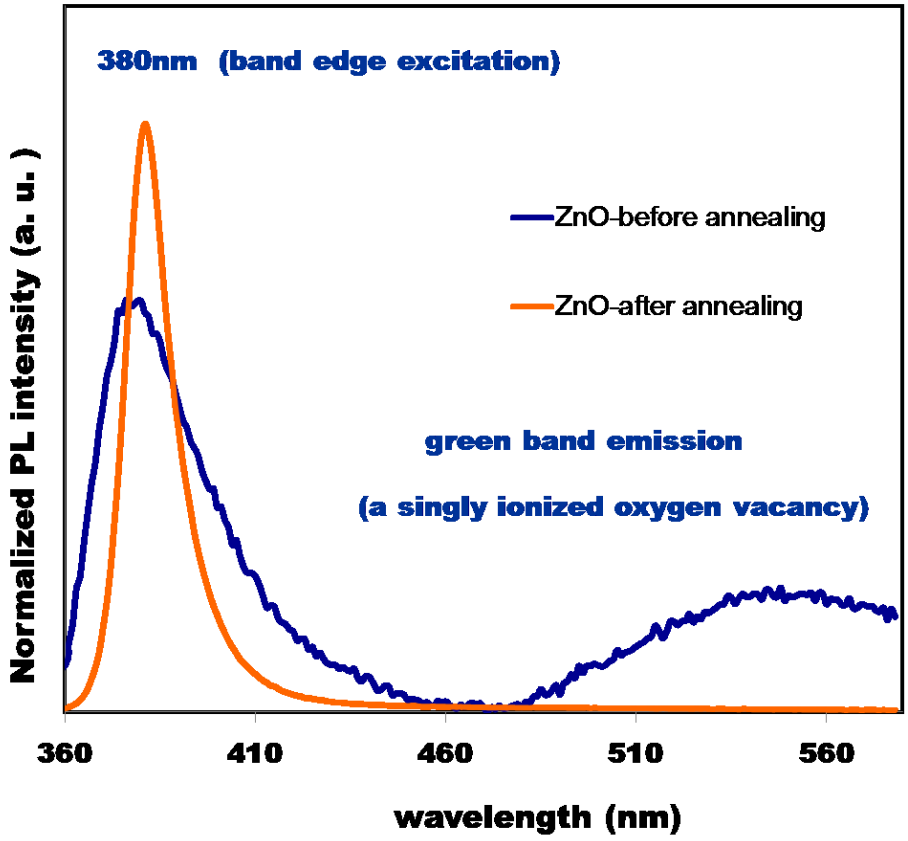

Figure 3-13. Photoluminescence spectra of ZnO nanowires showing annealing effect.

3-5. Dependence of ZnO nanowire growth on potassium chloride (KCl) concentration

The influence of KCl concentration on the structural property of ZnO nanowire has been investigated. The variation of the morphology as a function of the KCl concentration in the solution is discussed in this chapter. Xu et al. explained the effect of KCl during ZnO nanowire growth by the role of Cl^- ions attaching polar faces.[90] This is due to the fact that the rate of O_2 reduction (i.e., OH^- generation) decreases when Cl^- increases. Cl^- ions act as a stabilizer of the (0002) ZnO polar face. Figure 3-14 shows the morphologies of ZnO nanowires varies as potassium chloride concentration increases. Cl^- ions hinders the enlongation along [0001] direction due to the adherence of Cl^- ions on polar face prior to Zn^+ and OH^- approach resulting in the broaden hexagonal shape of ZnO nanodots.

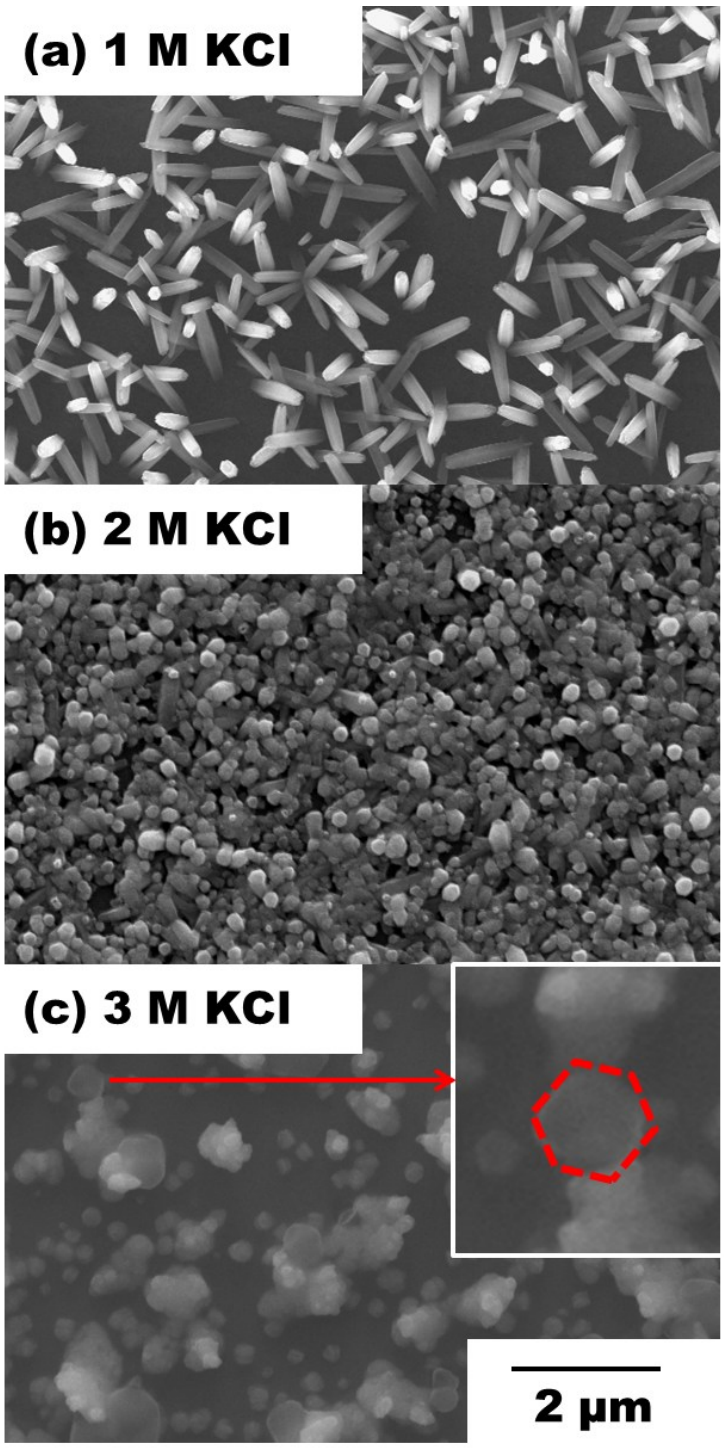

Figure 3-14. Effect of KCl Concentration on ZnO Nanowire Growth (a) 1 M, (b) 2 M and (c) 3 M KCl, respectively.

There is a certain range of KCl concentration where ZnO nanowires are grown preferentially longitudinal direction. With FESEM images, ZnO nanowire growth has been predicted. When the concentration of KCl is less than 1 M, Cl^- ions hinder diameter growth, favoring longitudinal growth, while when the concentration is larger than 1 M, diameter growth is favored. Figures 3-14 (b) and (c) clearly show that nanowires elongate their diameter and as KCl concentration increased up to 3 M, there is no vertical wires growth but nanoplates were formed. The growth of ZnO nanowire should be kept in the range of less than 1 M of KCl concentration to ensure nanowire structure instead of plate or film formation.

3-6. Dependence of ZnO nanowire growth on substrate species

During ZnO nanowire growth was performed by electrochemical deposition method, the first nucleation stage is critical for nanowire growth direction which affects final shape of nanowires such as nanowires, nanodots, nanoflowers and dendrites. In this chapter, the effect of substrate on ZnO nanowire growth was investigated by comparison of ITO, silicon, titanium silicide and copper transmission electron microscopy grid containing carbon film as substrates.

It is obvious that ZnO nanowire growth strongly depends on the substrate crystal structure. As shown in Figure 3-15, ZnO nanodots were created on silicon surface while nanoflowers were main morphology of ZnO crystal on titanium silicide surface.

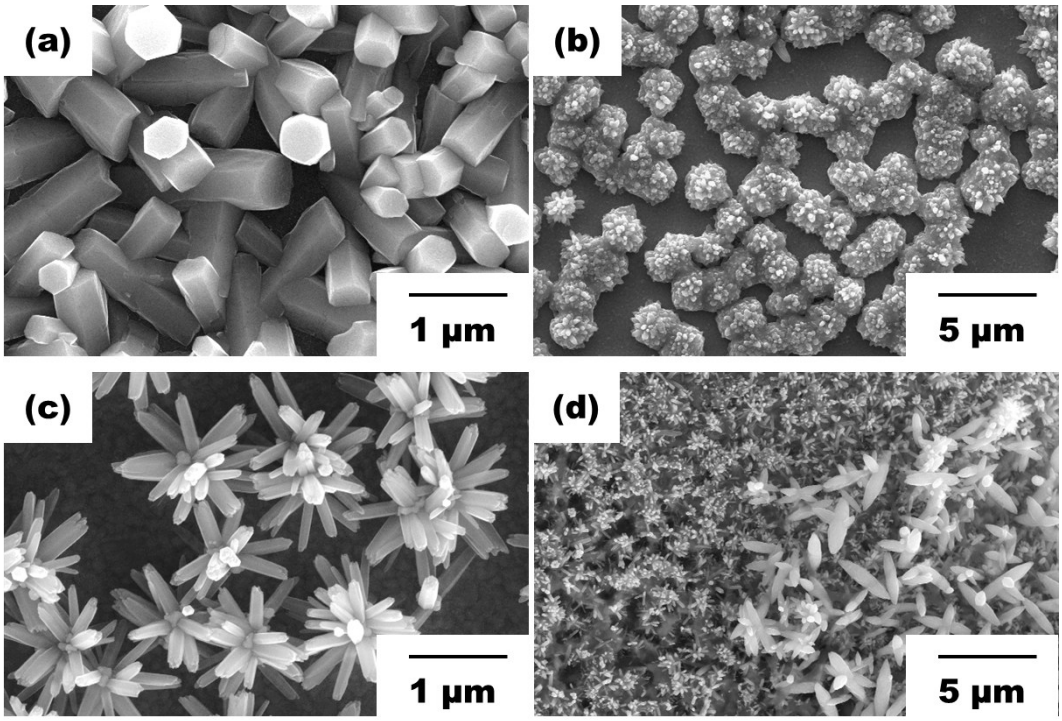

Figure 3-15. FESEM images of various morphologies of ZnO nanocrystal depending on substrates, (a) ITO Substrate, (b) silicon substrate, (c) titanium silicide substrate, and (d) TEM grid.

It was of interest that ZnO nucleation occurred not only on copper part of TEM grid but also on amorphous carbon film that was partially attached on copper grid. The dependence of substrate is believed that ZnO nuclei crystal structure, whether it is single crystal or polycrystal, was followed by substrate crystal then the growth direction was determined by nuclei's favorable growth direction. The substrate dependence on ZnO nanowires growth is still under investigation to enhance their application to organic photovoltaics.

3-7. ZnO nanowires growth on transmission electron microscopy (TEM) grid having copper frame with carbon film

In the previous chapter, the growth dependence of ZnO nanowires on various substrates has been investigated. In this chapter, deeper investigation of ZnO nanowires on a TEM grid will be discussed.

In this work, ZnO nanowires were grown on TEM grid from $ZnCl_2$ aqueous solution at low temperatures (~ 80 °C). The morphology of the ZnO nanowires could be tuned easily by adjusting the concentration of Zn^{2+} precursor, growth temperature, time and pH. The solution contained a mixture of reagent grade 5×10^{-4} M zinc chloride ($ZnCl_2$) and 0.1 M potassium chloride (KCl) as a supporting electrolyte without any further purification. Oxygen was bubbled into the solution, prior to the start of growth and the oxygen bubbling was continued until the deposition ended. Zinc oxide deposition was done using a potentiostat (CH Instrument 610B) applying a constant potential of -0.9 V versus a silver (Ag)/ silver chloride (AgCl) reference electrode in a saturated KCl solution. The working and counter electrodes were a TEM grid and a platinum wire, respectively.

In order to prevent the carbon film loss from copper frame, the growth time was kept 10 minutes which results in successful growth of ZnO nanowires both on carbon film and copper frame.

Transmission electron microscopy (Dr. Theodore) and field emission scanning electron microscopy (FESEM, XL-30) were used to analyze the morphology of nanowires.

The size of TEM grid is typically 3 mm in diameter and thin copper plate with carbon film on it as shown in Figure 3-16. Copper frame has been fully covered with ZnO nanowires and some part of carbon film has been survived after ZnO nanowire deposition in $ZnCl_2$ aqueous solution.

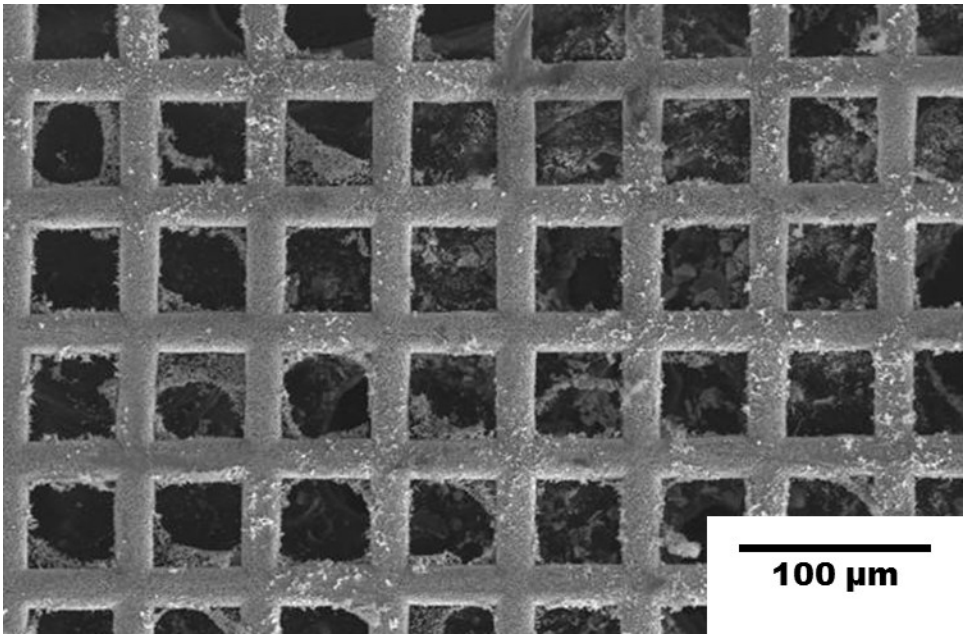

Figure 3-16. A TEM grid having ZnO nanowires both on copper frame and carbon film.

In order to prevent the copper chloride ($CuCl_2$) formation that will significantly change the pH of the solution resulting in undesirable growth condition and keep ZnO nanowires on carbon film during the ZnO nanowires growth, the growth time must be less than 10 minutes at 80 ℃. After 10 minutes growth, the white ZnO nanocrystals cover the copper frame and partially cover the carbon film. The FESEM images of as-grown ZnO nanowires on a TEM grid are summarized in Figure 3-17. ZnO nanowires on copper frame are well aligned normal to the substrate which indicates [0001] direction of growth while there is no specific direction of ZnO nanowires on

carbon film due to the characteristic of amorphous carbon film. The density of nanowires is critically influenced by the number of nucleation site where the diameters of nanowires are determined by the size of nucei.

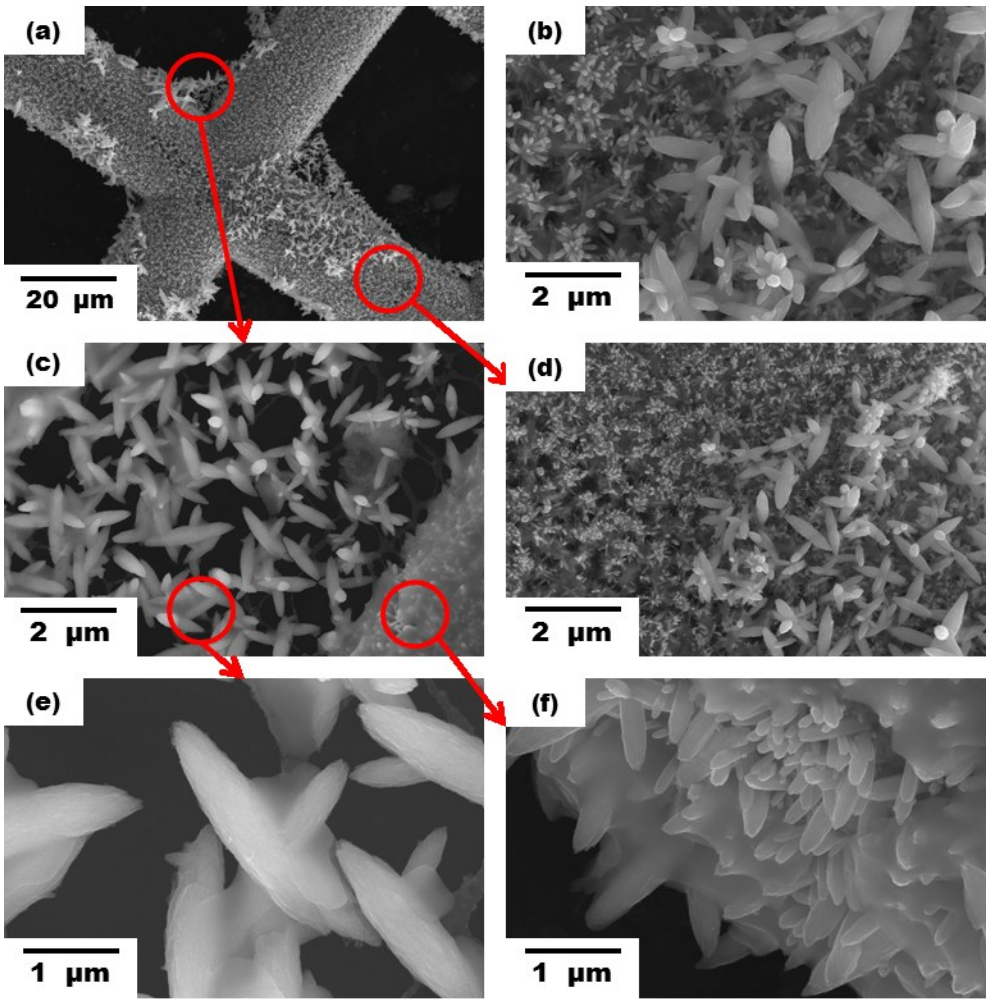

Figure 3-17. ZnO nanowires on a TEM grid with various magnifications.

ZnO nanowires are grown both on the copper frame and carbon film simultaneously. Carbon film is partially removed during the growth due to the temperature of the solution and weakening of bonding between the

carbon film and copper frame. Figure 3-17 shows different tendency of ZnO growth depending on substrate material. As shown in previous chapter, the crystal structures of ZnO on different substrates result in different orientation preference. However, an amorphous carbon film covering TEM grid has significantly different nucleation and growth process.

Firstly, it is simply understood that ZnO nanowires on copper frame having quasi-hexagonal shape due to the short growth time are grown by root-growth model. The next interesting part is ZnO nanowires grown on the carbon film. Even though the conductivity of carbon film is not defined here, it is obvious that carbon film works as a conductive substrate which supplies nucleation sites for ZnO. Typically, the ZnO nanowires grown for 30 min exhibit mean lengths of 500±50 nm and mean diameters of 100±50 nm on conductive substrate such as ITO coated glass, *etc*. However, in this study, the growth rates are influenced by substrate species. The average diameters of ZnO nanowires on carbon film and copper frame are 500 nm and 100 nm, respectively. This result indicates that the arrival rate of zinc ions is much higher on carbon film than copper frame resulting in 5 times larger in diameter, 4 times longer in length.

The size of the nanowires is controlled simply by changing the growth time although it is also affected by other growth parameters such as temperature and concentration of source materials. However, it has to be note that the growth time is critical to recognize the ZnO nanowires on TEM grid because the nanowires growth more than 10 minutes, all carbon film has

been removed from the frame into the solution where the film is drifting around.

Transmission electron microscopy (TEM) has been employed for further investigation of structural characteristics. In Figure 3-18, low magnification TEM image shows typical morphology of individual and cluster of ZnO nanowires. While the ZnO nanowires on copper frame show similar diameter of 100 nm and length of 500 nm, those on carbon film have 500 nm in diameter and 2 μm in length with sharp tips at both edges of nanowires.

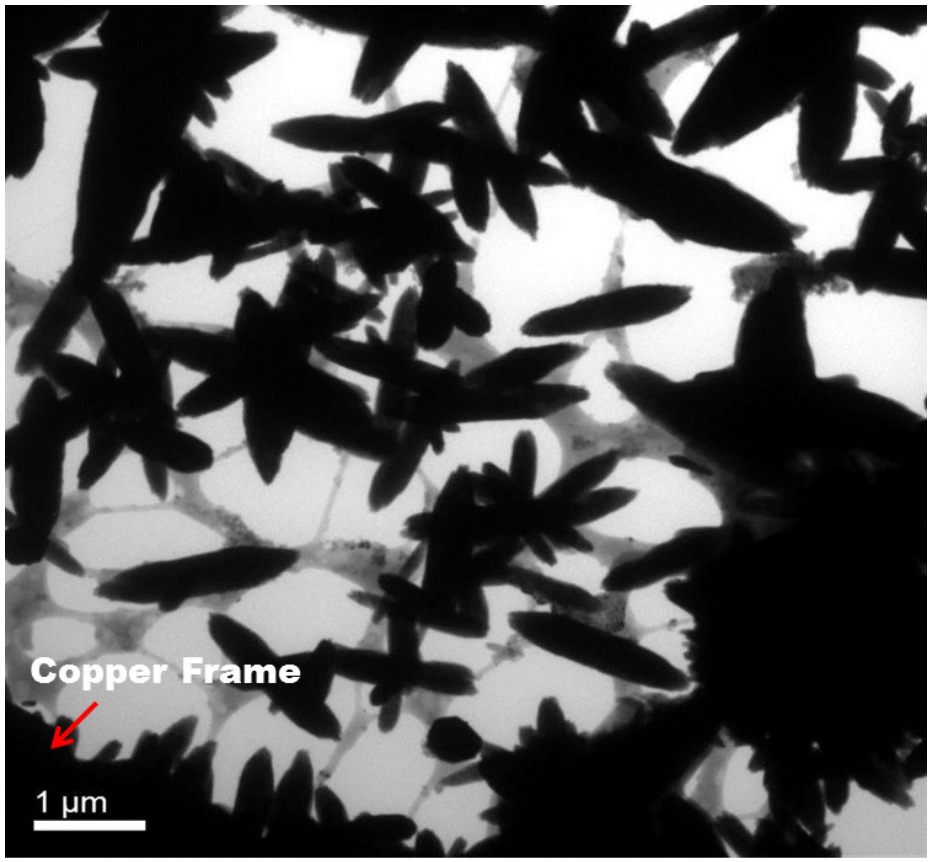

Figure 3-18. A low magnification TEM image of ZnO nanowires on a TEM grid.

ZnO nanowires having thin diameter (less than 50 nm) grow as a bundle individually at initial nucleation and growth stage and eventually coalesce to make large diameter nanowires (~500 nm) to minimize surface energy. As shown in Figure 3-10 of high magnification TEM images, the smaller nanowires are formed on top of bundle nanowires. When smaller nanowires are coalesced together, there are several dislocations at the interface of the walls. Since the growth time is relatively short (10 min), there are not enough time for zinc atoms to be diffused into other nanowires, the dislocations are generated.

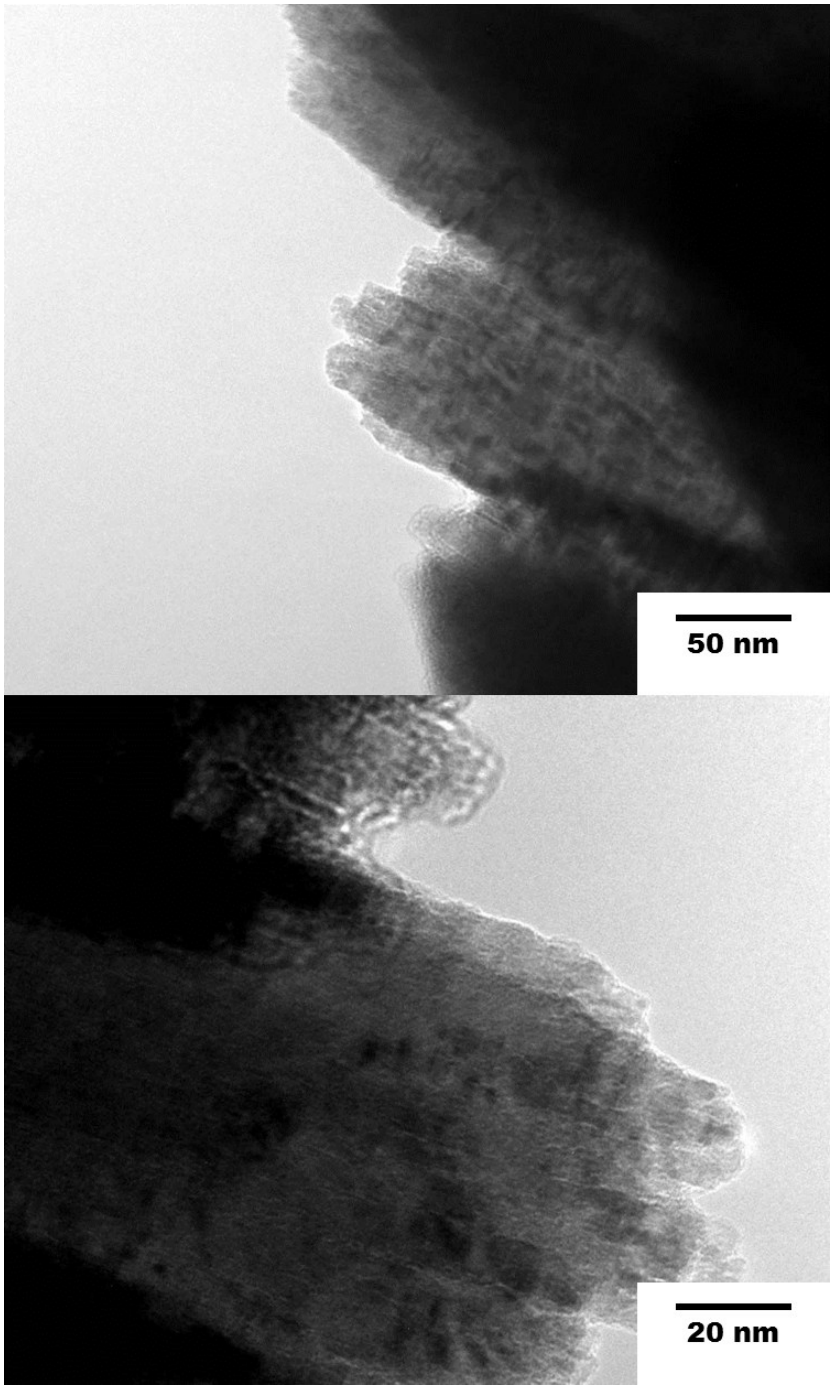

Figure 3-19. High magnification TEM images of ZnO nanowires on the carbon film.

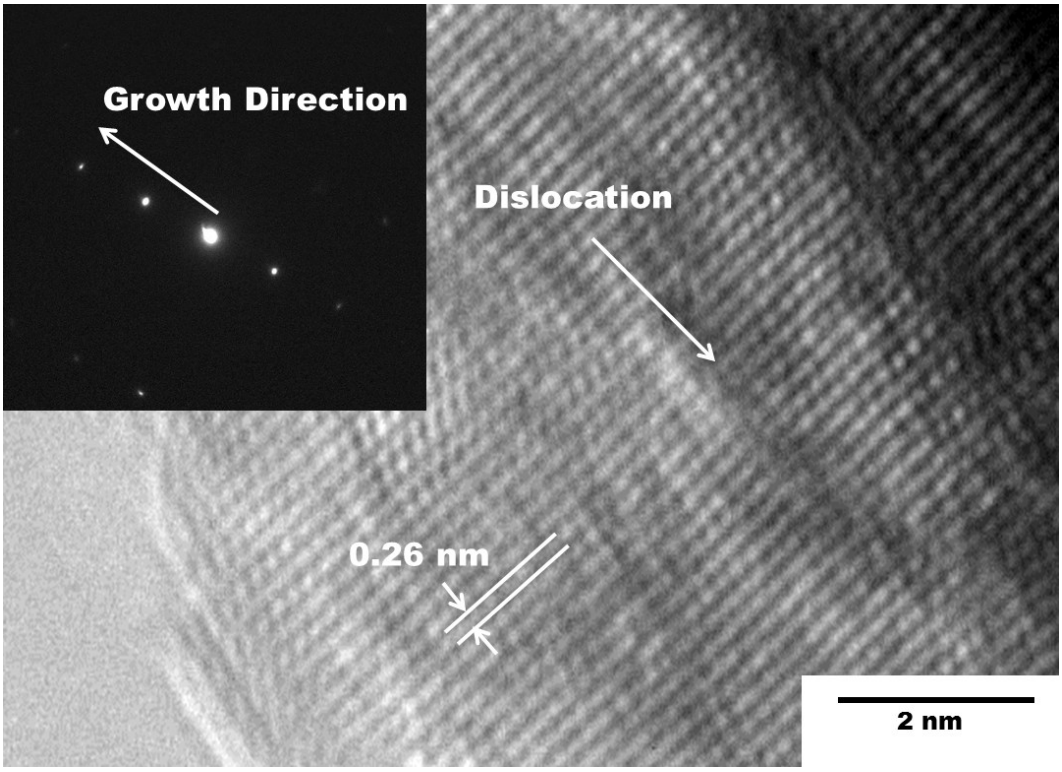

Figure 3-20. A high resolution TEM image of ZnO nanowire having dislocations grown on carbon film, the inset is a SAED pattern of ZnO nanowire.

The high resolution TEM and SAED results explain that [0001] is the preferred growth direction for ZnO nanowires. Lattice spacing of 0.26 nm corresponding to the *d*-spacing of the wurtzite ZnO (0002) plane indicating that the small ZnO nanowire before it forms the bundle is single crystal in nature and preferentially grows along [0001] direction (*c*-axis), which is confirmed by the SAED pattern. As indicated in Figure 3-20, the dislocation is formed at the interface between adjunct small nanowires. These dislocations can be compensated if nanowires are annealed at temperatures

higher than 400 ℃ for an hour or long enough growth time during electrochemical deposition.

In conclusion, we have successfully grown ZnO nanowires on TEM grid in $ZnCl_2$ and KCl aqueous solution within 10 minutes. The morphology of ZnO nanowires is influenced by the species of conductive substrates investigated by high resolution TEM and SAED pattern. Electrochemically deposited ZnO nanowires have a hexagonal crystal structure having 0.26 nm *d*-spacing of the wurtzite ZnO (0002) plane. We observed a wide range of ZnO nanowires diameter distribution grown on carbon film by the FESEM images that indicates more than 4 times magnitude both in lengths and diameters compared to those on the copper frame. The results in this study show that ZnO nanowires can be grown on carbon-based materials which supply enough nucleation sites when their forms are even nanodots or nanowires and independent on their crystallinity. By depositing ZnO nanomaterial directly on to TEM grid, the investigation for dependence of ZnO nanomaterials on solution types can be easily achieved.

3-8. ZnO nanowires growth on gold (Au) seed layer

Thin layer of gold was deposited on ITO to investigate the seed layer dependence on ZnO nanowires growth. . ZnO nanowires had random orientation of their vertical growth direction without seed layer shown in Figure 3-21 (a) while vertically aligned ZnO nanowire were grown on gold seed layer in Figures 3-21 (b) and (c).

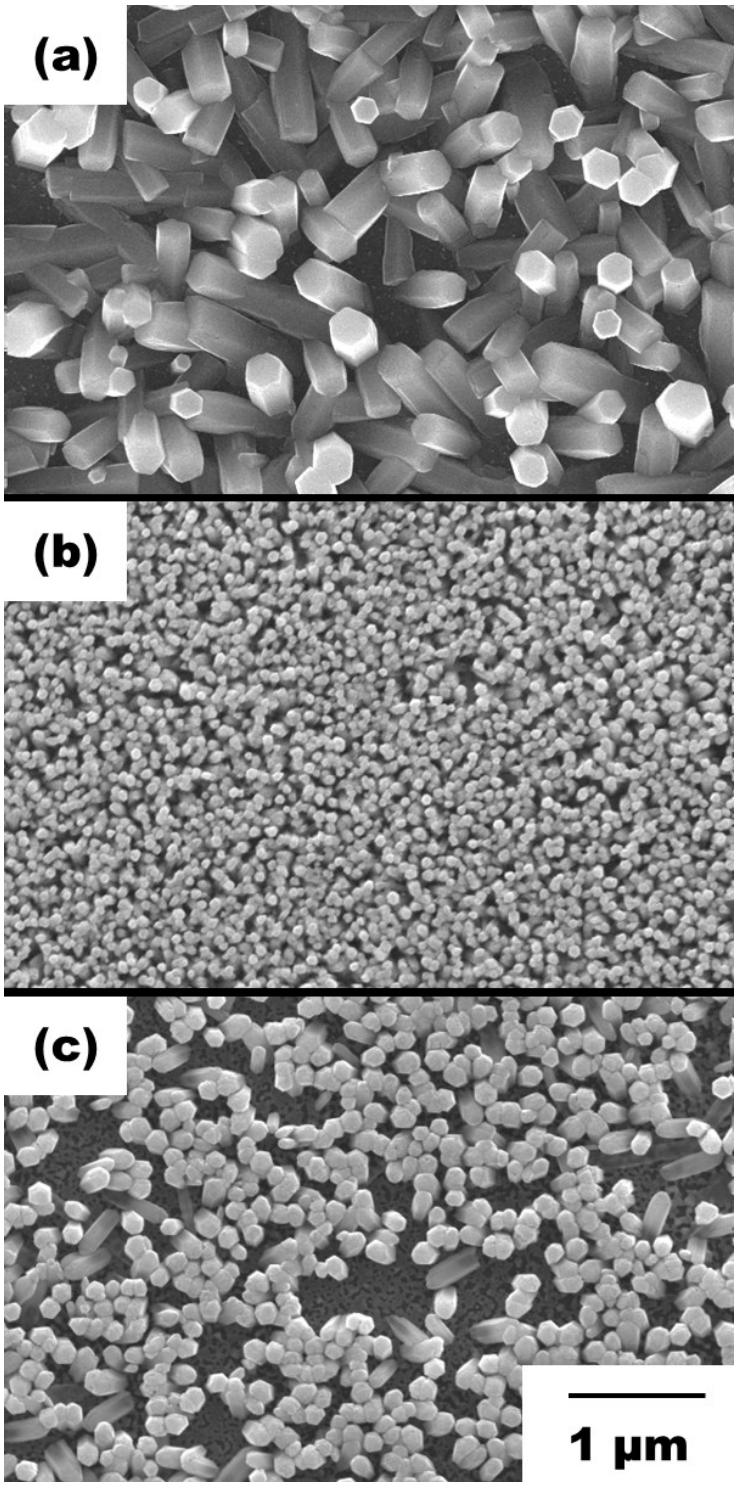

Figure 3-21. The seed layer dependence on ZnO nanowire growth, (a) seedless, (b) Au 2min and (c) Au 4min deposition.

A seed layer of gold supplied more nucleation site and plays a critical role of directional growth when ZnO nucleus was formed at the interface of gold and the solution. As matter of fact, ZnO nanowires on thicker seed layer have larger diameter which has larger grain size of gold layer that directly influences the diameter of ZnO nanowires. As shown above, perfectly vertical ZnO nanowire can be grown on gold seed layer which is able to act as both seed layer and cathode electrode.

Figure 3-22 shows the result of ZnO nanowires on 1" X 1" ITO substrate having gold seed layer grown for 1 hour in aqueous zinc chloride solution at 80 ℃. The length of ZnO nanorod arrays is 1 μm with hexagonal shape with areal density of 100 per 100 μm^2. The color of ZnO arrays is white under sun light.

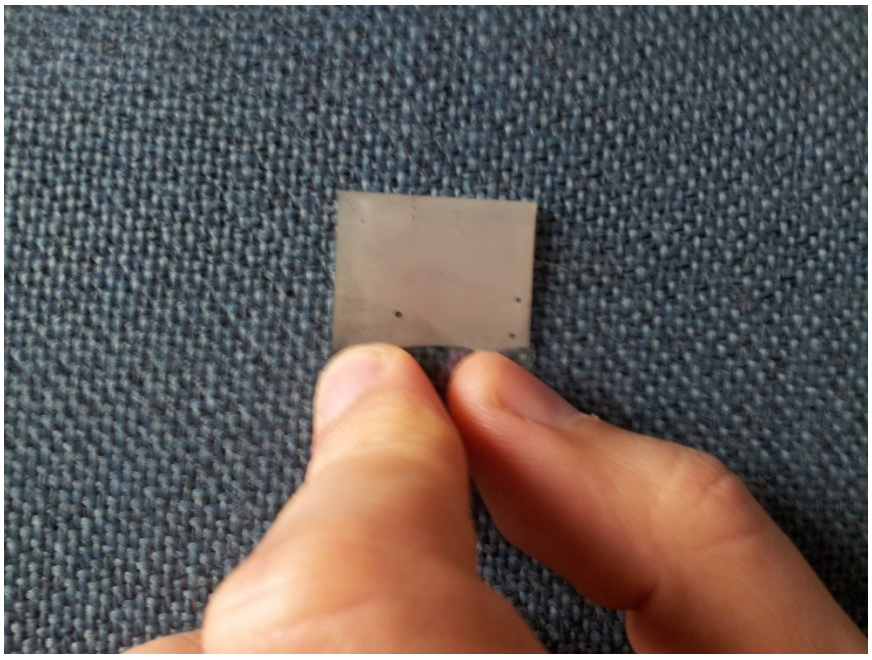

Figure 3-22. 1 μm ZnO nanorod arrays on 1" X 1" ITO substrate.

The length of ZnO nanowires is directly related with the growth time when the concentrations of $ZnCl_2$ and KCl are fixed. The $ZnCl_2$ and KCl concentrations for ZnO nanorod arrays in Figure 3-22 are 5 X 10^{-4} M and 0.1 M with distilled water, respectively. The gold seed layer acts as orientation modification layer which allows perfect vertical growth normal to the substrate. The diameter of ZnO nanowires was influenced by the thickness of seed layer where thicker layer exhibits larger diameter of ZnO nanowires. This seed layer thickness enables the control of areal density of nanowires with perfect hexagonal crystal shape of ZnO.

3-9. Summary

In this chapter, several parameters for 1-dimensional nanowires growth such as concentrations of source materials, zinc chloride ($ZnCl_2$) and potassium chloride (KCl) and substrate dependence having different crystal structures including carbon films on a TEM grid have been conducted.

When the concentration of KCl is less than 1 M, Cl^- ions hinder diameter growth, favoring longitudinal growth, while when the concentration is larger than 1 M, diameter growth is favored.

ZnO nanowires can be grown on carbon-based materials which supply enough nucleation sites when their forms are even nanodots or nanowires and independent on their crystal structures. By depositing ZnO nanomaterial directly on to a TEM grid, the characterization of ZnO nanomaterials on carbon-based substrates without damaging samples or preparation steps can be easily achieved.

CHAPTER 4

THE OPTIMIZATION OF ZINC OXIDE NANOROD ARRAYS FOR ORGANIC BULK-HETEROJUNCTION SOLAR CELLS

4-1. Introduction to ZnO nanorod arryas for organic bulk heterojunction solar cells

Zinc oxide (ZnO) has widely used for electronic and photonic devices, sensors, photodetectors and solar cells due to its direct wide bandgap (E_g = 3.3 eV at 300 K), and compatibility to devices requiring thermal and chemical stability. Additionally, the nanostructured forms of ZnO have several advantages including good transparency and high electron mobility.[1-4, 91] Morphology of ZnO nanostructure performed by electrochemical deposition has several issues particularly for various pH, growth temperature, and source materials.[92-93] The electrochemical deposition of ZnO nanostructure can be formed by application of a constant voltage between working and counter electrodes provided by potentiostat operating at low temperatures (< 80 °C).[94-97]

Tremendous effort has been devoted to the improvement of solar cells based on conjugated polymer as a potential alternative source of electrical energy. Photoactive materials, device structures and fabrication processes have been developed to enhance the device performance based on organic bulk-heterojunctions.[98-99] Organic bulk-heterojunction solar cells formed from blended poly (3-hexythiophene) (P3HT) and (6,6)-phenyl C_{61} butyric acid methyl ester (PCBM) exhibits efficiencies near 5% with optimized device

structure and fabrication conditions.[100] Most commonly, charge extraction is achieved by using an indium tin oxide (ITO) substrate. It has a high work function, as the positive electrode (anode) and where aluminum (Al) layer has a low work function metal and serves the negative electrode (cathode). The ITO extracts holes from the active layer through a hole transport layer while simultaneously the negative electrode extracts the electrons.[101] On the other hand, previous investigations have demonstrated that ZnO-based inverted solar cells make the better selective electron contact layers due to the high mobility of ZnO when compared to titanium oxide (TiO_2) layers. In addition, ZnO layers prevent oxidation and result an increase in the life time of photovoltaic devices.[102-105] The inverted device structure with a ZnO layer either thin film or seeded epitaxially grown nanostructure is favorable in terms of energy level balance. However in this work, we demonstrate nanostructured organic solar cells using ZnO nanorod arrays on the seedless ITO that exploit the reduction of surface reflection in order to improve the efficiency of bulk-heterojunction solar cells consisting of P3HT:PCBM blends.

4-2. Device fabrication of ZnO nanostructured organic bulk heterojunction solar cells

All devices in this work were prepared on 20 Ω sq^{-1} ITO coated glass substrates. These ITO substrates were cleaned in ultrasonic bath of acetone, methanol, and isopropanol, followed by an ultraviolet ozone (UVO) treatment. The growth of ZnO nanorod arrays was prepared by electrochemical

deposition method using potentiostat in 0.1 mM zinc chloride aqueous solution at a relatively low temperature (80 °C). A platinum wire and silver (Ag)/ silver chloride (AgCl) electrode in saturated potassium chloride (KCl) were used as the counter and reference electrodes, respectively. After ZnO nanostructure formation at constant voltage of -1 V, a conductive poly (3,4-ethylenedioxythiophene) poly (styrene sulfonate) (PEDOT:PSS) was used as a hole transport layer. The PEDOT:PSS layer was spin-coated at 5000 rpm for 1 min, resulting in a layer thickness of 30 nm after baking at 150 °C for 15 min. The photoactive layer of P3HT:PCBM blends were dissolved in 1, 2-dichlorobenzene with a mixing ratio of 1:1 by weight. The photoactive layers were obtained by spin-coating of the blend at 600 rpm for 1 min, which corresponded to a thickness of 250 nm. The metal cathode (LiF/Al) was thermally evaporated in a vacuum chamber through a shadow mask at a pressure of 1×10^{-7} Torr to finalize an active area of 0.2 cm^2.

4-3. Device performance of ZnO nanostructured organic bulk heterojunction solar cells

Current density-voltage (J-V) measurements were done using simulated AM 1.5 global solar irradiation (100 mW/cm^2) using a xenon-lamp based solar simulator (Spectra Physics Oriel). The light source was calibrated with a standard Si photodiode reference cell (Hamamatsu) prior to measurement. External quantum efficiencies (EQEs) were analyzed by a quantum efficiency measurement system (QE) and UV-VIS transmittance-

reflectance spectra were obtained in the air (Cary 5000 spectrophotometer). The morphology of as-deposited ZnO nanostructure and ZnO/PEDOT:PSS structures were characterized with the use of a field emission scanning electron microscope (FESEM, XL-30) and an atomic force microscope (AFM).

The morphologies of ZnO nanorod arrays grown on seedless ITO are shown in Figure 4-1. Densely aligned ZnO crystals are composed of both isolated nanorods and several nanorods simultaneously grown on a nucleus partially covering the substrate.

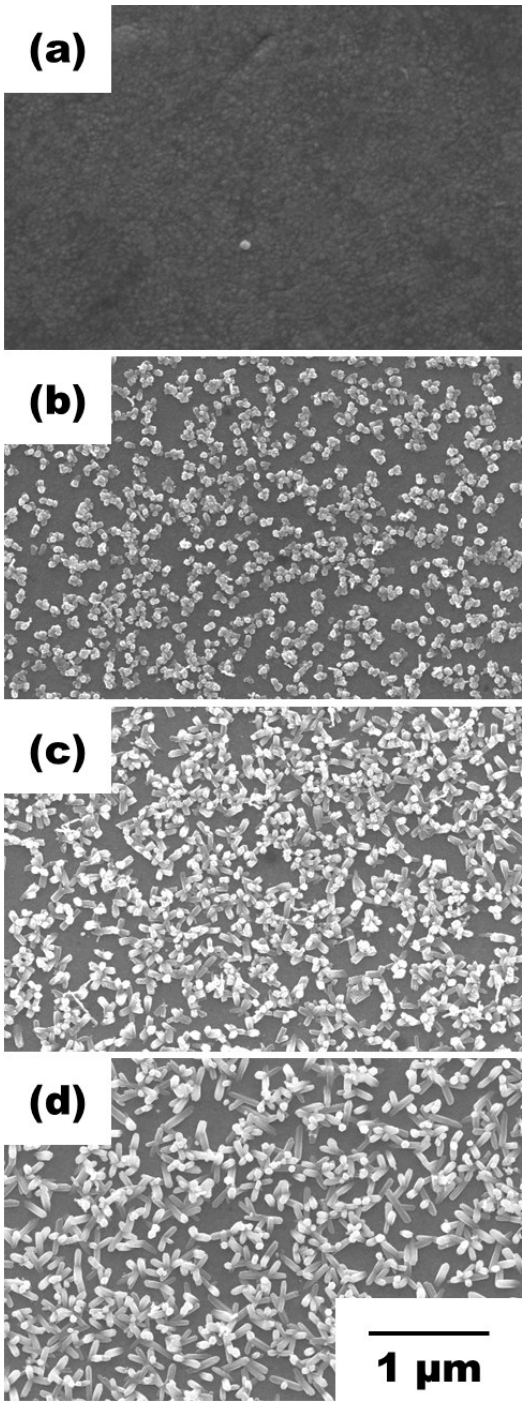

Figure 4-1. Field emission scanning electron microscopy (FESEM) images of (a) ITO, (b) ITO/ ZnO (100 nm), (c) ITO/ZnO (300 nm), and (d) ITO/ZnO (500 nm), respectively.

By controlling the concentration of the Zn^{+} source, the temperature during electrochemical deposition, and the pH of aqueous solution, no catalyst is required for the formation of ZnO nuclei. ZnO nanorods are single crystals following the crystal planes of ZnO nucleus. It can be found that hexagonal columnar grains grown in the direction perpendicular to the substrate with {101} side facets. The length of ZnO nanorods has been controlled by growth times of 15 min, 30 min, and 1 hr and corresponded to thicknesses of 100 nm, 300 nm, and 500 nm, respectively.

Addition of PEDOT:PSS layer on ITO/ZnO nanostructure shows critical variation of interface morphology between a hole transport layer and an active layer as shown in Figure 4-2.

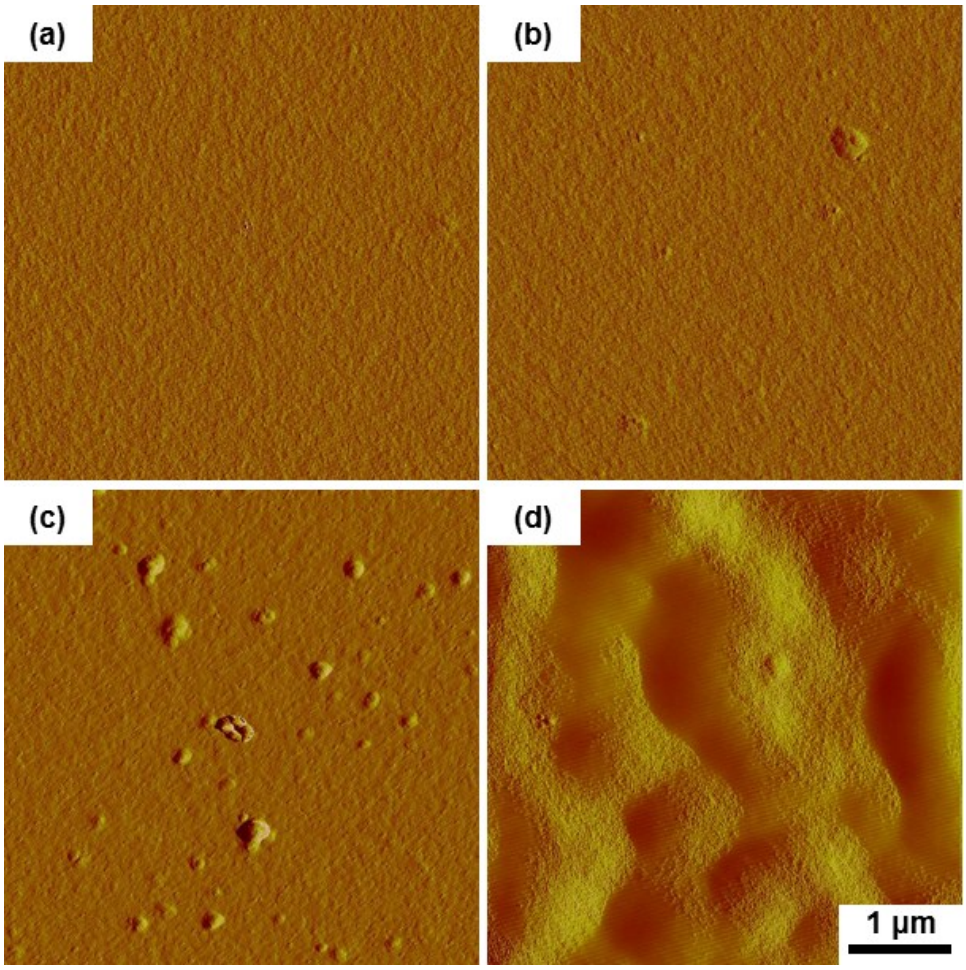

Figure 4-2. AFM surface images of PEDOT:PSS surfaces on (a) ITO, (b) ITO/ ZnO (100 nm), (c) ITO/ZnO (300 nm), and (d) ITO/ZnO (500 nm), respectively.

The RMS roughness for ITO/PEDOT:PSS is 1.3 nm; while, the surfaces of ITO/ZnO/ PEDOT:PSS structures with 100, 300, and 500 nm ZnO nanostructure have RMS values of 1.6, 6, and 20 nm (5 μm × 5 μm scan), respectively. Morphology of interface plays an important role for both charge transport and collection in devices. Few of the ZnO nanorods penetrate the PEDOT:PSS layer and reach the active layer. As shown in AFM images of

Figure 4-2, the surface becomes much smoother as the length of ZnO nanorods get shorter.

Figure 4-3 displays the current density-voltage (J-V) characteristics of the ZnO nanostructured organic bulk-heterojunction solar cells having structures ITO/(ZnO)/ PEDOT:PSS/P3HT:PCBM/LiF/Al with and without ZnO nanorod arrays under AM 1.5 global solar irradiation with an intensity of 100 mW/cm^2. The short-circuit current density (J_{sc}), open-circuit voltage (V_{oc}), fill factor (FF), and power conversion efficiency (PCE) derived from the J-V curves for nanostructured organic solar cells are summarized in Table IV.

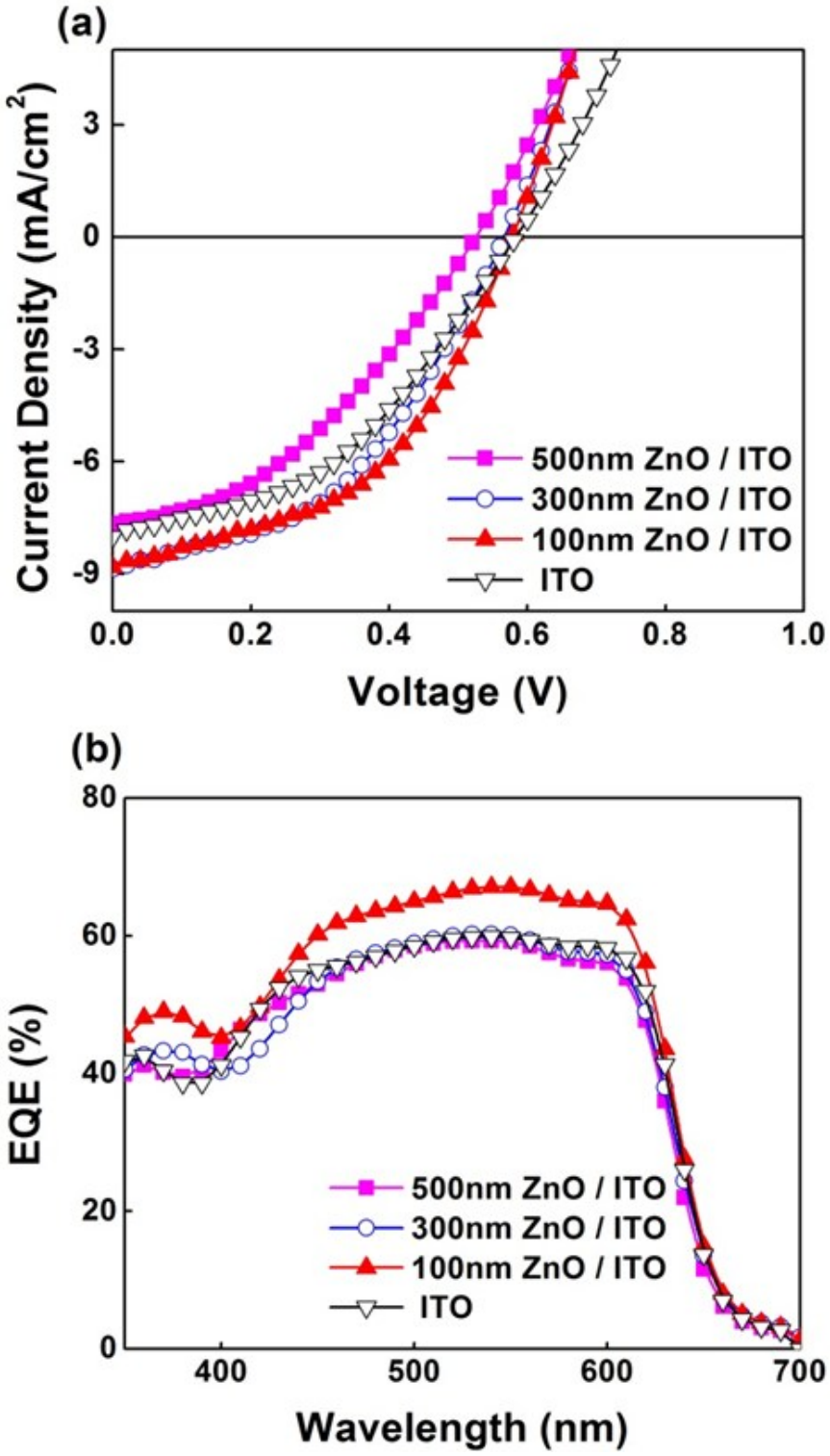

Figure 4-3. (a) Current density-voltage (J-V) characteristics and (b) external quantum efficiency for various length of ZnO nanostructured organic solar cell.

Table IV. The summary of device parameters of ZnO nanostructured Solar cells

	V_{oc} (V)	J_{sc} (mA/cm^2)	FF (%)	R_{sh} (Ω cm^2)	R_s (Ω cm^2)	Eff. (%)
ITO	0.58	8.0	42	266	13	1.9
100 nm ZnO	0.58	8.8	47	217	7.5	2.4
300 nm ZnO	0.57	8.8	44	183	8.8	2.2
500 nm ZnO	0.53	7.7	38	327	14.7	1.5

The device without ZnO nanorod arrays shows a V_{oc} of 0.58 V, a J_{sc} of 8 mA/cm^2, a FF of 42% that resulting in a PCE of 1.9%. While, the PCEs of the devices with ZnO nanorod arrays are dramatically improved 1.5%, 2.2%, and 2.4% as the length of ZnO nanorods decreases. Both short-circuit current density and fill factor clearly show enhancement over the devices using 100 nm and 300 nm length of ZnO nanorod than without ZnO nanorod arrays. However, a solar cell with the length of 500 nm ZnO nanorod arrays on seedless ITO shows a significant decrease in open-circuit voltage (0.53 V) when compared to 0.57 ~ 0.58 V for the others. One of the reasons for the decrease of V_{oc} for 500 nm of ZnO nanorod arrays might be due to the fact that the work function of ZnO is lower than ITO leading to the less difference of the work function between ITO/ZnO and Al than that of ITO and Al; even though, ZnO arrays does not fully cover the ITO surface. With the decrease of

ZnO length, FF increases from 38%, 44%, and 47%; whereas, the device without ZnO layer remains 42%.

The constant J_{sc} of 8.8 mA/cm^2 on ZnO nanorod length of 100 nm and 300 nm implies less contribution of the polymer/ZnO interface for the charge separation than that occurs at the P3HT:PCBM photoactive layer.[106] From the Figure 4-3, ZnO layer does not act as a hole blocking layer owing to the coverage on ITO but work as a facilitating photocurrent generation layer. Takanezawa*, et al.* explained the hole blocking effect by the ZnO layer resulting in the decrease of the efficiencies.[106-107] However, we do not encounter this issue for ZnO nanorods shorter than 500 nm. This result is supported by comparison of transmittance/reflectance spectra of ITO/ZnO nanorod arrays shown in Figure 4-4. It is known that the transmittance of the oxide layer plays a key role in the device performance. Figure 4-4 shows the optical transmittance spectra of the layers with or without ZnO nanorod arrays. It can be observed that all the ZnO nanostructure layers show good optical transmittance. For a bare ITO substrate, the transmittance is about 80% over the visible wavelength range. After electrochemical deposition of ZnO nanorods, the gradual shift is occurred towards 380 nm corresponding to the energy gap for ZnO with increased nanorods length.

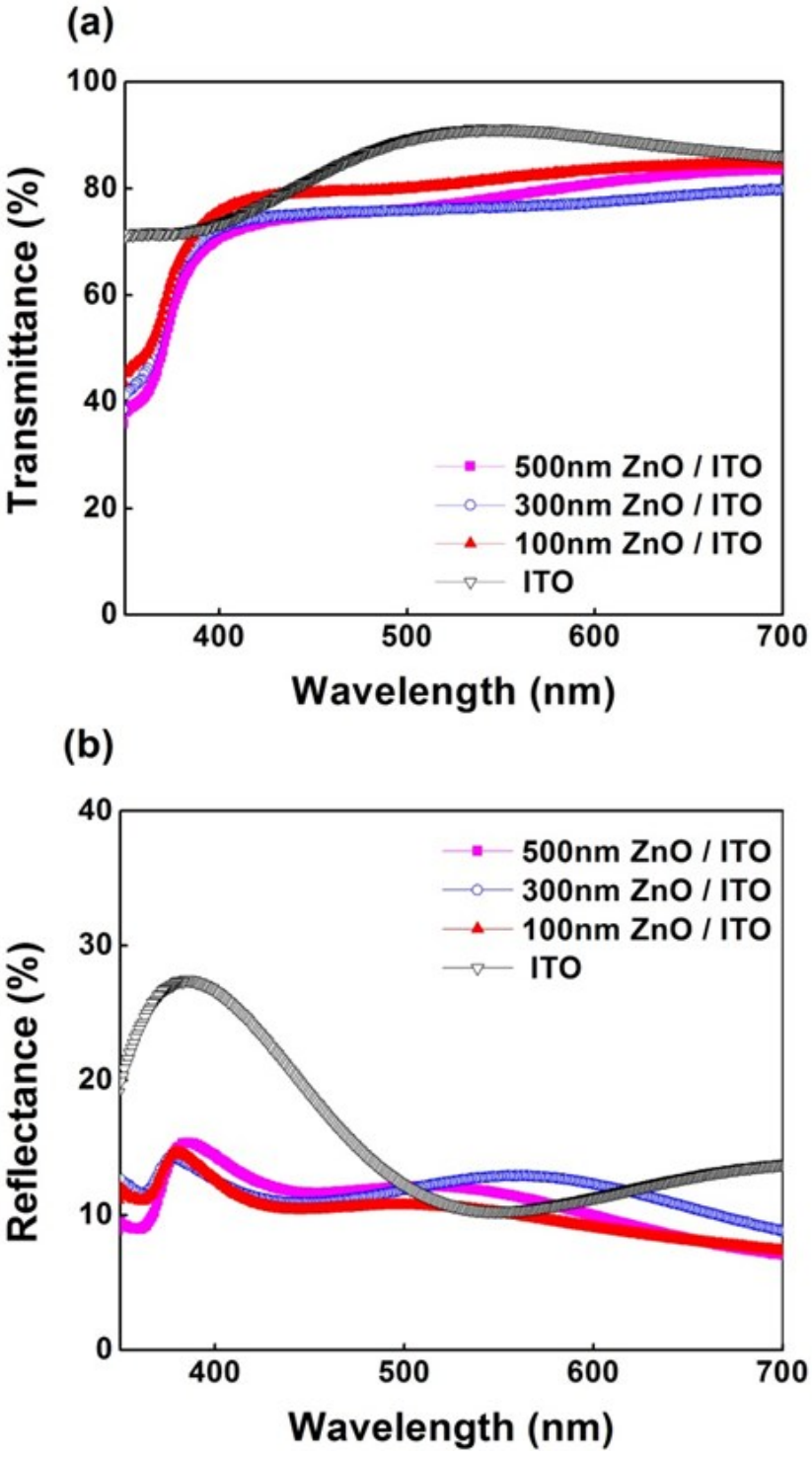

Figure 4-4. (a) Transmittance and (b) reflectance spectra of ZnO nanostructures on seedless ITO.

A first prominent visual observation is that the ZnO layers significantly reduce reflectance on ITO coated glass below 500 nm of wavelength as shown in Figure 4-4 (b). The decrease of reflectance at the interface of ITO/ZnO arrays induces more photocurrent as dictated by the EQEs spectra in Figure 4-3 (b). The resulting broader and lower reflectance spectra with 100 nm and 300 nm of ZnO nanorod arrays allows for more photons striking the photoactive layer to be transmitted through the transparent electrode and eventually produces more electron-hole pairs at lower wavelengths. It is worth to mention that exciton formation is partially governed by the wavelength range below 500 nm in this study that J_{sc} reaches 8.8 mA/cm^2 having 300 nm and100 nm ZnO nanorod arrays on seedless ITO substrate.

4-4. Summary

In conclusion, nanostructured organic solar cells based on an electrochemically deposited ZnO antireflection layer with improved efficiency and good growth stability have been simply fabricated on seedless ITO glass. It is found that it is critical to control absorption of photons through P3HT:PCBM layer at lower wavelength up to 500 nm in order to obtain the bulk-heterojunction photovoltaic devices, resulting in better power conversion efficiency. We conclude that the electrochemical deposition of ZnO nanorods is a very promising technique and further contribute to improve the device

performance for the large area, low temperature, and cost effective photovoltaic devices.

Chapter 5

ENHANCED DEVICE PERFORMANCE OF NANOSTRUCTURED SOLAR CELLS BASED ON CONTROLLED ZINC OXIDE AREAL DENSITY

5-1. Yttrium doped ZnO nanowire growth

Zinc oxide is a potential transparent conducting oxide (TCO) material due to its good optical and electrical properties. Other transparent conducting oxides such as aluminum doped ZnO and gallium doped ZnO have been extensively applied as transparent electrodes for organic light emitting diodes, solar cells and liquid crystal displays.[108-111] ZnO doped with rare earth metals shows great promise for spintronic applications.[112-113] However, very few studies of yttrium doped ZnO have been reported in the literatures.[23, 114-117] In this chapter, a simple method for the deposition of 1-dimensional yttrium doped ZnO nanowire arrays, with large scale uniformity, prepared by electrochemical deposition was investigated. Doping yttrium into ZnO nanowires can be a novel research area not only for transparent conducting materials but also for optical, electrical, photonic and nanostructured photovoltaic applications.

The growth by electrochemical deposition of a 1-dimensional ZnO nanostructure that occurs in an aqueous solution is the result of a chemical reaction at the surface of electrodes that are in contact with an ionically conducting phase with charge transfer among them. Such a solution based technique has been proposed as an alternative approach for mass production of metal, semiconductor and oxide nanomaterials with good control of

morphology and composition and with high reproducibility. In addition, solution-based growth of ZnO nanowires is of particular interest for vertically aligned ZnO nanowire arrays due to the technique's low cost, low temperature, and uniform growth. In this technique, a selective reaction produces nanocrystals with elongation along a favorable direction to form nanowires.[88,112,119]

5-2. Structural and optical properties of yttrium doped ZnO nanomaterials

Figure 5-1 shows FESEM images of yttrium doped ZnO nanowires with increasing yttrium concentrations. The micrographs reveal a significant yttrium concentration dependence of the surface morphology of the ZnO nanowire arrays.

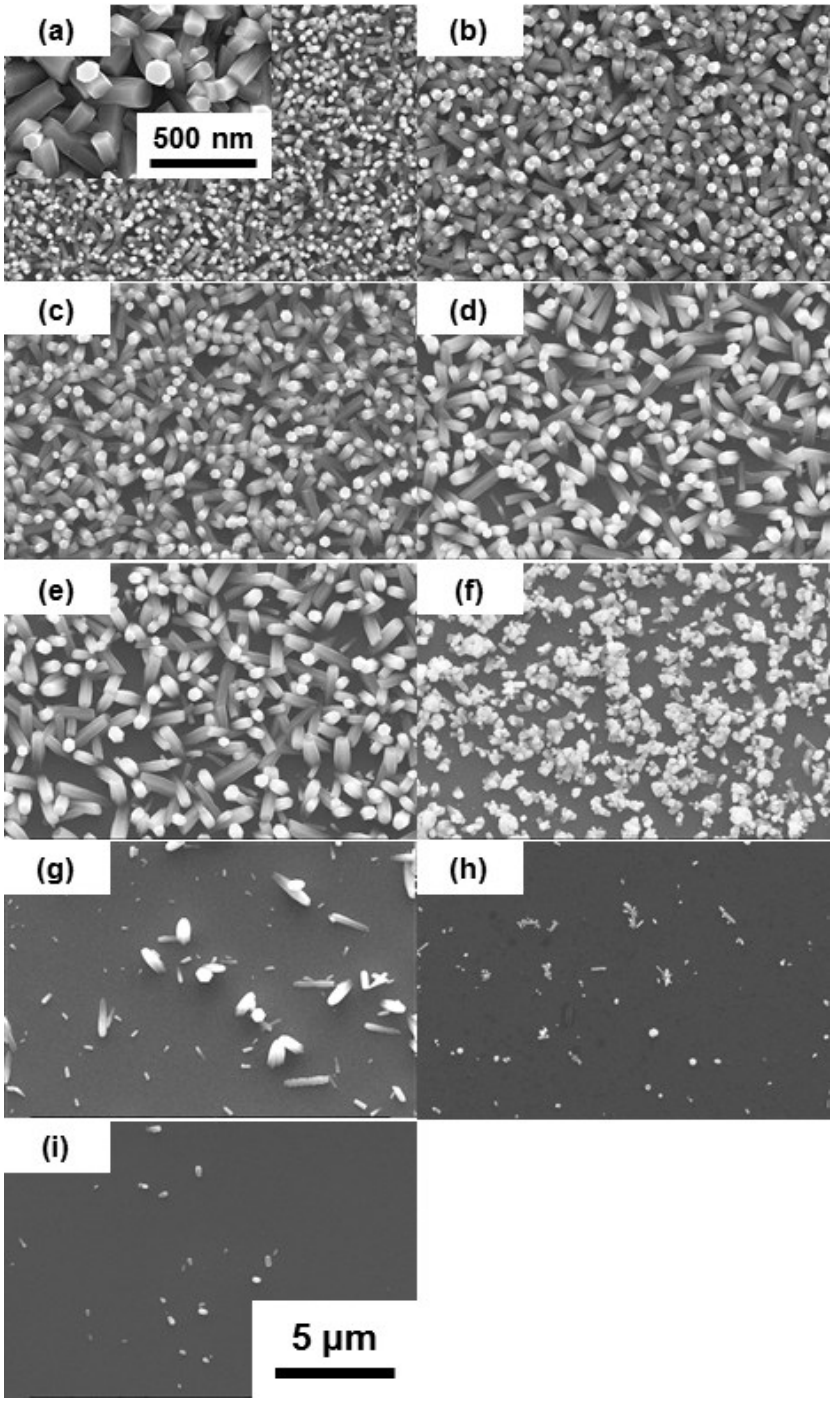

Figure 5-1. FESEM images of yttrium doped ZnO nanowires, (a) undoped, (b) 0.01 mM, (c) 0.02 mM, (d) 0.03 mM, (e) 0.05 mM, (f) 0.08 mM, (g) 0.10 mM, (h) 0.12 mM, and (i) 0.15 mM, on seedless ITO coated glass.

A first observation is that the diameter of the nanowires increases as yttrium concentration is increased upward from 0.01 mM. Continuous increase of the diameter occurs until the yttrium concentration reaches 0.05 mM, after which the diameter of the nanowires abruptly decreases. In addition, nanowires grown from solutions greater than 0.08 mM yttrium concentration, show significant decreases in both diameters and length. Joo *et al.* recently explained this phenomenon based upon face selective growth.[120]

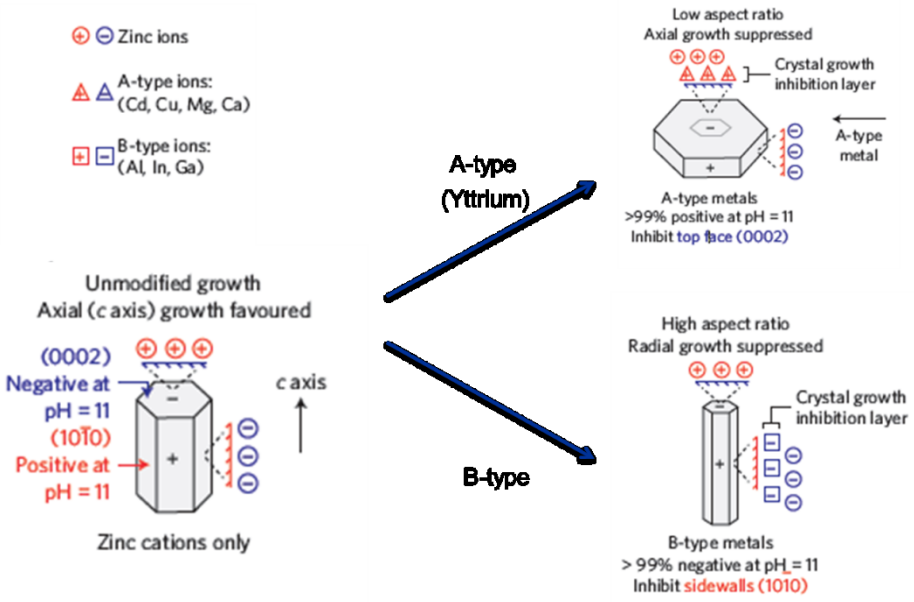

Figure 5-2. Rational control over ZnO nanowire morphology by means of face-selective electrostatic crystal growth inhibition.[120]

The addition of a small amount of yttrium chloride into the solution slightly changes the aspect ratio of the nanowires, due to positively charged

yttrium ions being attracted to the negatively charged top (0002) face. This suppresses growth along the preferred *c*-axis by limiting the access of zinc ions. In addition, we propose that yttrium ions are also attracted towards the surface of ITO, which results in a reduction of the number of nucleation sites (hindering the nucleation of ZnO nanowires) as yttrium doping concentration increases.

Figure 5-3 (a) shows that an increase with yttrium concentration inhibits the nucleation of ZnO on the ITO surface for concentrations up to 0.05 mM, with moderate continuation of the effect, up to 0.15 mM. The number of nucleation sites obtained from Figure 5-1, determined while excluding multiple nanowires simultaneously grown from a nucleus, indicates that yttrium ions play a key role in the nucleation process. When no yttrium source is applied to the solution, the average nucleation sites for undoped ZnO nanowires are 90 per 100 μm^2. The nucleation areal density rapidly decreases with increasing yttrium concentration until the nucleation site density is 25 per 100μm^2 for 0.05 mM yttrium concentration in the solution. The average diameter of the nanowires as calculated from the image in Figure 5-1 (a) is 150 nm for undoped ZnO nanowires. Meanwhile, the average diameters of the ZnO nanowires increase from 170 nm up to 210 nm when yttrium concentrations are 0.01 mM and 0.05 mM, respectively.

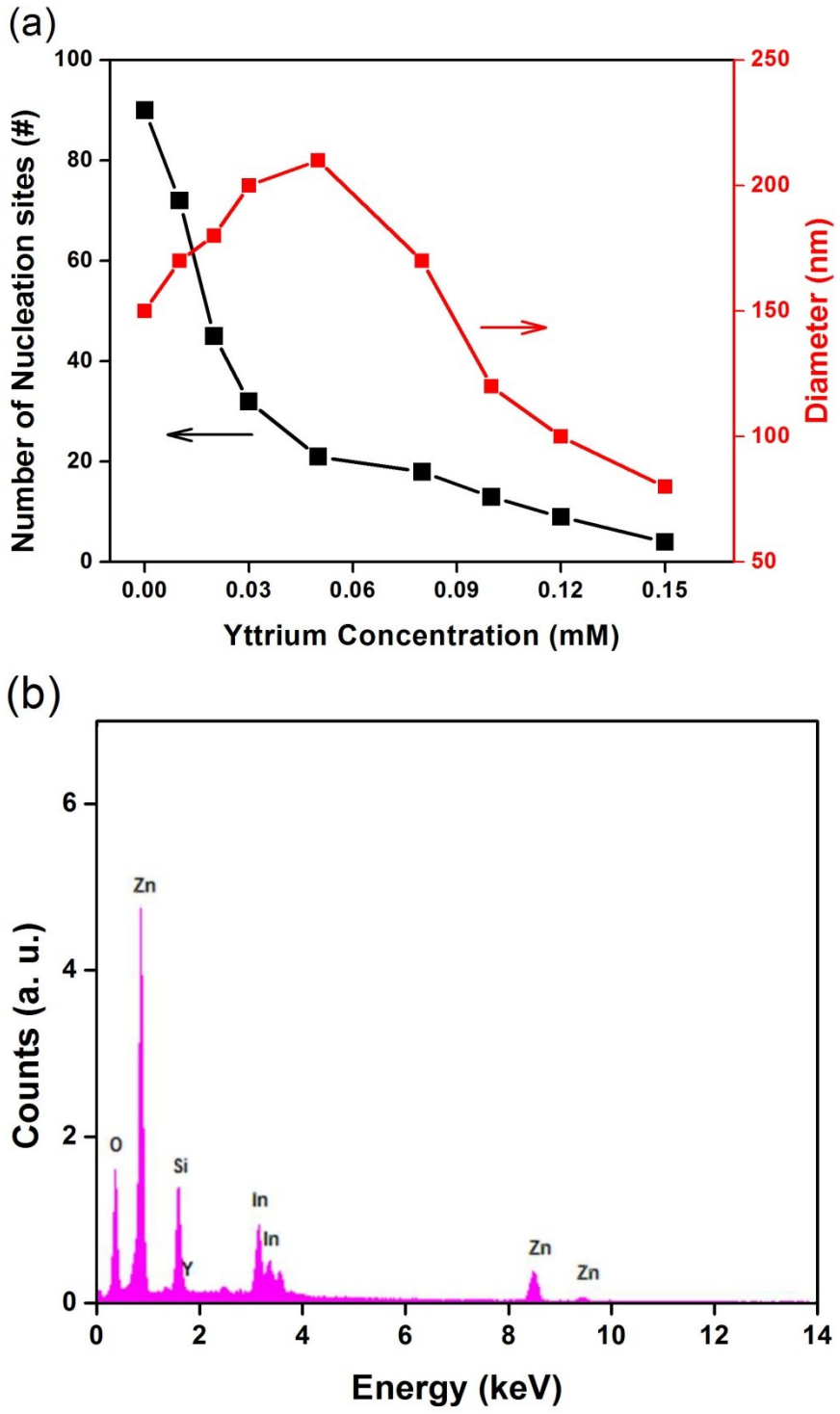

Figure 5-3. The number of nucleation sites of yttrium doped ZnO and X-ray dispersive spectroscopy for 0.03 mM yttrium doped ZnO nanowire array.

An energy dispersive X-ray spectroscopy (EDS) spectrum of electrochemically grown ZnO nanowires in the presence of 0.03 mM yttrium concentration shows an observable yttrium peak near 2 keV in Figure 5-2 (b). The yttrium to zinc atomic ratio, for 0.03 mM of yttrium content, is 0.014 as determined by EDS, which value is different from the desired yttrium doping concentration. Deficiency of yttrium might be due to the fact that only a small portion of the yttrium ions interact with the zinc ions, while most of the yttrium ions play a role in the inhibition of the nanowire nucleation.

Figure 5-4 shows XRD patterns obtained from yttrium doped ZnO nanowires fabricated from $ZnCl_2$ aqueous solution on a seedless ITO substrate. It is evident from the data that the (0002) peak decreases as the yttrium concentration is increased up to 0.08 mM. The $(10\bar{1}\ 0)$ peak is dominant for solutions with more than 0.1 mM of yttrium concentration. Although yttrium doping does not alter the crystal structure, it causes the lattice constant change, causing the (0002) peak position to shift from 34.40 degrees for undoped ZnO to 33.36 degrees for 0.08 mM yttrium doped ZnO. At the same time, the $(10\bar{1}\ 0)$ peak of the undoped ZnO at 31.74 degrees is gradually shifted to 31.68 degrees for 0.08 mM yttrium concentration.

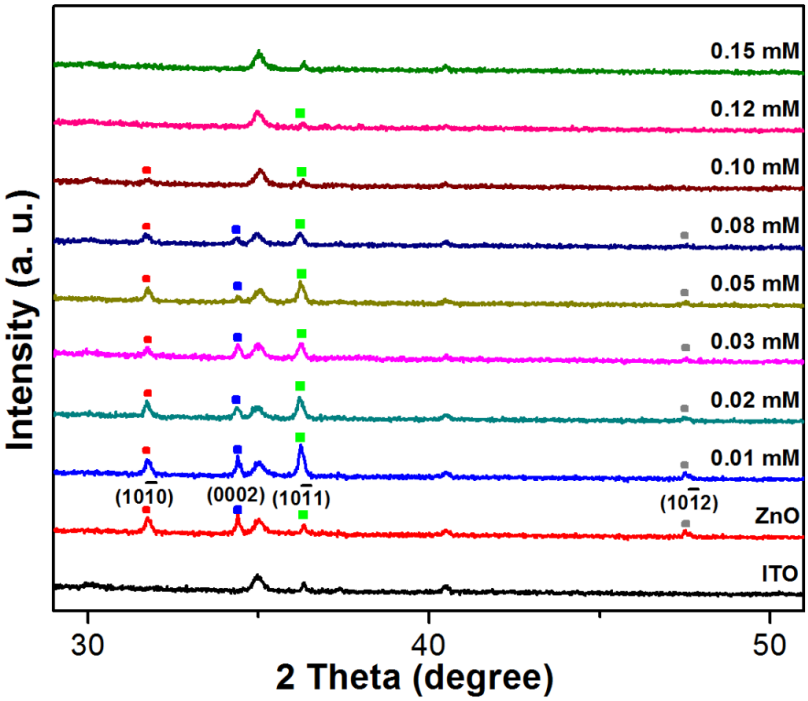

Figure 5-4. X-ray diffraction patterns of yttrium doped ZnO nanowires.

The increase of lattice constant suggests that the large yttrium ions substitute into the smaller Zn sites, partly, or into interstitial sites within the ZnO lattice. As shown in Figures 5-1 (f-i), nanowires are not grown along the vertical direction but along the horizontal direction, which behavior is induced by Y^{3+} ion suppressing nanowire growth on top of the (0002) face. Additionally, the top face of all of the nanowires show a quasi-hexagonal shape for more than 0.08 mM of yttrium content.[121-122] However, there are neither ZnO, zinc-related nor yttrium-related peaks in the EDS scan obtained from the 0.15 mM yttrium concentration sample. This is the case even though there are still short ZnO nanodots on the ITO surface as seen in

the FESEM image in Figure 5-1(i). The limited number of small ZnO nanocrystals is not detected by XRD, and so only ITO peaks are evident.

Photoluminescence (PL) is a useful technique for examination of the quality of ZnO nanowires, especially considering the presence of deep intrinsic defects. PL spectra obtained from annealed yttrium doped ZnO nanowires on seedless ITO, using a He-Cd laser with an exited wavelength of 325 nm, show the presence of a broad neutral donor-bound exciton emission peak at 381nm wavelength.[119] A continuous decrease is observed in the intensity of this exciton-emission peak, for nanowires grown from solutions with different yttrium molar concentrations, and the decrease correlates with the gradual reduction of the number of nanowires as shown in Figure 5-5.

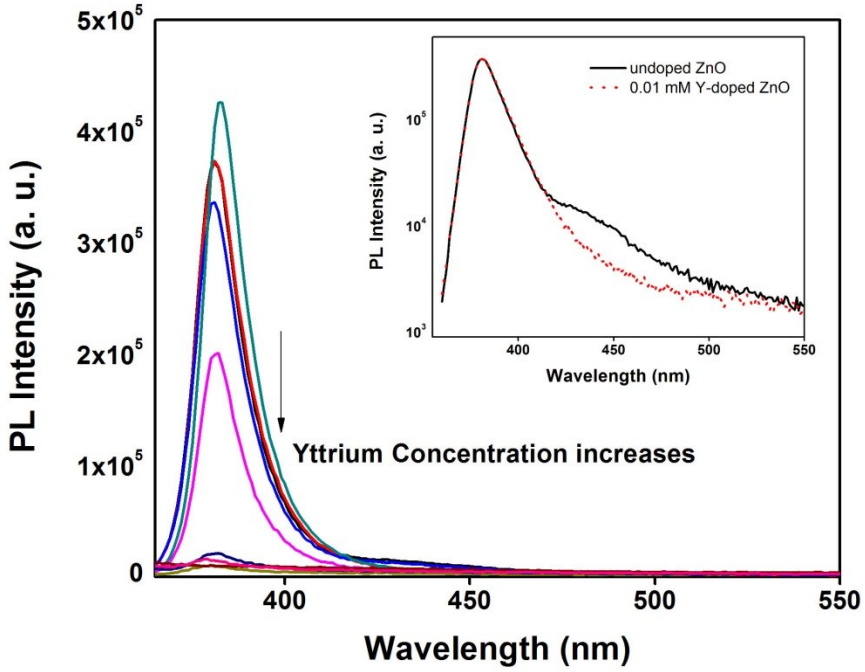

Figure 5-5. Photoluminescence spectra for yttrium doped ZnO nanowires with various yttrium concentrations.

Green band emission, resulting from radial recombination of a photo-generated hole with an electron that belongs to a singly ionized oxygen vacancy, was not detected after annealing at 400 °C in the air.[88] Interestingly, for 0.03 mM and 0.05 mM concentrations of yttrium in the solutions, PL peaks show a slight shift from 381 nm to 383 nm, corresponding to a bandgap change from 3.26 eV to 3.24 eV, respectively. One of the reasons for the UV emission shift might be the thermal energy caused by laser heating.[123] The inset in Figure 5-5 uses a logarithmic intensity scale for comparison of undoped ZnO and yttrium doped ZnO. Low yttrium contents (0.01 mM to 0.05 mM) show the same PL trend as the inset, for which a representative PL spectrum of 0.01 mM yttrium concentration has been chosen. The spectra reveal that neutral donor-bound exciton recombination processes dominate the emission in this work. Emission from free excitons, which would be located at a shoulder of the band edge emission, is not detected after annealing. Moreover, a broad peak region next to the neutral donor-bound exciton emission at higher wavelengths (lower energies) disappears in the 0.01 mM yttrium concentration PL spectrum. This is also known as a two-electron satellite (TES) related to a neutral donor excited from the 1s ground state to an excited state like 2s, 2p, *etc.*[124] Yttrium is a trivalent ion, with a $4d^1\ 5s^2$ electron configuration. Based on PL results, it appears that electrons of yttrium in the ZnO nanowires do not interact with oxygen vacancies, due to an absence of any observable green band emission. However, it is necessary to perform further research to understand the mechanism of yttrium doping into the ZnO crystals.

The transmittance and absorption of ZnO nanowires vertically aligned on ITO in the range of 350 to u700nm of wavelength are displayed in Figure 5-6. As indicated above, yttrium doping concentration from 0 to 0.05 mM, ZnO nanowires show slight decrease of absorption in the range from 350 to 400 nm owing to decrease of nanowires density. The absorption spectrum of 0.08 mM yttrium doped ZnO sample explains that combination of ZnO and ITO absorption behaviors which is attributed to decreased ZnO nanowires length. When the yttrium concentration exceeds 0.1 mM in the solution, nanowires growth was hindered by yttrium ions so that absorption spectra represent only ITO on glass substrate that is consistent with photoluminescence spectra.

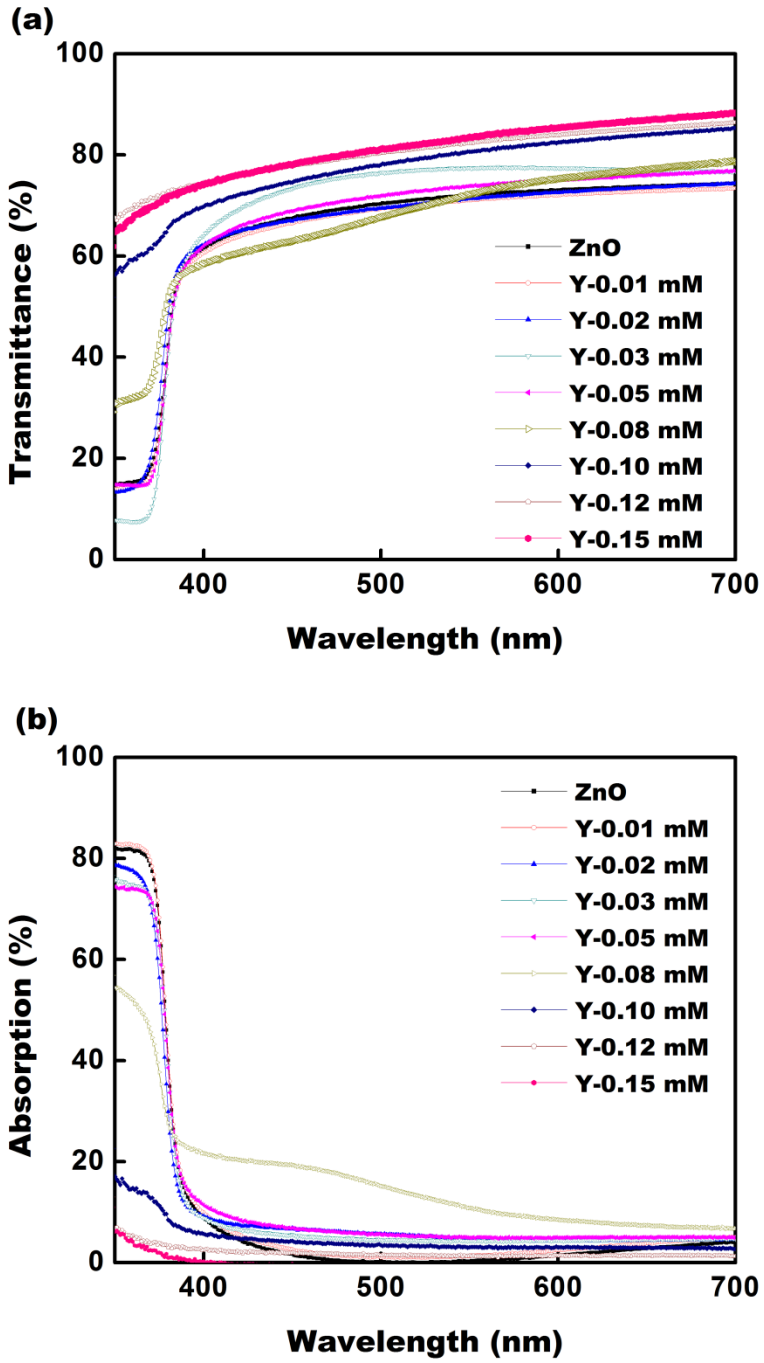

Figure 5-6. (a) Transmittance and (b) absorption spectra of Yttrium doped ZnO nanowires.

In conclusion, yttrium doped ZnO nanowires have been prepared on seedless ITO substrates, by electrochemically adding YCl_3 into $ZnCl_2$ aqueous solution at temperatures as low as 80 °C. Yttrium ions in the solution change the morphology and aspect ratios of the resulting 1-dimensional ZnO nanostructure as a result of positively charged yttrium ions attaching to the top of the ZnO growth front. This behavior also influences the number of sites for nucleation of ZnO nanowires, as yttrium ions move to the interface between the solution and ITO surface reducing accessibility for surface nucleation of ZnO nanowires. Further systematic study of yttrium doped ZnO nanostructures may enable density control without a seed layer, patterning of the nanowires onto a substrate, and aspect ratio control for nanostructured device applications. The enhanced UV emission capability of these nanostructures, without any significant broadening green band emission, as we confirm by PL spectra obtained at room temperature, can be quite useful for optoelectronic applications. The knowledge obtained in our study will contribute to the development of density and morphology control of ZnO nanocrystals enhanced by addition of a novel doping element, yttrium, in a manner which allows simple preparation, mass production and low cost fabrication.

5-3. Preparation of yttrium doped ZnO nanomaterials for organic bulk heterojunction solar cells

The solar cells performance having yttrium dope ZnO resulting in various areal densities on ITO substrates has been investigated. All devices

in this chapter have been prepared on 20 Ωsq^{-1} ITO coated glass substrates. These ITO substrates were cleaned in ultrasonic bath of acetone, methanol, and isopropanol followed by ultraviolet ozone (UVO) treatment. The growth of yttrium doped ZnO nanorod arrays was prepared by electrochemical deposition method using CHI 610B potentiostat in 0.5 mM $ZnCl_2$ aqueous solution at 80℃. A silver/silver chloride (Ag/AgCl) electrode and a platinum wire were used as the reference and counter electrodes, respectively. After both of undoped ZnO and yttrium doped ZnO nanostructure preparation at constant voltage of -1V, a conductive poly (3,4-ethylenedioxythiophene) poly (styrene sulfonate) (PEDOT:PSS) was used as a hole transport layer. The PEDOT:PSS layer was spin-coated at 5000 rpm for 1 min, resulting in a layer thickness of 30 nm after baking at 150 °C for 15 min. The photoactive layer of P3HT:PCBM blends were dissolved in 1, 2-dichlorobenzene with a mixing ratio of 1:1 by weight. The photoactive layers were obtained by spin-coating of the blend at 600 rpm for 1 min, which corresponded to a thickness of 250 nm. The metal cathode (LiF/Al) was thermally evaporated in a vacuum chamber through a shadow mask at a pressure of 1×10^{-7} Torr to finalize an active area of 0.2 cm^2

5-4. Characterization of yttrium doped ZnO nanostructured solar cells

Current density-voltage (J-V) characteristics were measured by simulated AM 1.5 global solar irradiation (100 mW/cm^2) using a xenon-lamp based solar simulator (Spectra Physics Oriel). The light source was calibrated with a standard Si photodiode reference cell (Hamamatsu) prior to

measurement. External quantum efficiencies (EQEs) were analyzed by a quantum efficiency measurement system (QE) and UV-VIS transmittance-reflectance spectra were obtained in the air (Cary 5000 spectrophotometer). The morphology of as-deposited yttrium doped ZnO nanostructure was characterized with the use of a field emission scanning electron microscope (FESEM, XL-30).

There are obvious differences in morphologies of ZnO nanorod arrays depending on the yttrium concentration as shown in Figure5-1. Without yttrium addition, only zinc ions in the solution are attracted to ITO substrate forming ZnO nanorods. Otherwise, yttrium ions play a key role in formation of ZnO nuclei as the ions are inhibiting the nucleation process. Therefore, number of nanorods density is reduced by addition of yttrium chloride into the solution.

5-5. Devices performance of yttrium doped ZnO nanostructured solar cells

Figure 5-7 shows the current density-voltage (J-V) characteristics of the ZnO nanostructured organic bulk-heterojunction solar cells having structures ITO/(ZnO or yttrium doped ZnO)/PEDOT:PSS/P3HT:PCBM/LiF/Al with and without ZnO nanorod arrays and various yttrium concentration during the nanorod arrays growth under AM 1.5 global solar irradiation with an intensity of 100 mW/cm^2. The short-circuit current density (J_{sc}), open-circuit voltage (V_{oc}), fill factor (FF), and power conversion efficiency (PCE) derived from the J-V curves for nanostructured organic solar cells are summarized in TableV.

Table V. Properties of yttrium doped ZnO nanostructured solar cells.

	V_{oc} (V)	J_{sc} (mA/cm^2)	FF (%)	R_{sh} (Ω cm^2)	R_s (Ω cm^2)	Eff. (%)
ITO	0.58	8.9	38	335	9.6	2.0
ZnO	0.51	9.5	30	150	10.3	1.5
Y-0.03 mM ZnO	0.54	9.2	44	372	10.5	2.2
Y-0.05 mM ZnO	0.54	9.2	40	251	10.2	2.0
Y-0.10 mM ZnO	0.52	9.0	37	264	12	1.8

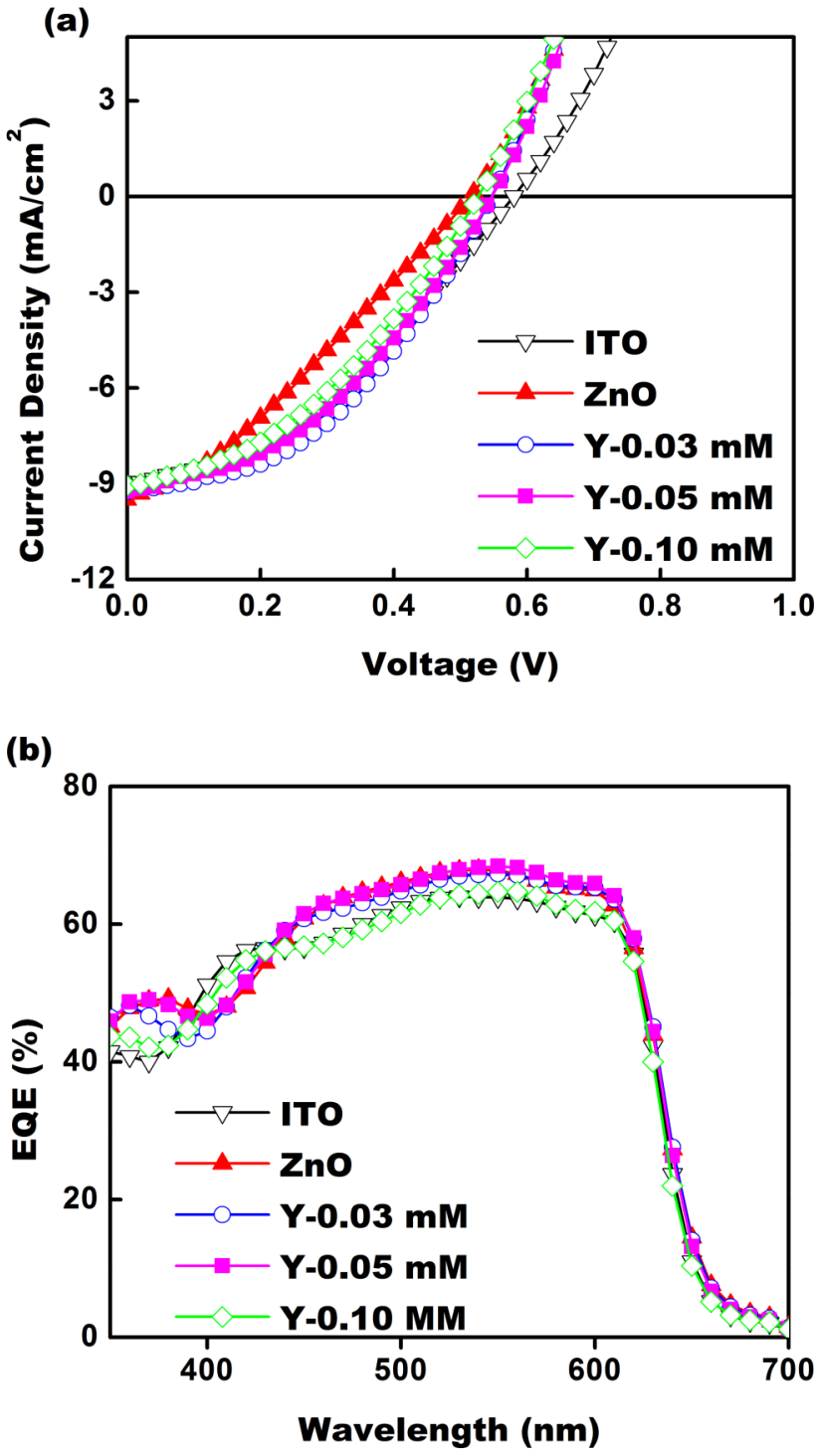

Figure 5-7. (a) Current density-voltage (J-V) characteristics and (b) external quantum efficiency for various yttrium concentrations of ZnO nanostructured organic solar cells.

Figure 5-8 shows the transmittance and reflectance spectra of ZnO nanostructured organic bulk heterojunction solar cells on seedless ITO substrates. The transmittances are similar to among them but as yttrium concentration increases, the transmittances of ZnO and yttrium doped ZnO nanostructure have better transmittances than bare ITO substrates in the wavelength range lower than 450 nm.

Importantly, the reflectance spectra show clear evidence for improving EQEs of ZnO and yttrium doped ZnO nanostructured solar cells. As yttrium doping concentration increases, the reflectances have been increased due to the light reflection from partially covered ITO substrate. As shown in FESEM images, the areal density of ZnO nanorod arrays is inversely related to yttrium concentration. The number of nucleation site has decreased 90, 30, 20, and 10 sites as yttrium concentration increases 0, 0.03, 0.05, and 0.10 mM, respectively. This result indicates that the controlled-number density of ZnO nanorods on ITO is able to change the light reflection on the substrate.

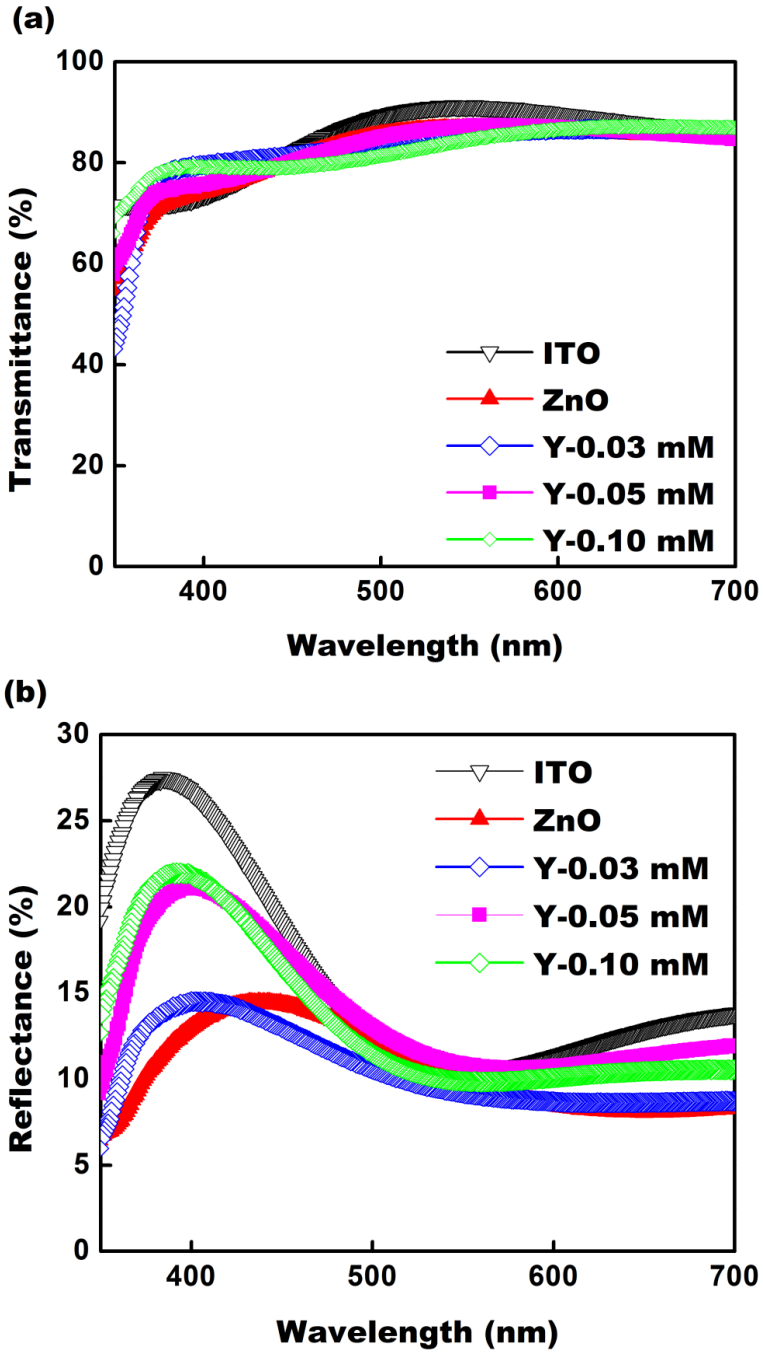

Figure 5-8. (a) Transmittance and (b) reflectance spectra of yttrium doped ZnO nanostructures on seedless ITO.

5-6. Summary

In conclusion, yttrium doped ZnO nanowires prepared on seedless ITO substrate have been used for nanostructured organic bulk heterojunction solar cells. Yttrium ions in the solution changed the morphology and areal density of ZnO nanowires resulting in controllable growth condition of nanostructure for solar cells. Without patterning with a mask, the decrease of number density of ZnO nanowires on ITO decrease the reflection of the light on the substrate more than 50% resulting in better EQEs than solar cells without ZnO nanowires. However, the reason for having 10% increase of PCE with yttrium doped ZnO nanowires is due to the fact that the lengths of ZnO, with or without yttrium doping, are more than 500 nm for all cases which causes the reduction of the V_{oc} from 0.58 V to 0.51 V. On the other hand, the organic solar cells having yttrium doped ZnO nanostructure shows increase of J_{sc} from 8.9 to 9.5 mA/cm^2 resulting in 10% better performance of nanostructured than flat bulk heterojunction solar cells.

ZnO nanowire growth on seedless ITO using yttrium dopant allows simple and low cost fabrication for organic bulk heterojunction solar cells by easily controllable the areal density of nanowires without patterning.

Chapter 6

FLEXIBLE ORGANIC BULK-HETEROJUNCTION SOLAR CELLS

6-1. Introduction to flexible organic bulk heterojunction solar cells

The widespread need to develop cost effective renewable energy sources originated for efficient, low cost photovoltaic devices. The organic, polymer-based photovoltaic devices have been introduced the potential of obtaining cheap and easy methods to produce energy from light. The possibility of chemically manipulating the material properties of polymers combined with a variety of cheap processing techniques has made polymer-based materials present in almost every aspect of modern research topics. Organic devices have several advantages such as low cost synthesis and easy fabrication of thin film devices by vacuum evaporation/sublimation, solution cast, ink-jet printing, and roll-to-roll methods.[125] In addition, to achieve wearable and bendable photovoltaic devices, it is critical to adapt a flexible substrate instead of glass which is a common substrate both for organic and inorganic photovoltaic devices.

Organic photovoltaic (OPV) devices have obtained much attention due to their promising properties such as mechanical flexibility, light weight and low production cost. In last decades, the power conversion efficiency (PCE) of organic solar cells has been improved and exceeded 5% by developing a new nanostructures, active materials and process enhancements. So far, the most widely used bottom transparent electrode is ITO deposited by reactive sputtering on either glass or flexible polymer foils such as Polyethylene

terephthalate (PET) and polyethylene naphtalate (PEN). In order to compensate the roughness of flexible substrate, a conductive poly (3,4-ethylenedioxythiophene) poly (styrene sulfonate) (PEDOT:PSS) was widely applied as a hole transport layer on ITO. The advantage of plastic solar cells compared to inorganic ones stems from the possibility of producing large area flexible devices with easy processing techniques.[126-127]

6-2. Fabrication of flexible organic bulk heterojunction solar cells

The enhanced performance of the flexible organic photovoltaics based on the blend of poly(3-hexylthiophene) (P3HT) and (6,6)-phenyl C_{61} butyric acid methyl ester (PCBM) on transparent poly(ethylene naphtalate) (PEN) substrates coated with indium tin oxide (ITO) have been demonstrated in this chapter.

Organic photovoltaic devices in this study were prepared on 100 Ω sq^{-1} and 20 Ω sq^{-1} ITO coated PEN and glass, respectively. These substrates were cleaned in ultrasonic bath of acetone, methanol, and isopropanol. Unlike ITO coated glass substrates, PEN substrates have silicon nitride (SiN) buffer layer between PEN and ITO layers to moderate the roughness and water absorption. A 500 nm SiN layer was prepared by chemical vapor deposition (CVD) at 150 °C. A PEDOT:PSS layer was used as a hole transport layer. The PEDOT:PSS layer was spin-coated at 5000 rpm for 1 min, resulting in a layer thickness of 30 nm after baking at 150 °C for 15 min. The photoactive layer of P3HT:PCBM blends were dissolved in 1, 2-dichlorobenzene with a mixing ratio of 1:1 by weight. The photoactive layers were obtained by spin-coating of

the blend at 600 rpm for 1 min, which corresponded to a thickness of 250 nm. The metal cathode (BCP/Ag) was thermally evaporated in a vacuum chamber through a shadow mask at a pressure of 1×10^{-7} Torr to finalize an active area of 0.2 cm^2.

6-3. Characterization of flexible organic bulk heterojunction solar cell

Current density-voltage (J-V) measurements were done using simulated AM 1.5 global solar irradiation (100 mW/cm^2) using a xenon-lamp based solar simulator (Spectra Physics Oriel). The light source was calibrated with a standard Si photodiode reference cell (Hamamatsu) prior to measurement. External quantum efficiencies (EQEs) were analyzed by a quantum efficiency measurement system (QE) and UV-VIS transmittance-reflectance spectra were obtained in the air (Cary 5000 spectrophotometer).

6-4. Devices performance of flexible organic bulk heterojunction solar cells

Figure 6-1 displays the current density-voltage (J-V) characteristics of the PEN-supported bulk heterojunction solar cells having structures PEN/SiN/ITO/PEDOT:PSS/P3HT:PCBM/BCP/Ag compared with the glass substrate device under AM 1.5 global solar irradiation with an intensity of 100 mW/cm^2. The short-circuit current density (J_{sc}), open-circuit voltage (V_{oc}), fill factor (FF), and power conversion efficiency (PCE) derived from the J-V curves for organic solar cells are summarized in Table VI.

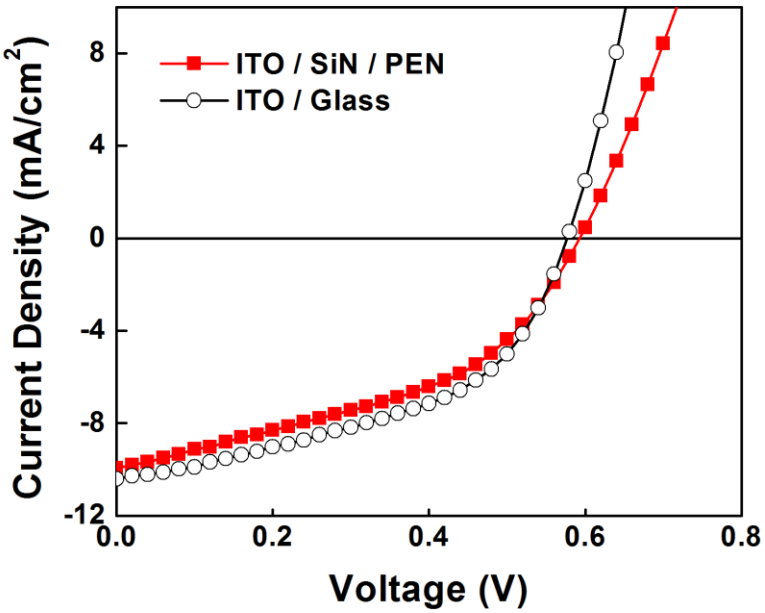

Figure 6-1. Comparison of current density-voltage (J-V) characteristics for organic solar cells with glass substrate and PEN substrate.

Table VI. The summary of device parameters of the flexible organic bulk heterojunction solar cell

	V_{oc} (V)	J_{sc} (mA/cm^2)	FF (%)	R_{sh} (Ω cm^2)	R_s (Ω cm^2)	Eff. (%)
ITO / Glass	0.57	10.4	48	192	3.5	2.9
ITO / SiN / PEN	0.58	9.9	43	138	8.4	2.5

The device fabricated on PEN substrate shows a V_{oc} of 0.58 V, a J_{sc} of 9.9 mA/cm^2, a FF of 43% that resulting in a PCE of 2.5%, while the PCE of glass substrate device shows 2.9%. It is obvious that lower PCE of flexible solar cell than glass counterpart is due to the absorption of light in PEN itself in the range of 350~400 nm as shown in Figure 6-2.

The transmittance/absorption data in Figure 6-2 explains one of the reasons that flexible solar cell has lower power conversion efficiencies than glass solar cell. The incoming light below 400 nm of wavelength is absorbed by PEN so that transmittance abruptly decreases resulting in less generation of current in those wavelengths range.

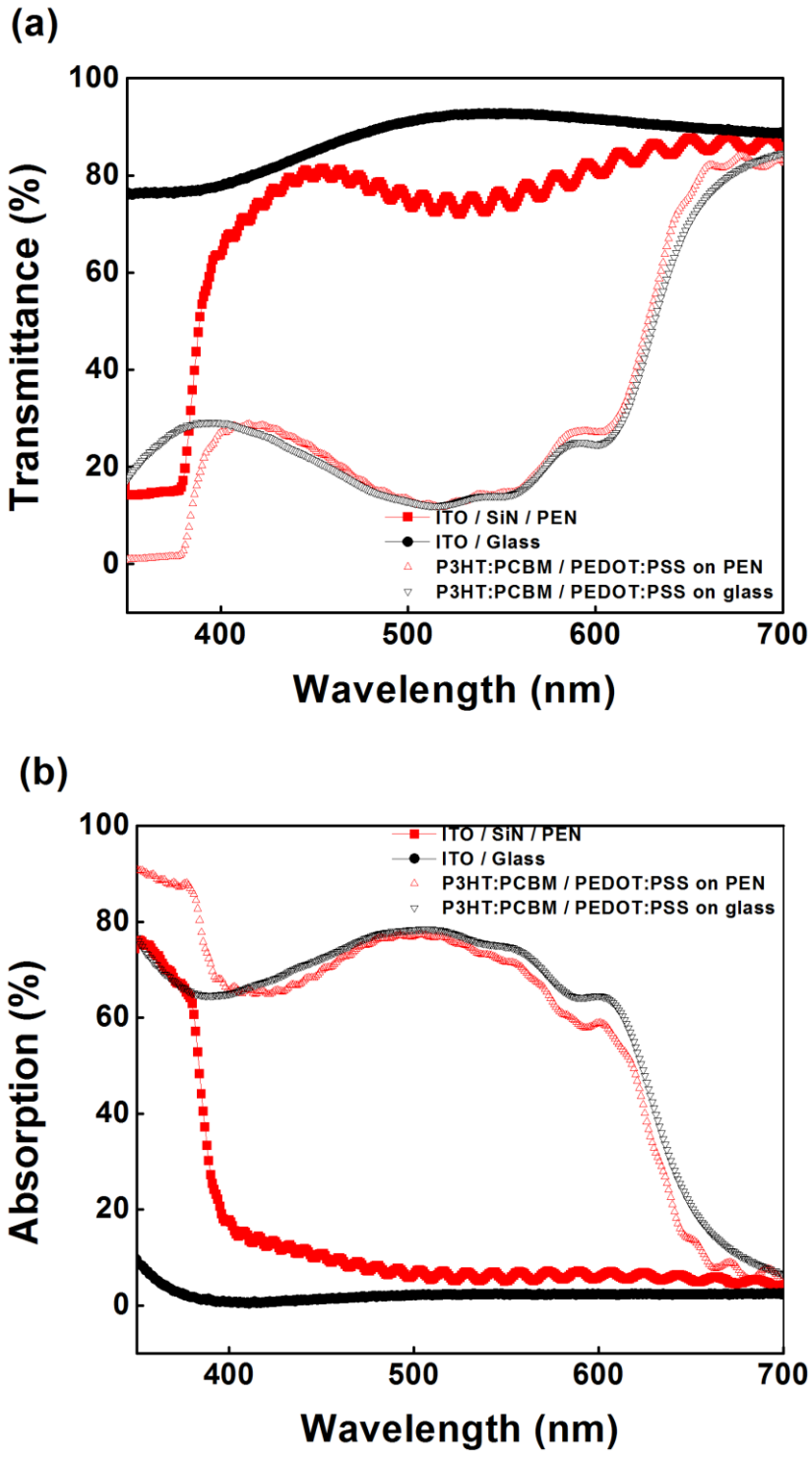

Figure 6-2. (a) Transmittance and (b) absorption spectra of organic bulk-heterojunction solar cells on PEN and glass substrates.

In addition, it is interesting that the transmittances for both of PEN and glass devices show very similar trend in the wavelength range of 400~700 nm after serial deposition of PEDOT:PSS and P3HT:PCBM even though substrates have more than 10% variation of their native transmittances. The active layer of P3HT:PCBM is minimally limited by transmission of light on bare substrates resulting in less transmittance/absorption difference between them after the active layer deposition.

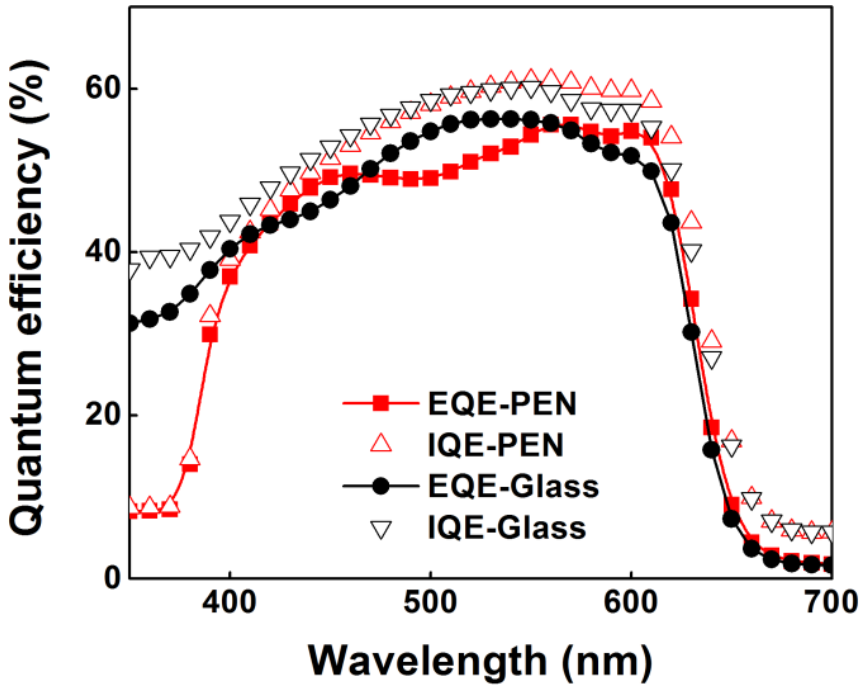

Figure 6-3. External quantum efficiencies (EQEs) and internal quantum efficiencies (IQEs) of flexible PEN-solar cell and rigid glass-solar cell.

Related with optical properties of the devices, the quantum efficiencies shown in Figure 6-3 have been obtained under AM 1.5 global solar irradiation (100 mW/cm^2). Wavelength range from 420 to 680 nm shows same trend for

both PEN and glass substrate devices. However, exciton generation is hindered by less photons passing through PEN towards active layer of P3HT:PCBM. It is prominent that absorption of light is a direct reason for dramatically reduction of exciton formation in active layer.

6-4. Summary

In conclusion, we have successfully fabricated bulk-heterojunction solar cells on ITO coated PEN with silicon nitride buffer layer. In order to obtain better power conversion efficiency, it is critical to reduce the absorption of incident light at PEN substrate. Even though, the light absorption below the wavelength of 400 nm is a native property of PEN substrates, we can conclude that the power conversion efficiency of our solar cell on PEN with efficiency of 2.5% is still very promising for inexpensive, low temperature, and large area flexible photovoltaic applications.

Chapter 7

SUMMARY AND CONCLUSION

In this dissertation, 1-dimensional ZnO nanomaterials for the application of hybrid/nanostructured solar cells were investigated by adapting simple electrochemical deposition method in order to understand the device physics of bulk heterojunction solar cells based on P3HT:PCBM active material.

Initial findings show that when the concentration of KCl is less than 1 M, Cl^- ions hinder diameter growth, favoring longitudinal growth; whereas when the concentration is larger than 1 M, diameter growth is favored. Nanowires elongated their diameter and as KCl concentration increases to 3 M that no vertical wires growth occurred. At this point nanodots were formed. The growth of ZnO nanowire should be kept in the range of less than 1 M of KCl concentration to ensure nanowire structures instead of plate or film formation.

ZnO nanowires on TEM grid in $ZnCl_2$ and KCl aqueous solution within 10 minutes were successfully grown on seedless ITO substrate. The morphology of the ZnO nanowires was influenced by the substrate species and was investigated by high resolution TEM and SAED analyses. Electrochemically deposited ZnO nanowires have a hexagonal wurtzite crystal structure and have a 0.26 nm *d*-spacing of the ZnO (0002) plane. ZnO nanowires can be grown on carbon-based materials which supply enough nucleation sites when they form nanodots or nanowires. This aspect is independent on their crystal structures. By depositing ZnO nanomaterials

directly on to TEM grid, the investigation for dependence of ZnO nanomaterials on solution types can be easily conducted without damaging samples.

A seed layer of gold plays a critical role in directional growth when ZnO nucleus was formed at the interface of gold and the solution. ZnO nanowires on thicker seed layer have larger diameter which has larger grain size of gold layer that directly influences the diameter of ZnO nanowires. Perfectly vertical ZnO nanowire can be grown on a gold seed layer that acts as both a seed layer and an electrode.

The knowledge obtained by demonstrating the growth of ZnO nanomaterials, nanostructured organic solar cells based on an electrochemically deposited ZnO antireflection layer with improved efficiency and good growth stability was simply fabricated on seedless ITO glass substrate. It is found that it is critical to control absorption of photons through P3HT:PCBM layer at lower wavelength up to 500 nm in order to obtain the bulk-heterojunction photovoltaic devices, resulting in better power conversion efficiency. The electrochemical deposition of ZnO nanorods is a very promising technique and further contributes to improve the device performance for the large area, low temperature, and cost effective photovoltaic devices.

Yttrium doped ZnO nanowires were prepared on seedless ITO substrates by electrochemically adding YCl_3 into a $ZnCl_2$ aqueous solution at temperatures as low as 80 °C. Yttrium ions in the solution change the morphology and aspect ratios of the resulting 1-dimensional ZnO

nanostructure as a result of positively charged yttrium ions attaching to the top of the ZnO growth front. This behavior also influences the number of sites for nucleation of ZnO nanowires, as yttrium ions move to the interface between the solution and ITO surface reducing accessibility for surface nucleation of ZnO nanowires. The enhanced UV emission capability of these nanostructures, without any significant broadening green band emission, as confirmed by PL spectra obtained at room temperature, can be quite useful for optoelectronic applications. The knowledge obtained in our study will contribute to the development of density and morphology control of ZnO nanocrystals enhanced by addition of a novel doping element, yttrium, in a manner which allows simple preparation, mass production and low cost fabrication.

In addition, yttrium doped ZnO nanowires prepared on seedless ITO substrate were used for nanostructured organic bulk heterojunction solar cells. Without patterning with a mask, the reduction of number density of ZnO nanowires on ITO decrease the reflection of the light on the substrate more than 50% resulting in better EQEs than solar cells without ZnO nanowires. The organic solar cells having yttrium doped ZnO nanostructure shows increase of J_{sc} from 8.9 to 9.5 mA/cm^2 resulting in 10% better performance of nanostructured than flat bulk heterojunction solar cells. ZnO nanowires growth on seedless ITO using yttrium dopant allows simple and low cost fabrication for organic bulk heterojunction solar cells by easily controllable the areal density of nanowires without patterning.

A flexible bulk-heterojunction solar cells on ITO coated PEN with silicon nitride buffer layer were successfully fabricated. In order to obtain better power conversion efficiency, it is critical to reduce the absorption of incident light at PEN substrate. Even though, the light absorption below the wavelength of 400 nm is a native characteristic of PEN substrates, the power conversion efficiency of flexible solar cell on PEN with efficiency of 2.5% is still very promising for inexpensive, low temperature, and large area flexible photovoltaic applications.

REFERENCES

(1) D. C. Look, Mater. Sci. Eng., B, 80, 383 (2001)

(2) S. J. Pearton, D. P. Norton, K. Ip, Y. W. Heo, and T. Steiner, Superlattices and Microstruct. 34, 3 (2003)

(3) Y. Chen, D. M. Bagnall, H. J. Koh, K. T. Park, K. Hiraga, Z. Q. Zhu, and T. Yao, J. Appl. Phys. 84, 3912 (1998).

(4) S. B. Zhang, S. H. Wei, and A. Zunger , Phys. Rev. B, 63, 075205 (2001)

(5) D. C. Look, C. Coskun, B. Claflin and G. C. Farlow, Physica, B, 340 (2003)

(6) R. L. Hoffman, B. J. Norris, and J. F. Wager, Appl. Phys. Lett. 82, 5 (2003)

(7) T. Minami, Semicond. Sci. Technol. 20, 35 (2005)

(8) A. Tsukazaki, A. Ohtomo, T. Onuma, M. Ohtani, T. Makino, M. Sumiya, K. Ohtani, S. F. Chichibu, S. Fuke, Y. Segawa, H. Ohno, H. Koinuma, and M. Kawasaki, Nat. Mater. 4, 42 (2005)

(9) S. D. Oosterhout, M. M.Wienk, S. S. van Bavel, R. Thiedmann, L. J. A. Koster, J. Gilot, J. Loos, V. Schmidt, and R. A. J. Janssen, Nat. Mater. 8,818 (2009)

(10) U. Ozgeur, Y. I. Alivov, C. Liu, A. Teke, M. A. Reshchikov, S. Dogan,V. Avrutin, S. J. Cho, and H. Morkoc, J. Appl. Phys. 98, 041301 (2005)

(11) K. Ueda, H. Tabata, and T. Kawai, Appl. Phys. Lett. 79, 988 (2001)

(12) Z. Jin, T. Fukumura, M. Kawasaki, K. Ando, H. Saito, T. Sekiguchi, Y. Z. Yoo, M. Murakami, Y. Matsumoto, T. Hasegawa, and H. Koinuma , Appl. Phys. Lett. 78, 3824 (2001)

(13) J. R. Neal, A. J. Behan, R. M. Ibrahim, H. J. Blythe, M. Ziese, A. M. Fox, and G. A. Gehring, Phys. Rev. Lett. 96, 197208 (2006)

(14) C. Gu, C. Cheng, H. Huang, T. Wong, N. Wang, and T. Y. Zhan, Cryst. Growth Des. 9, 3278 (2009)

(15) C. Cheng, M. Lei, L. Feng, T. L. Wong, K. M. Ho, K. K. Fung, M. M. T. Loy, D. Yu, and N. Wang, ACS Nano, 3, 53 (2009)

(16) B. A. Smith, C. Crystal Structure, Connexions Web site. http://cnx.org/content/m16927/1.10 (2010)

(17) W. I. Park, D. H. Kim, S. W. Jung, and G. C. Yi, Appl. Phys. Lett. 80, 4232 (2002)

(18) D. Jena, S. P. Alpay, and J. V. Mantese, J. Mater. Sci.: Mater. Electron. 10, 227 (1999)

(19) J. Muster, G. T. Kim, V. Krstic, J. G. Park, Y. W. Park, S. Roth, and M. Burghard, Adv. Mater. 12, 420 (2000)

(20) N. J. Stone and H. Ahmed, Appl. Phys. Lett. 73, 2134 (1998)

(21) Y. Cui, Q. Wei, H. Park, and C. M. Lieber, Science, 293, 1289 (2001)

(22) M. H. Huang, S. Mao, H. Feick, H. Yan, Y. Wu, H. Kind, E. Weber, R. Russo, and P. Yang, Science, 292, 1897 (2001)

(23) R.S. Wagner and W. C. Ellis, Appl. Phys. Lett. 4, 889 (1964)

(24) X. Duan and C. M. Lieber, Adv. Mater. 12, 298 (2000)

(25) J. Pfeifer, E. Badaljan, P. Tekula-Buxbaum, T. Kovacs, 0. Geszti, A. L. Toth, and H. J. Lunk, J. Crys. Growth. 169, 727 (1996)

(26) J. Gavillet, A. Loiseau, F. Ducastelle, S. Thair, P. Bernier, O. stephan, J. Thibault, and J. C. Charlier, Carbon, 40, 1649 (2002)

(27) Rudolf Holze, WILEY-VCH Verlag GmbH & Co. Chap 1 (2009)

(28) J. Xu, Q. Pan, Y. Shun, and Z. Tian, Sens. Actuators, B, 277 (2000)

(29) F. Zhang, X. Wang, S. Ai, Z. Sun, Q. Wan, Z. Zhu, Y. Xian, L. Jin, and K. Yamamoto, Anal. Chim. Acta, 519, 155 (2004)

(30) S. K. Kim and J. Y. Son, Electrochem. Solid-State Lett. 12, J17 (2009)

(31) X. Chu, D. Jiang, B. D. Aleksandra, and H. L. Yu, Chem. Phys. Lett. 401, 426 (2005)

(32) Y. W. Jun, J. S. Choi, and J. Cheon, Angew. Chem. Int. Ed. 45,

3414 (2006)

(33) C. Pacholski, A. Kornowski, and H. Weller, Angew. Chem. Int. Ed. 41, 1188 (2006)

(34) P. X. Gao and Z. L. Wang, J. Phys. Chem. B, 108, 7534 (2004)

(35) D. Ramirez, T. Pauporte, H. Gomez, and D. Lincot, Phys. Stat. Sol. A, 205, 2371 (2008)

(36) L. S. Mende and J. L. MacManus-Driscoll, Mater. Today, 10, 40 (2007)

(37) L. Vayssieres, Adv. Mater. 15, 464 (2003)

(38) Y. Sun, D. J. Riley, and M. N. R. Ashfold, J. Phys. Chem. B, 110, 15186 (2006)

(39) L. E. Greene, M. Law, D. H. Tan, M. Montano, and J. Goldberger, Nano Lett. 5, 1231 (2005)

(40) Z. R. Tian, J. A. Voigt, , J. Liu, B. Mckenzie, M. J. Mcdermott, M. A. Rodriguez, H. Konishi, and H. Xu, Nat. Mater. 2, 821 (2003)

(41) Z. Chen and L. Gao, J. .Crys. Growth, 293, 522 (2006)

(42) D. S. Boyle, K. Govender, and P. O'Brien, Chem. Commun. 1, 80 (2002)

(43) Z. Wang, X. F. Qian, J. Yin, and Z. K. Zhu, Langmuir, 20, 3441 (2004)

(44) H. Zhang, D. Yang, S. Li, X. Ma, Y. Ji, J. Xu, and D. Que, Mater. Lett., 59, 1696 (2005)

(45) K. Govender, D. S. Boyle, P. B. Kenway, and P. O'Brien, J. Mater. Chem., 14, 2575 (2004)

(46) J. Nelson, World Scientific, 1, 10 (2003)

(47) B. A. Gregg and M. C. Hanna, J. Appl. Phys. 93, 3605 (2003)

(48) B. A. Gregg, J. Phys. Chem. B, 107, 4688 (2003)

(49) H. Hoppe and N. S. Sariciftci, J. Mater. Res. 19, 1924 (2004)

(50) M. A. Green, K. Emery, Y. Hishikawa, W. Warta, and E. D. Dunlop, Prog. Photovolt.: Res. Appl. 20, 12 (2012)

(51) N. Geacintov, M. Pope, and H. Kallmann, J. Chem. Phys. 45, 2639 (1966)

(52) A. K. Ghosh and T. Feng, J. Appl. Phys. 49, 5982 (1978)

(53) D. L. Morel, A. K. Ghosh, T. Feng, E. L. Stogryn, P. E. Purwin, R. F. Shaw, and C. Fishman, Appl. Phys. Lett. 32, 495 (1978)

(54) Y. Nagao, Y, K. Tsuda, K. Kozawa, and T. Uchida, Heterocycles 54, 757 (2001)

(55) R. Gomez, J. L. Segura, and N. Martin, Org. Lett. 7, 717 (2005)

(56) G. Yu and A. J. Heeger , J. Appl. Phys. 78, 4510 (1995)

(57) S. Shaheen, C. Brabec, and N. S. Sariciftci, Appl. Phys. Lett. 78, 841 (2001).

(58) J. Xue, S. Uchida, B. Rand, and S. Forrest, Appl. Phys. Lett. 84, 3013 (2004)

(59) M. Jorgensen and F. Krebs, J. Org. Chem. 69, 6688 (2004)

(60) A. M. Ramos, M. T. Rispens, J. K. J. van Duren, J. C. Hummelen, and R. A. J. Janssen, J. Am. Chem. Soc. 123, 6714 (2001)

(61) D. Beljonne, J. Am. Chem. Soc. 125, 8625 (2003)

(62) R. A. J. Janssen, J. Am. Chem. Soc. 126, 10611 (2004)

(63) E. W. Meijer, J. Am. Chem. Soc. 126, 10021 (2004)

(64) E. W. Meijer, J. Am. Chem. Soc. 127, 11763 (2005)

(65) J. Xue, S. Uchida, B. P. Rand, and S. Forrest, Appl. Phys. Lett. 85, 5757 (2004)

(66) W. Shockley and H. J. Queisser, J. Appl. Phys. 32, 510 (1961)

(67) S. Gunes, H. Neugebauer, and N. S. Sariciftci, Chem. Rev. 1, 107 (2007)

(68) I. D. Parker, J. Appl. Phys., 75, 1656 (1994)

(69) C. J. Brabec, A. Cravino, D. Meissner, N. S. Sariciftci, T. Fromherz, M. T. Rispens, L. Sanchez, and J. C. Hummelen, Adv. Funct. Mater. 11 (2001)

(70) D. Mühlbacher, M. Scharber, M. Morana, Z. Zhu, D. Waller, R. Gaudiana, and C. Brabec, Adv. Mater. 18, 2884 (2006)

(71) J.K.J. van Duren, J. Loos, F. Morrissey, C.M. Leewis, K.P.H. Kivits, L.J. van IJzendoorn, M.T. Rispens, J.C. Hummelen, and R.A.J. Janssen, Adv. Func. Mater. 12, 665 (2002)

(72) C.W.T. Bulle-Lieuwma, W.J.H. Van Genni, J.K.J. Van Duren, P. Jonkheijm, R.A.J. Janssen, and J.W. Niemantsverdriet, Appl. Surf. Sci., 203, 547 (2003)

(73) J. K. J. van Duren, X. Yang, J. Loos, C. W. T. Bulle-Lieuwma, A. B. Sieval, J. C. Hummelen, R. A. J. Janssen, Adv. Func. Mater. 14, 425 (2004)

(74) M. A. Loi, P. Denk, H. Hoppe, H. Neugebauer, C. Winder, D. Meissner, C. Brabec, N. S. Sariciftci, A. Gouloumis, P. Vazquez, and T. Torres, J. Mater. Chem. 13, 700 (2003)

(75) D. C. Olson, J. Piris, R. T. Collins, S. E. Shaheen, and D. S. Ginley, Thin Solid Films, 496, 26 (2006)

(76) R. Thitima, C. Patcharee, S. Takashi, and Y. Susumu, Solid-state Electron. 53, 176 (2009)

(77) K. S. Leschkies, R. Divakar, J. Basu, E. Enache-Pommer, J. E. Boercker, C. B. Carter, U. R. Kortshagen, D. J. Norris, and E. S. Aydil, Nano Lett., 7, 1793 (2007)

(78) Z. H. Chen, Y. B. Tang, C. P. Liu, Y. H. Leung, G. D. Yuan, L. M. Chen, Y. Q. Wang, I. Bello, J. A. Zapien, W. J. Zhang, C. S. Lee, and S. T. Lee, J. Phys. Chem. C, 113, 13433 (2009)

(79) N. O. V. Plank, H. J. Snaith, C. Ducati, J. S. Bendall, L. Schmidt-Mende, and M. E. Welland, Nanotechnology, 19, 465603 (2008)

(80) L. E. Greene, M. Law, B. D. Yuhas, and P. Yang, J. Phys. Chem. C, 111, 18451 (2007)

(81) Y. J. Lee, D. S. Ruby, D. W. Peters, B. B. McKenzie, and J. W. P. Hsu, Nano Lett. 8, 1501 (2008)

(82) C. Y. Jiang, X. W. Sun, K. W. Tan, G. Q. Lo, A. K. K. Kyaw, and D. L. Kwong, Appl. Phys. Lett. 92, 143101 (2008)

(83) D. A. Porter and K. E. Easterling, Taylor & Francis Group, Chap

5 (1992)

(84) D. A. Porter and K. E. Easterling, Taylor & Francis Group, Chap 4 (1992)

(85) J. A. Venebles, Cambridge university press, Chap 1 (2000)

(86) B. B. Li, U. Philipose, C. F. de Souza, and H. E. Ruda, J. Electrochem. Soc. 158, D282 (2011)

(87) Y. C. Kong, D. P. Yu, B. Zhang, W. Fang, and S. Q. Feng, Appl. Phys. Lett. 78, 407 (2001)

(88) K. Vanheusden, W. L. Warren, C. H. Seager, D. R. Tallant, J. A. Voigtand B. E. Gnade, J Appl. Phys., 79, 7983-7990 (1996)

(89) F. A. Kroger, The Chemistry of Imperfect Crystals, 2nd Ed. 73 (1974)

(90) L. Xu, Y. Guo, Q. Liao, J. Zhang, and D. Xu, J. Phys. Chem. B, 109, 13519 (2005)

(91) S. D. Oosterhout, M. M.Wienk, S. S. van Bavel, R. Thiedmann, L. J. A. Koster, J. Gilot, J. Loos, V. Schmidt, and R. A. J. Janssen, Nat. Mater. 8,818 (2009)

(92) X. Fang, Y. Bando, U. K. Gautam,T. Zhai, H. Zeng, X. Xu, M. Liao, and D. Goldberg, Crit. Rev. Solid State Mater. Sci. 34, 190 (2009)

(93) Z. L. Wang, Mater. Today, 7, 26 (2004)

(94) L. E. Greene, M. Law, D. H. Tan, M. Montano, and J. Goldberger, Nano Lett. 5, 1231 (2005)

(95) Z. R.Tian, J. A.Voigt, , J. Liu, B. Mckenzie, M. J. Mcdermott, M. A. Rodriguez, H. Konishi, and H. Xu, Nat. Mater. 2, 821 (2003)

(96) Z. Chen and L. Gao, J. .Crys. Growth, 293, 522 (2006)

(97) D. S. Boyle, K. Govender, and P. O'Brien, Chem. Commun., 1, 80 (2002)

(98) W. Wang, H. Wu, C. Yang, C. Luo, Y. Zhang, J. Chen, and Y. Cao, Appl. Phys. Lett. 90, 183512 (2007)

(99) Y. Kim, S. A. Choulis, J. Nelson, D. D. C. Bradley, S. Cook, and J. R. Durrant, Appl. Phys. Lett. 86, 063502 (2005)

(100) Z. Xu, L. M. Chen, G. Yang, C. H. Huang, J. Hou, Y. Wu, G. Li, C. S. Hsu, and Y. Yang, Adv. Func. Mater. 19, 1227 (2009)

(101) G. Yu, J. Gao, J. C. Hummelen, F. Wudl, and A. J. Heeger, Science, 270, 5243, 1789 (1995)

(102) C. Waldauf, M. Morana, P. Denk, P. Schilinsky, K. Coakley, S. A. Chouli and C. J. Brabec, Appl. Phys. Lett. 89, 233517 (2006)

(103) D. W. Zhao, S. T. Tan, L. Ke, P. Liu, A. K. K. Kyaw, X. W. Sun, G. Q. Lo, and D. L. Kwong, Sol. Energy Mater. Sol. Cells, 94, 985 (2010)

(104) S. K. Hau, H. L. Yip, N. S. Baek, J. Zou, K. O'Malley, and A. K. Y. Jen, Appl. Phys. Lett. 92, 353301 (2008)

(105) Y. Sun, X. Gong, B. B. Y. Hsu, H. L. Yip, A. K. Y Jen, and A. J. Heeger, Appl. Phys. Lett. 97, 193310 (2010)

(106) T. Shirakawa, T. Umeda, Y. Hashimoto, A. Fukii, and K. Yoshino, J. Phys. D: Appl. Phys. 37, 847 (2004)

(107) K. Takanezawa, K. Hirota, Q. S. Wei, K. Tajima, and K. Hashimoto, J. Phys. Chem. C, 111, 7219 (2007)

(108) A.E. Jimenez-Gonzalez, J. A. S. Urueta, and R. Suarez-Parra, J. Crys. Growth, 192, 430 (1998)

(109) V. Bhosle A. Tiwari, and J. Narayan, Appl. Phys. Lett. 88, 032106 (2006)

(110) K. Nakahara, H. Takasu, P. Fons, A. Yamada, K. Iwata, K. Matsubara, R. Hunger, and S. Niki, Appl. Phys. Lett. 79, 4139 (2001)

(111) J. F. Wager, Science, 300, 1245 (2003)

(112) D. M. Bagnall, Y. F. Chen, Z. Zhu, T. Yao, S. Koyama, M. Y. Shen, and T. Goto, Appl. Phys. Lett. 70, 2230 (1997)

(113) Y. C. Kong, D. P. Yu, B. Zhang, W. Fang, and S. Q. Feng, Appl. Phys. Lett. 78, 407 (2001)

(114) R. Kaur, A. V. Singh, and R. M. Mehra, Phys. Stat. Sol. A, 202,1053 (2005)

(115) X. Han, K. Han, and M. Tao, J. Electrochem. Soc. 157, H593 (2010)

(116) P. T. Hsieh, R. W. K. Chuang, C. Q. Chang, C. M. Wang, S. J. Chang, J Sol-Gel Sci Technol. 58, 41 (2011)

(117) M. H. Huang, S. Mao, H. Feick, H. Yan, Y. Wu, H. Kind, E. Weber, R. Russo, and P. Yang, J. Alloys Compd. 509, 3606 (2011)

(118) D. Ramirez, T. Pauporte, H. Gomez, and D. Lincot, Phys. Stat. Sol. A, 205, 2371 (2008)

(119) D. C. Reynolds, D. C. Look, B. Jogai, C. W. Litton, T. C. Collins, W. Harsch, and G. Cantwell, Phys. Rev. B, 57, 12151 (1998).

(120) J. Joo, B. rian Y. Chow, M. Prakash, E. S. Boyden, and J. M. Jacobson, Nat. Mater. 10, 596 (2011)

(121) H. J. Fan, B. Fuhrmann, R. Scholz, C. Himcinschi, A. Berger, H. Leipner, A. Dadgar, A. Krost, S. Christiansen, U. Gosele, and M. Zacharias, Nanotechnology 17, S231 (2006)

(122) Z. Li, Y. Luan, Q. Wang, G. Zhuang, Y. Qi, Y. Wang, and C. Wang, Chem. Commun. 1, 6273 (2009)

(123) D. M. Bagnall, Y. F. Chen, Z. Zhu, T. Yao, S. Koyama, M. Y. Shen, and T. Goto, Appl. Phys. Lett. 73, 1038 (1998)

(124) K. Thonke, Th. Gruber, N. Teofilov, R. Schonfelder, A. Waag, and R. Sauer, Physica B, 308, 945 (2001)

(125) C. Lungenschmied, G. Dennler, H. Neugebauer, S. N. Saricifitci, M. Glatthaar, T. Meyer, and A. Meyer, Sol. Energy Mater. Sol. Cells, 91, 379 (2007)

(126) S. I. Na, S. S. Kim, J. Jo, and D. Y. Kim, Adv. Mater. 20, 4061 (2008)

(127) J. A. Hauch, P. Schilinsky, S. A. Choulis, R. Childers, M. Biele, and C. J. Brabec, Sol. Energy Mater. Sol. Cells, 92, 727 (2008)